Nanostructured Spinel Type Cobalt Oxides for Electrochemical Water Splitting

Thesis Submitted to AcSIR for the Award of the

Degree of

Doctor of Philosophy

in Chemical Sciences

By

R. M. Ramsundar

AcSIR No: 10CC11J26023

Under the guidance of

Dr. P. A. Joy

and

Dr. Vijayamohanan K Pillai

CSIR-National Chemical Laboratory

Pune 411008, India

सीएसआईआर - राष्ट्रीय रासायनिक प्रयोगशाला
(वैज्ञानिक तथा औद्योगिक अनुसंधान परिषद)
डॉ. होमी भाभा मार्ग, पुणे - 411 008, भारत
CSIR - NATIONAL CHEMICAL LABORATORY
(Council of Scientific & Industrial Research)
Dr. Homi Bhabha Road, Pune - 411 008, India

Certificate

This is to certify that the work incorporated in this Ph.D. thesis entitled **"Nanostructured Spinel Type Cobalt Oxides for Electrochemical Water Splitting"** submitted by **Mr. R. M. Ramsundar** to **Academy of Scientific and Innovative Research (AcSIR)** in fulfillment of the requirements for the award of the **Degree of Doctor of Philosophy in Chemical Sciences**, embodies original research work under my supervision. I further certify that this work has not been submitted to any other University or Institution in part or full for the award of any degree or diploma. Research material obtained from other sources has been duly acknowledged in the thesis. Any text, illustration, table etc., used in the thesis from other sources, have been duly cited and acknowledged.

R. M. Ramsundar
(Student)

Dr. P. A. Joy
(Supervisor)

Dr. Vijayamohanan K. Pillai
(Co-Supervisor)

Communication Channels
NCL Level DID : 2590
NCL Board No. : +91-20-25902000
EPABX : +91-20-25893300
: +91-20-25893400
FAX
Director's Office : +91-20-25902601
COA's Office : +91-20-25902660
SPO's Office : +91-20-25902664
WEBSITE
www.ncl-india.org

DECLARATION

I, hereby declare that all the experiments in the thesis entitled, "**Nanostructured spinel type cobalt oxides for electrochemical water splitting**" submitted for the degree of **Doctor of Philosophy in Chemical sciences** to Academy of Scientific and Innovative Research (AcSIR), has been carried out by me at the Physical and Materials Chemistry Division of CSIR-National Chemical Laboratory, Pune, India under the joint supervision of **Dr. P. A. Joy** and **Dr. Vijayamohanan K. Pillai**. Research material obtained from other sources has been duly cited and acknowledged in the thesis. This work is original and has not been submitted in part of full by me for any degree or diploma to this or any other University.

R. M. Ramsundar

(R. M. Ramsundar)

Date : 04/05/17

CSIR-NCL

Pune, India.

...Dedicated to my Parents and to my sisters...

Acknowledgements

It is a great pleasure to express my gratitude and sincere thanks to all those who helped me directly and indirectly to complete this work. This thesis would not have been possible without all these people and their constant encouragement.

First of all, I would like to express my immense and sincere gratitude to my research supervisor ***Dr. P.A. Joy*** *for his constant support, encouragement and guidance throughout my Ph. D. I really admire the way he teaches many complicated things in a simple manner and giving freedom to work in different aspects without any pressure. I am also thankful to* ***Dr. Vijayamohanan K Pillai****, my co-guide for designing the work, timely advice and effective discussion during my Ph.D and completion of this thesis.*

I express my sincere thanks to the former directors Dr. Sivaram and Dr. S. Pal, and the present director, Dr. Ashwini Kumar Nangia, for allowing me to work in the prestigious Laboratory and making all the facilities available for my research work. I would like to acknowledge UGC for the financial assistance in the form of a research fellowship. I wish to thank Dr. Anilkumar, former Head of the Physical Chemistry Division, for allowing me to use all the divisional facilities. My sincere thanks to all the DAC members Dr. C. S. Gopinath ,Dr. K. Sreekumar and Dr.Nandini devi. They were kind enough to spend their valuable time for my evaluation presentations. The valuable suggestions given by them helped me to shape the thesis more perfectly.

I thank all my seniors, Vijay, Kannan Joyashish, Lenin, Khaja, Sreeja,, Mangesh, Pankaj, and for their help and support in the initial stages of my work, and my lab mates, Bindhu Govindraj, Jayaprabha, Anjali, Manjunath, Mohan, Anantharamaiah, Arun Anupriya Abhinath and Anagha for providing the nice working environment in the lab.

I take time to convey my gratitude to the project students who worked with me Nimisha, Majitha, Athira and Fawaz for their help.

I would like to thank all my friends who made my life at NCL more cheerful. Arul Kashmir, Jasmine, Senthil, Rajambal, Edwin, Palani, Senthil, Sivaranjani, Dhanalakshmi, Mohanraj, Suresh, Vasu, , Rajaperumal, Dhanasekar, Pandiaraj, Suman, Rupa, Venkat, Naren, Anuj, Ashok, Prabhu K, Prabhu M, Prabhu D, Devaraj, Kishodra, Kumar, Sudhakar, Chitravel,

Ananthan, Kubendiran, Punith, Subramani, Sridhar, Manikandan, Loganathan, Kuyilazhagan, Rami, Chaitanya.

My special regards to my teachers because of whose teaching at different stages of education has made it possible for me to see this day. Because of their kindness I feel, was able to reach a stage where I could write this thesis.

In this occasion I would like mention my friends Ebenezer, Pethan, Pavul, Jasmine , Rajeswari, Krisnaveni and Adaikalam for their constant support and help

My deepest acknowledgement goes to ***my parents, sisters and brother in laws*** *for their love, support and encouragement which made me to come up to this level*

R. M. Ramsundar

Contents

List of Figures

List of Tables

Abstract

Due to the increased population and anthropogenic activities, the world energy demand keeps increasing and the energy supply is lesser than the demand. Currently, major part of the energy supply is from the fossil fuels which emits CO_2 while burning and increases the global warming effect. Hydrogen is one of the fuels having high energy density than all other conventional fuels and it will give only water as a by-product while burning. Electrochemical water splitting is one of the attractive methods to produce hydrogen and it contains two half-cell reactions, hydrogen evolution at the cathode and oxygen evolution at the anode. Among these, oxygen evolution has sluggish kinetics and complicated multistep mechanism. At present, precious metal oxides such as RuO_2 and IrO_2 are used as anode materials for the oxygen evolution. To reduce the cost of production, the efficiency of the system has to be improved and the precious metal oxide catalysts have to be replaced by earth abundant and cost effective catalysts. Recently, Co_3O_4 is identified as one of the potential catalyst for the oxygen evolution due to its thermodynamic stability and electrocatalytic activity. In this thesis, we have studied the role of different oxidation states of cobalt in Co_3O_4 to increase the stability and electrocatalytic activity for the oxygen evolution reaction

Chapter 1 is a general introduction on the importance and production of hydrogen, water splitting mechanism and the catalysts used for water splitting. It also gives a brief introduction to the oxygen evolution reaction, the catalysts used, mechanism and thermodynamic study of the catalyst for oxygen evolution, and role of oxygen evolution catalyst in artificial leaf. The factors which influence the electrocatalytic activity for the oxygen evolution reaction are discussed. The oxygen evolution catalysts based on cobalt and their electrocatalytic studies are discussed. Finally, the structure and properties of the spinel Co_3O_4 and its importance in the oxygen evolution reaction are discussed.

Chapter 2 discusses about the synthesis of nanosized metal oxides by coprecipitation and autocombustion methods. Also, it discusses about the various characterization techniques used in the present study such as XRD, TEM, XPS, BET analysis and magnetic measurements. The details about the electrochemical methods like catalyst ink preparation, Tafel plot data collection and quantitative oxygen gas measurements are discussed.

Chapter 3 discusses about the electrocatalytic activities of nanostructured Co_3O_4 synthesized by different methods. Co_3O_4 nanorods are synthesized by template free, simple

coprecipitation/digestion method and the electrocatalytic activity in a wide pH range (4-14) is studied. The stability of Co_3O_4 nanorods in neutral and acidic pH is found to be enhanced due to the usage of phosphate buffer as electrolyte. The electrocatalytic activity of Co_3O_4 nanoparticles synthesized by autocombustion method are studied at basic pH and compared with the activity of Co_3O_4 nanorods. Both the Co_3O_4 nanorods and nanoparticles showed a low overpotential of 385 mV at 1 mA/cm^2 at neutral pH. The electronic structure of Co^{3+} in both the Co_3O_4 nanostructures and their electrocatalytic activities are correlated.

Chapter 4 discusses the role of Co^{2+} in the electrocatalytic activity of Co_3O_4 for the oxygen evolution reaction. Zn^{2+} is partially and progressively substituted for Co^{2+}in Co_3O_4 and the structural and electronic properties are studied using various techniques. Zn-substitution in Co_3O_4,is found to increase the high-spin contribution Co^{3+}in the octahedral sites as confirmed by absorption spectroscopy and magnetic studies. The population of high-spin Co^{3+} in the $Zn_xCo_{3-x}O_4$ is correlated with the electrocatalytic activity for the oxygen evolution reaction and $Zn_{0.8}Co_{2.2}O_4$gives the lowest overpotential (260 mV at 10 mA/cm^2) at the basic pH medium and the reason behind the enhanced electrocatalytic activity is discussed.

Chapter 5 discusses the role of Co^{3+} in the electrocatalytic activity of Co_3O_4 for the oxygen evolution reaction,by replacing Co^{3+} with Al^{3+}. Al-substituted Co_3O_4 compositions are characterized using various techniques. The electrocatalytic activity studies on $Co_{3-x}Al_xO_4$ showed that increasing the Al content decreases the electrocatalytic activity for the oxygen evolution reaction. It is confirmed that the reduction in the electrocatalytic activity is due to the decreased population of Co^{3+} in the compounds..

Chapter 6 discusses the effect of oxidation state of cobalt in the spinel cobalt oxides on the oxygen evolution reaction. Different oxidation states of cobalt (2+, 3+ and 4+) has been tuned in the cobalt oxides without changing the structure of the cobalt oxides. The electrocatalytic activity of $Li_{0.5}Co_{2.5}O_4$ (only Co^{3+}) is compared with that of Co_3O_4 (Co^{2+} and Co^{3+}). In the same way, the activity of $LiCoO_2$ (only Co^{3+}) is compared with that of $Li_{0.5}CoO_2$ (Co^{3+} and Co^{4+}). Finally, the electrocatalytic activities of Co_3O_4, $Li_{0.5}Co_{2.5}O_4$, $LiCoO_2$ and $Li_{0.5}CoO_2$are compared and correlated with the oxidation state of cobalt.

Chapter 7 summarizes the work reported in the previous chapters and the various factors that influence the electrocatalytic activity of cobalt oxides for oxygen evolution reaction. Scope for future work on the studied materials is discussed.

Chapter 1

Introduction

1.1 Energy demand and usage

The world energy demand is increased due to the increased world population. The world energy demand was 14 TW in 2015 and this keeps increasing day by day. The worldwide energy supply does not fulfill the energy requirement due to the unrestrained energy consumption. The major part of the energy production from non-renewable sources like fossil fuels, natural gas, etc. which emits CO_2 and contributes to global warming. The CO_2content in the atmosphere has already crossed 400 ppm [1]. Notably, world-wide CO_2 emission has been increased by 56% during 1990-2003. This increased CO_2 emission was anticipated due to the rapid growth in the population (by 35%) and per capita GDP (60%). In recent years, awareness is created among the developed countries and they have envisioned the generation of electricity from renewable energy resources which is increased by 2.5% every year. This increase can be ascribed to the growth of new renewable energy products like, solar photovoltaics, wind and bio gas in the global market. As a consequence, the share of electricity produced from renewable energy sources is increased by 6% between 1990 and 2015.Among the different sources, energy production using sunlight is promising in many ways like photovoltaics, and using dye sensitized solar cells which generate electricity from the sunlight. Solar energy can be stored in the form of chemical fuel and one of the best examples is conversion of water to H_2 and O_2 [2-3].

One of the best solutions to meet the high energy demand is the usage of the high-energy density fuel, Hydrogen. Hydrogen has a very high energy density value compared to the conventional fuels like petrol, diesel, and gasoline. Particularly, it has 3 times higher energy density compared to that of petrol. Table 1.1 shows the energy density values of commonly used fuels [4].

Table 1.1 Energy density of different fuels

Fuel	**Energy density (MJ/kg)**
Coal	24
Diesel	45.4
Propane (LPG)	46.4
Gasoline (Petrol)	47.2
Hydrogen	123

When hydrogen is burned with oxygen, it gives water and heat as the by-products. The absence of carbon emission, which makes hydrogen as a very attractive fuel for energy production, is a greenerway for the environment. Moreover, hydrogen can be converted into many energy-rich materials like NH_3, CH_4, and CH_3OH for better storage and transport. All the above mentioned materials have a wide range of applications in industrial and agricultural sectors. However, hydrogen can be considered as a renewable/sustainable energy only when the production of hydrogen is also from the renewable sources without affecting the environment.

1.2 Hydrogen economy

At present, more than 90% of hydrogen is being produced from the steam reforming reaction, where hydrogen is produced by the burning of hydrocarbons (methane, natural gas) at high temperatures. The formed carbon monoxide reacts with water and gives hydrogen and carbon dioxide[5].

$$CH_4 + H_2O \rightarrow CO + 3\ H_2 + 191.7\ \text{kJ/mol} \qquad (700–1100\ ^\circ\text{C})$$
$$CO + H_2O \rightarrow CO_2 + H_2 - 40.4\ \text{kJ/mol} \qquad (130\ ^\circ\text{C})$$

The higher reaction temperature, CO_2 emission, and the use of non-renewable sources (natural gas, methane) are the major drawbacks of this method of hydrogen production.

Artificial photosynthesis has gained much attention due to its higher efficiency in the conversion of the sunlight to oxygen and carbohydrates [6-8]. Only 1% of incident solar energy is utilized for photosynthesis for the production of oxygen and carbohydrates. Among the overall process of photosynthesis, the oxygen evolution reaction mediated by the oxygen evolving complex, tetramanganese oxide cluster, in the Photosystem II is the difficult reaction [6-8]. This is because of the energetically uphill reaction and also it is a $4e^-$ transfer reaction with a complicated multistep mechanism [9-11].

Solar to hydrogen generation which mimics the photosynthesis can be executed in two different ways. In the *indirect* configuration, currently available photovoltaic (PV) devices are used to collect the solar energy which is converted to electrical energy. The generated electrical current is utilized to run the electrolyzer which generates hydrogen. In this method, PV device + electrolyzer system achieved more than 20% efficiency for production of hydrogen [12-13]. However, the high cost of photovoltaic materials and the catalysts used in

the electrolyzer are the major drawbacks of this system. Particularly, low-cost, earth abundant catalyst for the hydrogen and oxygen evolution reactions must be developed. Therefore, the introduction of cost-efficient materials based on the earth abundant elements will be the solution for the widespread implementation of PV device + electrolyzer system [14-16]. An alternative for the solar hydrogen production is a *direct* solar-to-water splitting conversion, which is called as *photoelectrochemical(PEC) water splitting.* Actually, it is a complicated process that requires fundamental knowledge in physics, chemistry, optics, electronics and thermodynamics. In *semiconductor photoeelctrochemistry*, light-sensitive semiconductor photoelectrode is immersed in an aqueous solution which is connected to a metallic counter electrode through an external circuit. The photoelectrode is illuminated by sunlight which creates photogenerated electron-hole pairs. Photogenerated holes drive the oxygen evolution reaction at the electrode-electrolyte interface of the anode, while the photogenerated electrons drive the hydrogen evolution reaction at the cathode surface. The cost of the PEC system is expected to be less than that for the PV device + electrolyzer system. However, it is associated with many complicated problems. The magnitude of the potential generated in the PEC and the kinetics of water splitting reaction mainly depend on the nature of the semiconductor/electrolyte interface. Moreover, the chosen semiconductor catalyst should possess stability in the highly oxidizing water oxidation conditions and higher carrier life time is required for the photogenerated electron-hole pairs.In both *direct* and *indirect* methods of solar-to-hydrogen production by water splitting, the oxygen evolution reaction controls the overall efficiency of water splitting.

1.3 Water splitting

The electrochemical water splitting can be done by a simple two-electrode system in which oxygen evolution from anode and hydrogen evolution from cathode take place and this can be explained by the following half-cell reactions:

$H_2O \longrightarrow 4e^- + O_2 + 4H^+$ (Oxygen Evolving Reaction at anode) (1)

$2H^+ + 2e^- \longrightarrow H_2$ (Hydrogen Evolving Reaction at cathode) (2)

The overall reaction is

$H_2O \longrightarrow O_2 + ½\ H_2$ ΔG_o=237.2 kJ/mol ΔE_o =-1.23V (3)

Equation 3 shows that one mole of water contains 237.2 kJ of energy and the corresponding thermodynamic potential (V_{rev}) is 1.23 V. In practice, to split water, more than 1.23 V is required due to the kinetic complexity and the sluggish rate of the reaction. The operating voltage, V_{op}, is given by

$$V_{op} = V_{rev} + \eta_a + \eta_c + \eta_\Omega + \eta_{sys} \quad (4)$$

In addition to the V_{rev}, anodic overpotential (η_a), cathodic overpotential (η_c), ionic conductivity losses (η_Ω) and other system losses (η_{sys}) increases the operating potential. Usually, water electrolysis requires 1.6–1.9 V, which depends on the gas production rate. The anodic and cathodic overpotentials are related to the intrinsic activation barrier for oxygen evolution and hydrogen evolution reactions, respectively, and are responsible for 85% of total efficiency losses [17]. Overpotential can be correlated to the activation energy and the current density can be correlated to the electrochemical reaction rate. The overpotential(η) and the current density(i) are related through the Tafel equation:

$$\eta = a + b \log (i) \quad (5)$$

where '*a*' is related to the activity of the electrode and '*b*' is related to the mechanism of the reaction, which is also called as *Tafel slope*. Tafel equation is derived from the Butler-Volmer equation based on the approximations that (i) overpotential is sufficiently large, where there is no backward reaction, and (ii) there is no effect of concentration gradient. The formation of concentration gradient can be avoided by gently stirring the electrolyte during the data collection for the Tafel plot. Figure 1.1 shows the Tafel plot for an anodic process. It shows that at higher current density, the plot is linear and when approaching low current density, the plot deviates from linearity. The linear part of the plot can be fitted to a straight line. The slope of the fitted line is called Tafel slope. The point of intersection of the straight line on the x-axis (at $\eta = 0$) is called exchange current density (i_o). Exchange current density can be defined as the rate of reaction at zero overpotential. At zero overpotential, the rate of forward and backward reactions is equal, the net rate of reaction is zero, and the system is at equilibrium condition. Hoar[14] was the first who made the connection between Tafel line and the overpotential for oxygen evolution. The experimentally observed Tafel slope for the oxygen evolution reaction varies from 30 mV to 120 mV (per decade of current). The

intermediate values are interpreted in terms of mixed mechanism or the intermediate coverage of adsorbed species [18].

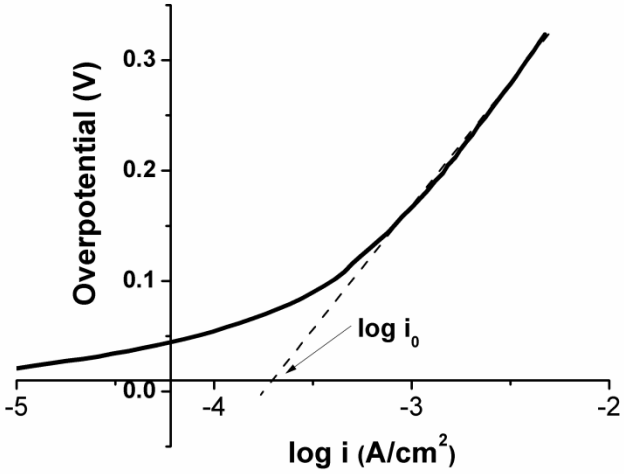

Figure 1.1 Tafel plot for an anodic process

Between the oxygen evolution and hydrogen evolution reactions, oxygen evolution is the complicated one because it is a $4e^-$ transfer, multistep, and sluggish reaction, which is the rate determining step. In a solid-electrolyte interface, at a time only one electron can transfer. The exchange current density is about 10^{-9} to 10^{-12} A/cm^2 since the reaction is a sluggish one. In the electrolysis of water, 70% of the total cost of production of hydrogen is due to the amount of electricity used. If we can catalyze the oxygen evolution reaction, we can increase the efficiency of the overall reaction and thus decrease the total cost of production.

In the photosynthesis for conversion of solar energy to fuel, a leaf splits the water by photosynthetic process to produce oxygen and hydrogen. The primary step of photosynthesis is the absorption of the sunlight and its conversion of electron-hole pairs. The photogenerated holes are utilized by the oxygen evolution complex for the production of oxygen. The photogenerated electrons and protons produced by the oxygen evolution reaction are captured by ferredoxin in the photosystem I for the production of hydrogen in the form of NADPH [19].

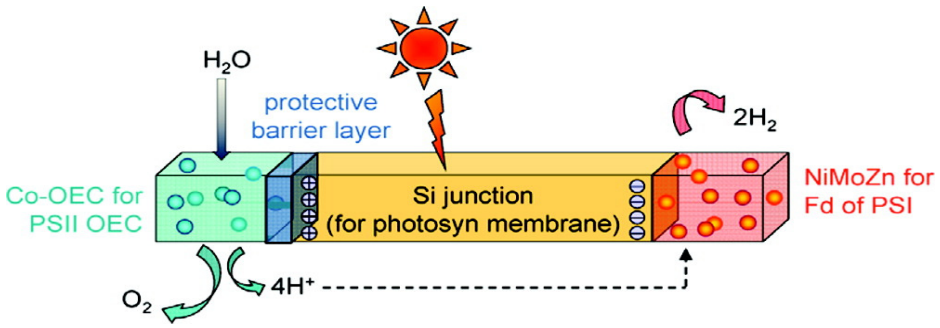

Figure 1.2 Construction of an artificial leaf. The photosynthesis membrane is replaced by a Si junction, which performs light capture and conversion to a wireless current. The oxygen evolving complex and ferredoxin reductase of the photosynthesis membrane are replaced by Co-OEC and NiMoZn OER and HER catalysts, respectively, to perform water splitting (Figure adapted from [19]).

Figure 1.2 shows an artificial leaf, in which Co-OEC (anode) and NiMoZn (cathode) are incorporated to the single junction Si cell. The single junction Si cell does the function of the membrane in photosynthesis. The ability to catalyze water oxidation and water reduction in neutral medium by Co-OEC and NiMoZn make the catalysts suitable for the artificial leaf. Illumination of sunlight on the Si cell generates electron-hole pairs. The holes are captured by Co-OEC and the electrons are utilized for the reduction of water at cathode. Single junction Si cell is not sufficient to achieve a higher voltage to catalyze water splitting at a reasonable rate of reaction. By replacing the single junction Si cell with a triple junction Si solar cell, a potential of 1.8 V can be achieved. When the solar cell is illuminated, the generated potential is sufficient to meet the potential needed for water splitting and no external potential is required. As a result, a solar to fuel efficiency of 4.7% can be attained.

1.4 Hydrogen evolution reaction

Hydrogen evolution reaction is one of the half-cell reactions occurring at the cathode. The protons generated are reduced at the cathode and produce hydrogen. Platinum is the well known electrocatalyst for hydrogen evolution reaction. It has near zero overpotential for the hydrogen evolution reaction, with a very high exchange current density (10^{-3} A/cm^2) [20]. However, the high cost of the platinum limits its practical usage and increases the cost of production of hydrogen. Ni-Mo, Ni-Co and Ni-Fe binary compositions have been reported to show good catalytic activity for hydrogen evolution [16]. Recently, MoS_2 has been reported to show good electrocatalytic activity for the hydrogen evolution reaction at a low overpotential of 176 mV at 10 mA/cm^2 [15].

1.5 Oxygen evolution reaction

Oxygen evolution reaction is the bottleneck for the efficient conversion of solar energy to renewable fuels by water splitting. Hence, catalysing the oxygen evolution reaction will bring many developments in the solar energy conversion systems. Since the oxygen evolution reaction (OER) is a complex, multistep, inner-sphere process and critically depends on the formation and stabilization of high energy surface, confined, intermediates, it is difficult to study the interaction between the catalyst surface and the reaction intermediates experimentally. The short lifetime of the reaction intermediates, harsh reaction conditions and extensive gas evolution from the surface of the catalyst are the important reasons which make the system more complicated to study experimentally. To explore the fundamental understanding about OER, theoretical approaches help in a constructive way, where individual reaction steps and intermediates are accessible.

Quantum mechanical calculations, based on density function theory (DFT), have been used to study the individual reaction steps of the associative mechanism of OER. The individual reaction steps are shown below [21]:

$$M + H_2O \xrightarrow{\Delta G1} MOH + H^+ + e^-$$

$$MOH \xrightarrow{\Delta G2} MO + H^+ + e^-$$

$$MO + H_2O \xrightarrow{\Delta G3} MOOH + H^+ + e^-$$

$$MOOH \xrightarrow{\Delta G4} M + O_2 + H^+ + e^-$$

M refers to the surface metal atom of the catalyst, MO, MOH, and MOOH refers to the possible intermediate species in the reaction mechanism. ΔG_i refers to the Gibbs free energy of the reaction step *i*. From the mechanism shown above, each reaction involves the transfer of a single electron with a change in free energy. From this, the Gibbs adsorption free energies of the surface reaction intermediates; ΔG_{MOH}, ΔG_{MO}, and ΔG_{MOOH}; can be calculated with respect to the applied potential. At a given applied potential, Gibbs free energy change of a particular mechanistic step is given by the difference between the adsorption energies of the two intermediates which are involved in the reaction. For example, ΔG_3depends on the Gibbs free energies of the reaction intermediates MO and MOOH. Therefore,

$$\Delta G_3 = \Delta G_{MOOH} - \Delta G_{MO} - qV$$

Likewise, reaction free energy diagrams are generated to identify the thermodynamically least favourable step in the reaction pathway.

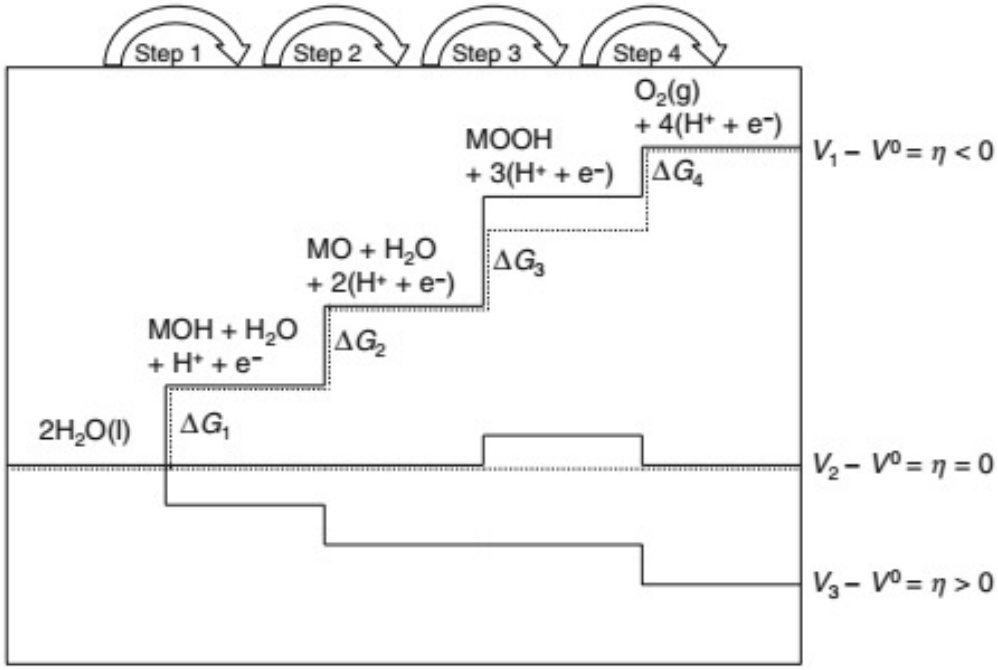

Figure 1.3 Schematic plot of the Gibbs free energy of the reactive species and intermediates in theoxygen evolution reaction versus the reaction coordinate. Solid lines indicate the energetics of a'Real' catalyst at three different potentials. Dotted lines represent the energetics of an 'Ideal'catalyst. (Adapted from [20])

Fig 1.3 shows the schematic representation of the free energy diagram of a hypothetical catalyst with the reaction intermediates in the oxygen evolution reaction along the reaction coordinate. The reaction coordinate moves from free water (left) to free O_2 (right). The solid lines represent the energetics of a 'Real' catalyst, whereas the dotted lines represent the energetics of an 'Ideal' catalyst at three different applied potentials. The horizontal lines represent the free adsorption energies of the individual reaction intermediates in the oxygen evolution reaction.

1.6 Solid catalysts for oxygen evolution

At present, the well known catalysts for oxygen evolution are RuO_2 and IrO_2. Both are precious metal oxides and very costly due their less abundance on the earth's crust. Moreover, RuO_2 and IrO_2 can work only in the acidic medium. Among these two catalysts,

IrO_2 is considered as a good catalyst than RuO_2. This is because, RuO_2 gets converted into RuO_4 during the oxygen evolution process and the electrocatalytic activity is reduced with time. There are many attempts to improve the stability and catalytic activity of RuO_2 and IrO_2. Substitution of iridium in RuO_2 ($Ir_xRu_{1-x}O_2$) provides higher stability in acidic medium than for RuO_2 and more activity compared to IrO_2 for the OER. Particularly, $Ir_{0.2}Ru_{0.8}O_2$ has been shown to have higher stability and electrocatalytic activity compared to other compositions [22].

In the recent years, much attention is focused on developing a good catalyst based on the earth abundant elements to reduce the cost of production of hydrogen. The first volcano plot related to the OER activity of metal oxides was reported by Trasatti[18, 23]. The author correlated the overpotential for OER and the standard enthalpy change for the conversion of the metal ion from lower to higher valency in the oxide, $MO_x \rightarrow MO_{x+1}$. The higher activity of RuO_2 and IrO_2 are correctly predicted in this study. Since OER is expected to involve more than one surface bound oxygen moiety intermediates such as MOH, MO or MOOH, the volcano plot correlation can be rationalised. The interaction of these intermediates with the surface of MOx could result in the increased coordination sphere of M. Hence, their formation would be expected to parallel the heat of formation of the higher valence state.

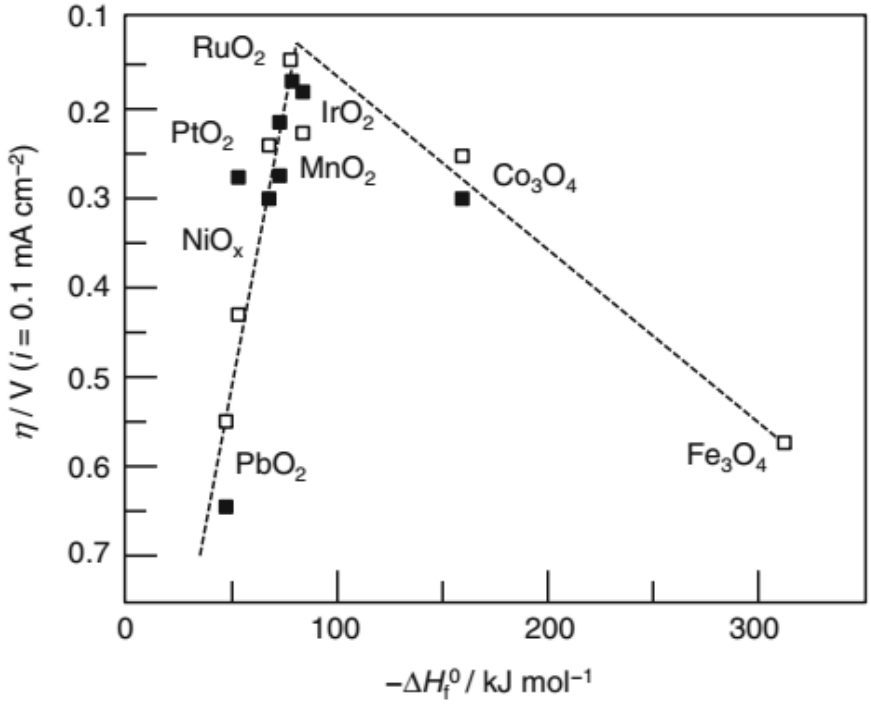

Figure 1.4 Volcano plot of OER activity for the various oxide catalysts in acidic (unfilled) and basic (filled) media versus the enthalpy of a lower to higher valent transition.

Trasatti emphasized that the surface redox reactions play very important role in electrocatalysis [23]. When a metal ion is oxidized to the higher oxidation state, it becomes more oxidizing and more electron-attractive. Hence, the higher valent cations act as active sites for the oxidation of water to oxygen and the oxidation of the metal ion precedes the oxygen evolution. This shows that the redox potential of the metal oxide surface must be close to the thermodynamic potential for oxygen evolution. With the reference of this, materials with no redox reactions available at a potential higher than the thermodynamic potential of oxygen evolution are expected to show higher overpotential for OER. Because of this, SnO_2, TiO_2, PbO_2 and PtO_2 have higher overpotential for OER, due to the non-availability of redox transitions at a potential range higher than the thermodynamic potential of oxygen evolution [18].

Recently, many non-precious transition metal oxides have shown promising catalytic activity for the oxygen evolution reaction. Transition metal ions are well known for their multiple oxidation states and redox properties. However, there is limitation for the use of the transition metal oxides as catalysts due to the dissolution of the catalyst in neutral and acidic media. These catalysts are active only in the alkaline medium [24]. NiO, $Ni(OH)_2$ and MnO_2 nanostructures have shown remarkably low overpotential (~300-320 mV) for oxygen evolution in alkaline medium [25-27]. Similarly, spinel oxides such as $NiCo_2O_4$, $ZnCo_2O_4$ and $CoFe_2O_4$ are shown to have better stability and catalytic activity towards oxygen evolution[28-30]. Cobalt containing perovskites like $LaCoO_3$ and $Ba_{0.5}Sr_{0.5}Co_{0.8}Fe_{0.2}O_{3-\delta}$ have also been indentified for their superior electrocatalytic activity for OER [31-32].

Even though many catalysts, based non-precious metal oxides, have been identified in the recent times, tuning/designing the catalyst for the oxygen evolution reaction is still an open challenge. This is because, oxygen evolution is a $4e^-$ transfer, multistep reaction with complicated mechanism and a double bond is formed between two oxygen atoms, which comes from two different water molecules. Most of the mechanistic studies have been carried out electrochemically using platinum only because of the simplicity. The oxygen evolution reaction on metal oxide surface is very complicated. Many factors/descriptors will be governing the catalytic activity which may vary with the nature of the element and surface of the catalyst.

From the nature's oxygen evolving complex, $CaMa_4O_x$, the presence of M_4O_4 cluster is identified as one of the descriptor for OER. Particularly, in the case of transition metal

oxides, the presence of M_4O_4 cluster is identified as essential for the oxygen evolution activity. Even, compounds with the same molecular formula, without M_4O_4 cluster, is not active for OER. For example, $LiMn_2O_4$ is a catalytically inert spinel for OER. However, upon complete delithiation by dilute nitric acid treatment, the formed λ-MnO_2 (which differs from β-MnO_2) is found to be highly active for OER. The Mn_4O_4 cubane structure is activated by delithiation [33]. The same is true with cubic $Li_2Co_2O_4$ and layered $LiCoO_2$. Layered $LiCoO_2$is a well-known anode material for batteries, but it is not active for OER. However, cubic spinel-type $Li_2Co_2O_4$ shows significant catalytic activity for OER. Cubic $Li_2Co_2O_4$ comprised of Co_4O_4 units, whereas layered $LiCoO_2$comprised of alternating layers of Co-O and Li-O octahedra that form $LiCo_3O_4$ units and not Co_4O_4 units [34]. Molecular Co_4O_4 complexes such as $Co_4O_4(OAc)_4(Py)_4$ and $[Co_4O_4(CO_2Py)_2(bpy)_4](ClO_4)_2$ have been synthesized and studied for their catalytic activity for OER by photochemical method. Both show significant catalytic property for photochemical OER [35-36].

In addition to the well known descriptors like surface area, porosity, and particle size, many other descriptors are also identified for the catalytic activity for oxygen evolution, such as e_g occupancy of the octahedral metal cation, number of *d*-electrons in the transition metal ion, oxidation state of the metal ion, M-O bond length, prefrential exposure of lattice planes and magnetic moment of the catalyst [37].From the crystal field perspective, octahedrally coordinated 3d metal ion's *d* orbital will be split in to the many energy levels. Particularly, e_g and t_{2g} levels are very important for the catalysis, because, these two states are involved in the overlap with the oxygen related adsorbates and intermediates. Among the two states, e_g orbital has stronger overlap with the oxygen related adsorbate due to its sigma bonding nature than the t_{2g} orbital with the pi-bonding nature [38-39]. Because of these reasons, e_g orbital occupancy is one of the important descriptors for the oxygen evolution reaction.

Shao-Horn and co-workers studied the strong correlation between the electronic structure of the transition metal oxides and the electrocatalytic activities for OER [31]. In perovskites, electron occupancy in the e_g orbital has been identified as a descriptor for OER. A series of perovskites with different e_g orbital occupancy have been synthesized and studied for their OER activity. e_g orbital occupancy was determined from X-ray absorption near edge structure (XANES), magnetic studies and other characterization methods. Finally, OER activity and e_g orbital occupancy is correlated and in the form of a volcano plot (Figure1.5).

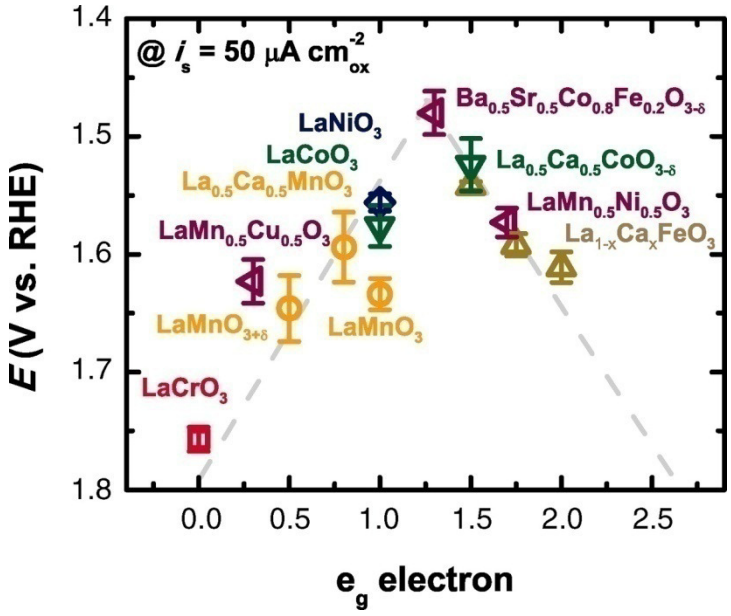

Figure 1.5 Volcano plot showing the relationship between OER catalytic activity, defined as the overpotential at 50 μA cm^{-2}(estimated true oxide surface area), and the e_g orbital occupancy of the B-site transition metal ion (figure adapted from [31])

The volcano plot (Figure 1.5) shows that the catalysts with the e_g orbital occupancy close to 1 are more active for OER (eg $LaCoO_3$, $LaNiO_3$). $Ba_{0.5}Sr_{0.5}Co_{0.8}Fe_{0.2}O_{3-\delta}$ with the e_g orbital occupancy of 1.2 shows the highest activity for OER in the volcano plot.

In the same way, the e_g orbital occupancy and OER activity in $LaCoO_3$ is studied with different sizes of $LaCoO_3$ [40]. Change in the size of $LaCoO_3$ is found to change the e_g orbital occupancy. Among the different e_g occupancies studied (1, 1.1, 1.2, 1.3), $LaCoO_3$ with e_g occupancy =1.2 has shown the highest electrocatalytic activity for OER, which proves the Shao-Horn principle. Copper rhodium delafossite ($CuRhO_2$) with e_g =1 shows higher electrocatalytic activity for OER compared to the other copper delafossites ($CuYO_2$, $CuAlO_2$, $CuFeO_2$) which have lower e_g occupancy values [41].

1.6.1 Cobalt containing oxygen evolution catalysts

Recently, Nocera and co-workers [42] deposited amorphous cobalt containing phosphate (denoted as Co-Pi) electrochemically and studied the electrocatalytic activity for OER at neutral pH. Phosphate buffer (KH_2PO_4) was used as the electrolyte which has important role in the proton-coupled electron transfer (PCET) for OER. A self-repairing behaviour was observed using the above catalyst for OER [43]. When the thickness of the thin film was

increased, OER activity was found to increase, which suggested that the Co-Pi film is permeable to the used electrolyte and also to the cobalt atoms which are inside the bulk of the material which are capable of working as active sites for OER. Structural studies on the Co-Pi films using EXAFS revealed that the structure comprised of bis-μ-oxo/hydroxo linked Co ions and this has been explained based on molecular cobaltate clusters [44]. In this model, the cluster consists of Co^{3+}-oxo/hydroxocubanes, with cobalt in edge sharing octahedra. Both EPR and XANES studies indicated that the valency of the cobalt ion is more than 3 and the population of Co^{4+} increased during the water oxidation reaction [44]. This implies that redox behaviour of Co^{3+}/Co^{4+} mediates the electron transfer for OER.

Recent *in situ* spectroscopic studies on the catalysts for OER revealed some mechanistic details. Zhang *et al* studied the water oxidation intermediates on cobalt oxides by time resolved Fourier-transform infrared spectroscopy [45]. Based on the identified surface superoxide intermediate (absorption at 1013 cm^{-1}), a mechanistic pathway has been proposed. Under electrocatalytic conditions, the surface of Co_3O_4 changed to hydroxyl-rich Co(O)OH structure. According to the proposed mechanism, two sequential hole injection converts Co(III)-OH to Co(IV)-OH. Then the nucleophilic addition of H_2O to one of the oxo sites results in the O-O bond formation and a hydroperoxide surface species. Also, both the metal centres reduce from Co(IV) to Co(III). Later, subsequent injection of two holes drives the formation of O_2 from the superoxo intermediate.

Bergmann *et al* [46] studied the surface of cobalt oxide for OER by *in situ* X-ray techniques. The studies revealed that the surface of cobalt oxide becomes amorphous with high content of hydroxyl groups, $CoO_x(OH)_y$, and it comprises of di-μ-oxo bridged Co^{3+}/Co^{4+} ions. This redox couple is responsible for the electron transfer reactions for OER. Interestingly, after OER, the surface of the cobalt oxide reverts back to its original structure and flexibility of the structure on the surface is observed. During the applied potential for OER, the tetrahedral Co^{2+} ions on the surface are oxidized to Co^{3+} and also changes its coordination environment from tetrahedral to octahedral and incorporated in the $CoO_x(OH)_y$ species.

1.6.2 Spinel type cobalt oxide, Co_3O_4

Cobalt oxide (Co_3O_4) has a normal cubic spinel structure with the general formula AB_2O_4. It is a face centred cubic (fcc) crystal system with the $Fd\bar{3}m$ space group and contains cobalt in two different oxidation sates, Co^{2+} and Co^{3+}. Co^{2+} occupies the tetrahedral sites (A-site) and

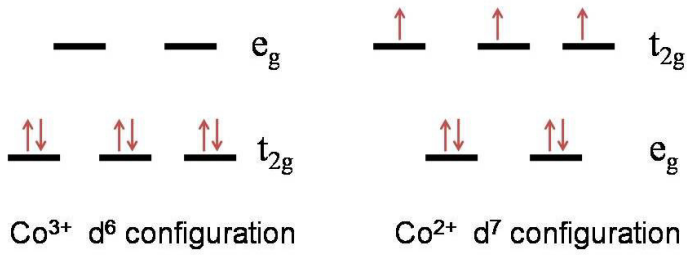

Figure 1.6 crystal field splitting of Co^{3+} ion in octahedral field (on the left) and Co^{2+} ion in tetrahedral field (on the right).

Co^{3+} occupies octahedral sites (B-site) [47]. In a crystal field, the degenerated d orbitals of Co^{2+} and Co^{3+} split into two groups as shown in Figure 1.6.

The Co^{3+} ion in the octahedral site is low-spin (t_{2g}^6) and diamagnetic [48]. This is because, the crystal field splitting energy, Δ_0 (19000 cm^{-1}) [48], is much higher than the electron pairing energy of 11600 cm^{-1} [49]. Co^{2+} in the tetrahedral site is in the high-spin configuration ($e_g^4\ t_{2g}^3$) with three unpaired electrons, S=3/2, and therefore, carry a magnetic moment. Co_3O_4 is found to be paramagnetic at room temperature and antiferromagnetic below the Neel temperature, $T_N \approx 40$ K [48] due to the week coupling between the nearest Co^{2+} ions. It is a p-type semiconductor with the band gap of 1.6 eV [50-51].

Co_3O_4 is identified as one of the functional materials with applications in a variety of fields in science and technology. Co_3O_4 has applications in supercapacitor, Li-ion battery, gas sensors and catalyst for oxidation [52-54]. Also, it is known for its catalytic activity in oxygen evolution reaction, oxygen reduction reaction, CO_2 reduction and CO oxidation [55-57]. Esswein *et al* studied the correlation between the size of the Co_3O_4 nanoparticles and the electrocatalytic activity for OER [58]. Different sizes of Co_3O_4nanoparticles were synthesized and tested for the electrocatalytic activity for OER. When the size of the Co_3O_4 nanoparticles is decreased, the overpotential for the OER is also decreased.This is due to the increased surface area of the smaller sized nanopartciles which increases the number of the catalytic sites on the surface of the nanoparticles.

1.7 Scope of the thesis

Recently, cobalt based catalysts are shown to have superior catalytic activities for the oxygen evolution reaction. This can be the due the intrinsic property of the cobalt ion in the studied compounds. Particularly, nanostructured spinel Co_3O_4 has gained much attention for OER

among the earth abundant metal oxides, because of its thermodynamic stability and electrocatalytic activity for OER. Even though many mechanisms are proposed for the electrochemical activity for, the exact reason/mechanism for OER on the surface of complex metal oxides like spinels and perovskites is not yet clear. The objective of the present work is to identify the descriptors for the oxygen evolution reaction on spinel-type cobalt oxide and thereby increasing the catalytic activity by modifying the cobalt oxide.

According to the *pourbaix diagram*, Co_3O_4 is not stable below pH 9 under oxygen evolution condition [59]. At low pH, severe corrosion occurs at the surface of the catalyst leading to dissolution of the cobalt ions. One of the important requirements for an oxygen evolution catalyst is improved solar-to-hydrogen conversion efficiency in photoelectrochemical water splitting cells, which demands neutral medium electrolytes. Moreover, the conductivities of neutral electrolytes are quite low compared to acidic and basic electrolytes which create higher resistance and reduce the overall rate of the water splitting reaction. In the present study, we tried to look at the possibility of using Co_3O_4 as an efficient oxygen evolution catalyst in a wide range of pH (4-14), particularly at the neutral medium.

As discussed, Co_3O_4 is a mixed metal oxide with the cubic spinel structure (AB_2O_4), in which Co^{2+} occupies in the tetrahedral coordination environment (A-site) and Co^{3+} occupies in the octahedral coordination environment (B-site). Previous studies have shown that in spinels, octahedral Co^{3+} is responsible for the most of the catalytic conversions. To understand the role of Co^{2+} and Co^{3+}in Co_3O_4, these ions are replaced partially and separately using an appropriate metal ion such as Zn^{2+} and $Al^{3+}$and studied the role of the substituted compositions for OER.

The effect of the oxidation state of cobalt plays a vital role in the electrocatalysis for OER, since the Co^{3+}/Co^{4+} redox couple is reported to play a major role. Usually, higher valent metal cations are the active sites for OER. Usually, lithium doping is expected to increase the electrocatalytic activity of many anode and cathode materials. Therefore, the electrocatalytic activities of different lithium cobalt oxides having the similar spinel structure as that of $Co_3O_4$and having different oxidation states of cobalt is studied. The compositions $Li_{0.5}Co_{2.5}O_4$ (only Co^{3+}), $LiCoO_2$ (only Co^{3+}), and $Li_{0.5}CoO_2$ (Co^{2+} and Co^{3+}) are studied and compared their activities with that of Co_3O_4 (Co^{2+} and Co^{3+}).

References:

1. Statistics, I. E. A., *CO2 Emissions from Fuel Combustion–Highlights 2012*. IEA, Paris Cited July: 2014.
2. Statistics, I. E. A., *Renewables information*. IEA, Paris Cited July: 2016.
3. Statistics, I. E. A., *World energy statistics*. IEA, Paris Cited July: 2016.
4. *https://en.wikipedia.org/wiki/Energy_density*.
5. Rajeshwar, K.; McConnell, R. D.; Licht, S., *Solar hydrogen generation: toward a renewable energy future*. Springer Verlag: 2008.
6. Ferreira, K. N.; Iverson, T. M.; Maghlaoui, K.; Barber, J.; Iwata, S., *Science* **2004,** *303*, 1831.
7. Barber, J., *Inorganic Chemistry* **2008,** *47*, 1700.
8. Loll, B.; Kern, J.; Saenger, W.; Zouni, A.; Biesiadka, J., *Nature* **2005,** *438*, 1040.
9. Aho, A.; Antonietti, M.; Arndt, S.; Behrens, M.; Bill, E.; Brandner, A.; Centi, G.; Claus, P.; Cox, N.; DeBeer, S., *Chemical energy storage*. Walter de Gruyter: 2013.
10. Barber, J., *Chemical Society Reviews* **2009,** *38*, 185.
11. Dau, H.; Zaharieva, I., *Accounts of Chemical Research* **2009,** *42*, 1861.
12. Khaselev, O.; Turner, J. A., *Science* **1998,** *280*, 425.
13. Turner, J. A., *Science* **2004,** *305*, 972.
14. Hoar, T. P., *Proceedings of the Royal Society of London. Series A, Containing Papers of a Mathematical and Physical Character* **1933,** *142*, 628.
15. Ma, L.; Ting, L. R. L.; Molinari, V.; Giordano, C.; Yeo, B. S., *Journal of Materials Chemistry A* **2015,** *3*, 8361.
16. Walter, M. G.; Warren, E. L.; McKone, J. R.; Boettcher, S. W.; Mi, Q. X.; Santori, E. A.; Lewis, N. S., *Chemical Reviews* **2010,** *110*, 6446.
17. Greeley, J.; Markovic, N. M., *Energy & Environmental Science* **2012,** *5*, 9246.
18. Trasatti, S., Electrochemical Theory | Oxygen Evolution In *Encyclopedia of Electrochemical Power Sources*, Elsevier: Amsterdam, 2009; pp 49.
19. Nocera, D. G., *Accounts of Chemical Research* **2012,** *45*, 767.
20. Dau, H.; Limberg, C.; Reier, T.; Risch, M.; Roggan, S.; Strasser, P., *ChemCatChem* **2010,** *2*, 724.
21. Doyle, R. L.; Lyons, M. E., The Oxygen Evolution Reaction: Mechanistic Concepts and Catalyst Design. In *Photoelectrochemical Solar Fuel Production*, Springer: 2016; pp 41.

22. Cheng, J. B.; Zhang, H. M.; Chen, G. B.; Zhang, Y. N., *Electrochimica Acta* **2009,** *54*, 6250.
23. Trasatti, S., *Electrochimica Acta* **1991,** *36*, 225.
24. Pourbaix, M., *Atlas of electrochemical equilibria in aqueous solutions*. Pergamon Press, Oxford: 1974.
25. Browne, M.; Cullen, R. J.; Doyle, R. L.; Colavita, P. E.; Lyons, M. E. G., *ECS Transactions* **2013,** *53*, 59.
26. Godwin, I. J.; Lyons, M. E. G., *Electrochemistry Communications* **2013,** *32*, 39.
27. Stern, L. A.; Hu, X., *Faraday Discussions* **2015,** *176*, 363.
28. Jin, C.; Lu, F.; Cao, X.; Yang, Z.; Yang, R., *Journal of Materials Chemistry A* **2013,** *1*, 12170.
29. Kim, T. W.; Woo, M. A.; Regis, M.; Choi, K. S., *Journal of Physical Chemistry Letters* **2014,** *5*, 2370.
30. Xu, Y. J.; Bian, W. Y.; Wu, J.; Tian, J. H.; Yang, R. Z., *Electrochimica Acta* **2015,** *151*, 276.
31. Suntivich, J.; May, K. J.; Gasteiger, H. A.; Goodenough, J. B.; Shao-Horn, Y., *Science* **2011,** *334*, 1383.
32. Grimaud, A.; May, K. J.; Carlton, C. E.; Lee, Y. L.; Risch, M.; Hong, W. T.; Zhou, J.; Shao-Horn, Y., *Nature communications* **2013,** *4*, 2439.
33. Fayette, M.; Nelson, A.; Robinson, R. D., *J. Mater. Chem. A* **2015,** *3*, 4274.
34. Gardner, G. P.; Go, Y. B.; Robinson, D. M.; Smith, P. F.; Hadermann, J.; Abakumov, A.; Greenblatt, M.; Dismukes, G. C., *Angewandte Chemie International Edition* **2012,** *51*, 1616.
35. Symes, M. D.; Lutterman, D. A.; Teets, T. S.; Anderson, B. L.; Breen, J. J.; Nocera, D. G., *ChemSusChem* **2013,** *6*, 65.
36. McCool, N. S.; Robinson, D. M.; Sheats, J. E.; Dismukes, G. C., *Journal of the American Chemical Society* **2011,** *133*, 11446.
37. Hong, W. T.; Welsch, R. E.; Shao-Horn, Y., *The Journal of Physical Chemistry C* **2016,** *120*, 78.
38. Betley, T. A.; Wu, Q.; Van Voorhis, T.; Nocera, D. G., *Inorganic Chemistry* **2008,** *47*, 1849.
39. Ballhausen, C. J.; Gray, H. B., *Inorganic Chemistry* **1962,** *1*, 111.
40. Zhou, S.; Miao, X.; Zhao, X.; Ma, C.; Qiu, Y.; Hu, Z.; Zhao, J.; Shi, L.; Zeng, J., *Nature Communications* **2016,** *7*.

41. Hinogami, R.; Toyoda, K.; Aizawa, M.; Yoshii, S.; Kawasaki, T.; Gyoten, H., *Electrochemistry Communications* **2013,** *35*, 142.
42. Kanan, M. W.; Nocera, D. G., *Science* **2008,** *321*, 1072.
43. Lutterman, D. A.; Surendranath, Y.; Nocera, D. G., *Journal of the American Chemical Society* **2009,** *131*, 3838.
44. Risch, M.; Ringleb, F.; Khare, V.; Chernev, P.; Zaharieva, I.; Dau, H. In *Characterisation of a water-oxidizing Co-film by XAFS*, Journal of Physics: Conference Series, IOP Publishing: 2009; p 012167.
45. Zhang, M.; de Respinis, M.; Frei, H., *Nature chemistry* **2014,** *6*, 362.
46. Bergmann, A.; Martinez-Moreno, E.; Teschner, D.; Chernev, P.; Gliech, M.; De Araújo, J. F.; Reier, T.; Dau, H.; Strasser, P., *Nature Communications* **2015,***6*, 8625.
47. Chen, J.; Wu, X.; Selloni, A., *Physical Review B* **2011,** *83*, 245204.
48. Roth, W., *Journal of Physics and Chemistry of Solids* **1964,** *25*, 1.
49. Ohnishi, S.; Sugano, S., *Journal of Physics C-Solid State Physics* **1981,***14*, 39.
50. Kim, K. J.; Park, Y. R., *Solid State Communications* **2003,** *127*, 25.
51. Shinde, V. R.; Mahadik, S. B.; Gujar, T. P.; Lokhande, C. D., *Applied Surface Science* **2006,** *252*, 7487.
52. Vijayanand, S.; Kannan, R.; Potdar, H. S.; Pillai, V. K.; Joy, P. A., *Journal of Applied Electrochemistry* **2013,** *43*, 995.
53. Patil, D.; Patil, P.; Subramanian, V.; Joy, P. A.; Potdar, H. S., *Talanta* **2010,***81*, 37.
54. Kshirsagar, V. S.; Vijayanand, S.; Potdar, H. S.; Joy, P. A.; Patil, K. R.; Rode, C. V., *Chemistry letters* **2008,** *37*, 310.
55. Liang, Y.; Li, Y.; Wang, H.; Zhou, J.; Wang, J.; Regier, T.; Dai, H., *Nature Materials* **2011,** *10*, 780.
56. Gao, S.; Jiao, X.; Sun, Z.; Zhang, W.; Sun, Y.; Wang, C.; Hu, Q.; Zu, X.; Yang, F.; Yang, S.; Liang, L.; Wu, J.; Xie, Y., *Angewandte Chemie International Edition* **2016,** *55*, 698.
57. Xie, X.; Li, Y.; Liu, Z.-Q.; Haruta, M.; Shen, W., *Nature* **2009,** *458*, 746.
58. Esswein, A. J.; McMurdo, M. J.; Ross, P. N.; Bell, A. T.; Tilley, T. D., *The Journal of Physical Chemistry C* **2009,** *113*, 15068.
59. Minguzzi, A.; Fan, F.-R. F.; Vertova, A.; Rondinini, S.; Bard, A. J., *Chemical Science* **2012,** *3*, 217.

Chapter 2

Experimental Methods

2.1 Introduction

This chapter describes the method of synthesis used for the materials studied in the present work, characterization techniques used and the details about the electrochemical techniques. Various soft chemical methods like coprecipitation, autocombustion, hydrothermal, sol-gel and citrate gel methods are available for the synthesis functional oxide nanomaterials [1-5]. In the present work, a modified coprecipitation/digestion method, followed by calcination, was used to synthesize Co_3O_4 nanorods. Autocombustion method was used to synthesize nanoparticles of cobalt oxide and substituted cobalt oxides.

2.2 Synthesis

2.2.1 Coprecipitation

Coprecipitation is one of the soft chemical methods used for the synthesis of metal oxide nanomaterials by forming a precipitate from aqueous solutions. Corresponding metal precursors in the form of nitrates, chlorides, sulphates, etc. are used for the precipitation using a precipitating agent. Depending on the precipitating agent, metal oxides are obtained directly or precursors in the form of hydroxide or carbonate, etc. are obtained which after calcination at a suitable temperature, produce the corresponding metal oxide.

Nucleation, growth and agglomeration are the major steps involved in the coprecipitation reaction. During the nucleation process, numerous small particles are formed and become sparingly soluble, which leads to supersaturation. Usually, supersaturation can be induced by various parameters like pressure, temperature, concentration and chemical reaction. The formed particles tend to grow/aggregate together either by the Oswald ripening process or through the oriental attachment to minimize the energy and to become thermodynamically stable. If the crystallinity of the precursor is improved during precipitation, the high energy facets will attach together and orient to give morphologically controlled precursors. These precursors retain the morphology even after calcination in air to form the corresponding metal oxides.

In the present work, Co_3O_4 nanorods were prepared by the coprecipitation/digestion method, as reported in the literature from our group [6]. According to this method, 100 ml of distilled water was taken in a three-necked round bottom flask (RBF) and purged with argon gas for 1 hour to remove the excess oxygen present. The distilled water was then slowly heated to 70ºC on a heating mantle. Two 250 ml separating funnels containing 0.0339 M of

$Co(NO_3)_2.6H_2O$ solution and 0.0627 M of K_2CO_3 solution were connected on the two necks of the RBF, and a water condenser was connected to the third neck. The two solutions were added simultaneously to the water, heated in the RBF. Concentrations of the acidic and basic solutions were optimized through trial experiments for maintaining the pH in the range 7 to 8. The precipitate obtained after completion of addition was digested in the mother liquor, at the same temperature, for 8hours. The precipitate formed was thoroughly washed with distilled water, several times, to avoid K^+ ion contamination and further dried in an oven at 70 ºC, overnight. The obtained precursor wasidentified as cobalt hydroxy carbonate, and it was calcined at 300 ºC for 5 hours in the air, to obtain the cobalt oxide, as reported [6].

2.2.2 Autocombustion method

Autocombustion method is one of the simplest and cost effective methods to synthesize metal oxide nanoparticles. It is also known as self propagating high temperature synthesis (SHS) or fire synthesis [7-8]. The exothermicity of the redox reaction is utilized for the synthesis of metal oxides. This synthesis method has many advantages over other methods, such as low temperatures used, short reaction time, homogeneous powders due to the molecular level mixing of the metal ions, large scale preparation possible, fine particle nature of the products obtained, etc. In this method, glycine, urea, citric acid, hydrazine, etc are used as fuels and metal nitrates are used as oxidizing agents [8-10]. In the solution-combustion method, the redox mixture solution contains an oxidizer and a fuel [11-12]. In this method, a mixed solution of the aqueous solutions of stoichiometric amounts of metal nitrates and fuels like urea, glycine is heated rapidly. The fuel is the source of C and H and gets converted in to CO_2 and H_2O during the combustion reaction and liberates heat.

In the present study, the glycine-nitrate process (GNP) [13] has been used to synthesize nanosized cobalt oxides. Glycine molecule has the Zwitter-ionic character, in which one end has a carboxyl group and another end has the amino group [13]. Therefore, it can form complex with metal ions with various sizes, effectively. During the combustion reaction, glycine will act as the fuel. The fuel/oxidizer ratio mainly governs the powder characteristics such as crystallite size, surface area, agglomeration, etc. Theoretically calculated ratios of metal nitrate to fuel for divalent and trivalent metal ions are given in equation 2.1 and equation 2.2.

$$M(NO_3)_2 + \frac{10}{9}C_2H_5O_2N = MO + \frac{20}{9}CO_2 + \frac{25}{9}H_2O + \frac{14}{9}N_2 \quad 2.1$$

$$2M(NO_3)_3 + \frac{30}{9}C_2H_5O_2N = M_2O_3 + \frac{60}{9}CO_2 + \frac{75}{9}H_2O + \frac{49}{9}N_2 \quad 2.2$$

In the present work, corresponding metal nitrates of AR grade have been used for the synthesis of metal oxide in a single step. Required amounts of metal nitrate and glycine were dissolved in minimum amount of water, separately, mixed together and sonicated for 15 minutes to achieve a homogeneous solution. The homogeneous mixed solution was taken in a crystallizing dish (150 mm x 75 mm) and kept on a hot plate with controlled heating. After evaporation of water, there will be gelation followed by self-ignition to yield the corresponding oxides in a single step. It is reported that the particle size of the resulting metal oxide can be controlled by decreasing the amount of glycine used for the reaction. Hence, the lowest possible metal-to-glycine ratio was used, optimized by trial experiments, for each synthesis to get single phase materials with very small particle size.

2.3 Characterization

2.3.1 Powder X-Ray Diffraction

Powder X-ray diffraction (XRD) is the very basic and widely used characterization tool available for phase identification of crystalline materials. The XRD pattern of a crystalline material is the fingerprint for that material, and it gives information about the structure and phase purity [14-15]. The basic operative principle of XRD is the Bragg's Law, given by

$$n\lambda = 2dsin\theta \quad 2.3$$

where, λ is the incident X-ray wavelength, 'n' is an integer, 'd' is the inter-planar spacing in a crystal and θ is the angle of an incidence of X-rays.

The peaks in an XRD pattern becomes broader for nanomaterials, and varies with the crystallite size, compared to that of the bulk counterpart, due to the smaller crystallite size of nanomaterials. The average crystallite size (*t*) of a nanomaterial can be calculated using the Scherrer equation [16].

$$t = \frac{K\lambda}{\beta \cos\theta} \qquad 2.4$$

where, K is the constant and depends on the shape of the nanomaterials (0.9 for spherical particles), λ is the wavelength of the X-rays used, θ is the Bragg angle, and β is the full width at half maximum (FWHM) of a peak after correcting for the instrumental contribution to the peak broadening.

In the present study, powder X-ray diffraction patterns were collected on PANalytical XPERT PRO model X-ray diffractometer, Cu Kα (1.5418 Å) radiation was used as the X-ray source, and Ni acted as a filter. XRD patterns of the synthesized samples were recorded in the 2θ range 10-80 degrees at the scan rate of 1.17 degrees/minute. The XRD pattern of known compounds was simulated using the computer program called 'Powder Cell for Windows (PCW)' version 2.4 [17]. The space group, unit cell lattice parameters, atomic positions and occupancy parameter are used as input parameters. The experimental pattern was compared with the simulated pattern and also with the standard Joint Committee on Powder Diffraction Standards (JCPDS) data.

2.3.2 Transmission electron microscopy (TEM)

Transmission electron microscopy (TEM) is the best technique used to study the microstructure of a sample. The TEM instrument works based on the same principles of light microscopy, the most important differences is that an electron beam is used instead of light waves because the smaller size of electron provide better resolution than a light microscope. A beam of electrons is focused onto a sample and the resulting image formed by the transmitted electrons is captured on a fluorescent screen/CCD camera. TEM analysis is a useful technique to determine particle size, shape, and distribution of particle size [18-19].

TEM analysis in the present work was carried out on a FEI model TECNAI G2 F30 transmission electron microscope operated at an accelerating voltage of 300 kV (CS = 0.6 mm, resolution = 1.7 Å). For the TEM analysis, samples were prepared by dispersing the dried nanoparticles in a small amount of low boiling organic solvent by sonication and dropped onto a carbon coated copper grid (200 mesh). All the collected TEM images were analyzed by using the digital micrograph software available on the instrument.

2.3.3 X-Ray photoelectron spectroscopy (XPS)

XPS is a surface analytical technique, and it is also called as Electron Spectroscopy for Chemical Analysis (ESCA) [20-21]. XPS is based on the photoelectric effect. The photoelectric effect is the emission of an electron upon X-rays falling on a solid surface. The kinetic energy (KE) of the emitted electron is measured by the electron spectrometer, the binding energy(BE) of the electron is calculated using the kinetic energy of the ejected electron and the energy of X – ray sources being used, as

$$BE = h\nu - (KE + \phi) \qquad 2.5$$

where BE is the binding energy of the element/ion present in the sample, hν is the energy of X–rays being used, KE is the kinetic energy of the emitted electrons, and ϕ is the work function.

All the XPS studies in the present work have been carried out on a model VG Microtech Multilab ESCA 3000 spectrometer using a non-monochromatized Mg Kα source, hν = 1253.6 eV with a base pressure in the analysis chamber as 4×10^{-10} Torr. The overall energy resolution of the instrument is determined from the full width at half maximum of the $4f_{7/2}$ core level of gold surface, and it was found to be about 0.7 eV. In addition to this, all the binding energies of insulating samples were corrected using the C peak of carbon with the binding energy value of 285.00 eV as the reference.

2.3.4 BET analysis

Solids substance may be porous or non-porous in nature, The pores are classified into three major types such as macroporous (diameter above 50 nm), mesoporous (diameter 2-50 nm) and microporous (diameter less than 2 nm), depending on the size of the pores present within the solids. It is important to know the number of adsorbate molecules in a monolayer and the area of cross section of the adsorbate molecule, which are used to get information about the surface area of that solid, given by

$$Surface\ area = \frac{v_m\, N}{22414}\, Am \times 10^{-20} m^2 \qquad 2.6$$

Where $v_m$the volume of the adsorbate molecules in a monolayer, N is is the Avogadro's number and Am is the area of cross section of the adsorbate molecule.

Brunauer-Emmett-Teller (BET) equation was used for calculating the monolayer capacity (in volume) of a solid, given by

$$\frac{P}{v\,(P_0 - P)} = \frac{1}{Cv_m} + \frac{(C-1)P}{Cv_m P_0} \qquad 2.7$$

where P and P_0 are the pressure at equilibrium and saturation vapour pressure at the experimental condition, respectively.v and v_m are the volume of the adsorbate molecules at pressure p and in the monolayer, respectively. C is a positive constant.

Equation 2.7 gives a straight line with $\frac{P}{v\,(P_0-P)}$ on y-axis and $\frac{P}{P_0}$ on x-axis. $v, v_m$and C are calculated from the slope and intercept of the plotted straight line.

The surface area measurements of the samples in the present work were carried out using a Micromeritics NOVA 1200 (Quanta Chrome) instrument using N_2 gas as the adsorbate molecules.

2.3.5 Magnetic measurements

The magnetic characteristics of materials as a function of applied field at different temperatures and as a function of temperature at different applied field strengths can be studied using a vibrating sample magnetometer (VSM). The instrument allows precise magnetization measurements to be made as a function of magnetic field strength, temperature and crystallographic orientation. The working principle of a VSM is based on the Faraday's law, where an electromotive force (*emf*) is induced in a conductor by a time varying magnetic flux [23-24].

In the present study, a Quantum Design MPMS 7T SQUID-VSM was used for all the magnetic measurements. SQUID assembly has a superconducting ring with two Josephson junctions. When a change in magnetic flux is brought about, it generates a voltage and a current in the ring which gets added and subtracted to the measuring current at two Josephson junctions. This induces a resistance change and a voltage across the superconducting loop.

The SQUID assembly thus becomes highly sensitive, giving a field sensitivity of 2×10^{-15} Tm^2.

In the present study, magnetization as a function of temperature was measured in the range 2–300 K, in an applied field of 1 Tesla. The magnetic susceptibility, χ, is calculated as χ = M/H where M is the measured magnetization at a particular temperature and H is the applied field. The relation between susceptibility and temperature is given by the Curie-Weiss law. According to the Curie-Weiss law, the susceptibility

$$\chi = \frac{C}{T - \Theta} \qquad 2.8$$

where C is the curie constant and Θ is the Weiss constant which is proportional to the molecular field. Θ can be zero (for paramagnetic) or positive (for ferromagnetic) or negative (for antiferromagnetic). From the Curie constant, C, the number of unpaired electrons can be calculated from the equation

$$C = Ng^2\mu_B{}^2 S (S+1)/3k \qquad 2.9$$

where N is the Avogadro number, g is g-factor (= 2), k is the Boltzmann constant and μ_B is Bohr magneton, the unit for the magnetic moment of an electron.

2.3.6 UV-Visible spectroscopy

UV-Visible spectroscopy investigates the interactions between ultraviolet or visible electromagnetic radiation and matter. UV-visible spectroscopy refers to the absorption spectroscopy in the Ultraviolet-visible region. Diffuse reflectance spectroscopy is used to analyze the optical properties of powdered crystalline samples. Diffuse reflectance relies upon the focused projection of the spectrometer beam into the sample where it is reflected, scattered and transmitted through a material. The back-reflected, diffusely scattered light (some of which is absorbed by the sample) is then collected by the accessories (integrating sphere attachment) and directed to the detector optics. Only the part of the beam that is scattered within a sample and returned to the surface is considered to be diffuse reflection. The spectral reflectance component in the diffuse reflectance spectra causes changes in the band shapes, their relative intensities, and, in some cases it is also responsible for the complete band inversion. Dilution of a sample with a non-absorbing matrix minimizes these effects. Dilution increases the penetration of the incident beam into the sample, which increases the scattered component contribution in the spectrum and minimizes the specular

reflection component. Kubelka-Munk conversion can be applied to a diffuse-reflectance spectrum to compensate for these differences. The Kubelka-Munk equation is given by [25]:

$$f(R) = \frac{1-(R^2)}{2R} = \frac{k}{S} \qquad 2.10$$

where R is the absolute reflectance of the sampled layer, K is the molar absorption coefficient and S is the scattering coefficient. The Kubelka-Munk equation creates a linear relationship for spectral intensity relative to sample concentration. It assumes infinite sample dilution in a non-absorbing matrix, a constant scattering coefficient and an "infinitely thick" sample layer.

For the present study, Shimadzu UV 3600 plus UV Vis NIR spectrophotometer has been used. The obtained data is deconvoluted using PeakFit software [26].

2.4 Electrochemical characterizations

2.4.1 Electrochemical methods

All the electrochemical measurements were carried out using CH Instruments 400a or CH Instruments 660b or Solartron (EI 1287 and FRA 1255B). Particularly, impedance measurements were carried out in on the Solartron instruments. Glassy carbon electrode (3 mm diameter) is used as the working electrode and a platinum foil is used as the counter electrode. For neutral and acidic conditions, a calomel (0.1 M KCl) electrode and for basic condition Hg/HgO (0.1 M KOH) electrode are used as the reference electrodes.

2.4.2 Preparation of catalyst ink

All the catalysts used in this study are semiconductors, having low electronic conductivity. To rectify this problem, Vulcan carbon is added to the catalyst in the ratio 80:20. The catalyst-carbon mixture is dispersed in ethanol-water mixture (3:2). In addition, nafion solution dispersed in isopropyl alcohol was added as a binder, which prevents the catalyst coming out from the electrode surface during the electrochemical measurements. In the present study, 4 mg of catalyst and 1 mg of Vulcan carbon is mixed with 160 µL of 0.2% nafion solution and the volume is made up to 1 mL by adding 3:2 ethanol water mixture. The solution is sonicated for 15 minuted for homogeneous dispersion. From this catalyst ink, 18 µL coated on the glassy carbon electrode (3 mm dia) and dried under a lamp. This catalyst

coated electrode is used for all the measurements such as cyclic voltammetry, Tafel plots and impedance measurements.

2.4.3 Tafel plot data collection

The data for Tafel plot were collected galvanostatically. Since cobalt oxides are well known for their capacitive properties, the contribution of capacitive current may add up to the catalytic current. To avoid this error, galvanostatic mode is followed to collect the data points for the Tafel plot. According to this method, a current is applied for 300 s. The potential is slowly increased and saturated once the capacitance from the electrode material is vanished. The potential is noted after the saturation. In this manner, current is applied in the range of 10^{-7} A/cm^2 to 10^{-3} A/cm^2 and the respective potential values are noted. Throughout the measurement, the electrolyte solution is stirred at 400 rpm to avoid the effect of mass transport and the concentration gradient.

2.4.4 Quantitative oxygen evolution

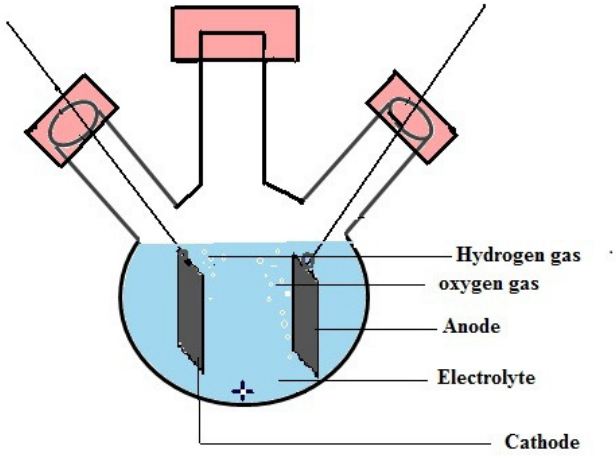

Figure 2.1 Three neck electrochemical cell setup for collecting evolved gas

SS316 mesh is used as the electrode material. The prepared catalyst ink is coated on the surface of SS316 mesh and dried under a lamp. The catalyst loading was 1 mg/cm^2. The catalyst coated electrode is inserted through one of the necks with the help of rubber septum. In the same way, a platinum electrode is inserted in the other neck with airtight rubber septum. Then the RBF is filled with the electrolyte till 3/4 of its total volume. The electrolyte

is vigorously purged with nitrogen gas to remove the dissolved oxygen from the electrolyte. During the purging, the middle neck is closed with an airtight rubber septum and sealed with teflon tape. The air in the RBF is collected immediately in a 10 µL airtight syringe and injected to the gas chromatography, to confirm the absence of oxygen in the setup. Then, a constant current is applied galvanostatically for 8 hrs and the solution is stirred to avoid the accumulation of produced gas bubbles at the electrode surface. The evolved gas is collected from the cell using the syringe, at every 2 hour interval, and injected in the gas chromatography to analyse the produced gas mixture for quantification of hydrogen and oxygen. Agilent 7890 GC system with a TCD detector is used for the analysis of the gas mixture. The analyzed gas mixture gives peak for the hydrogen and oxygen with the retention

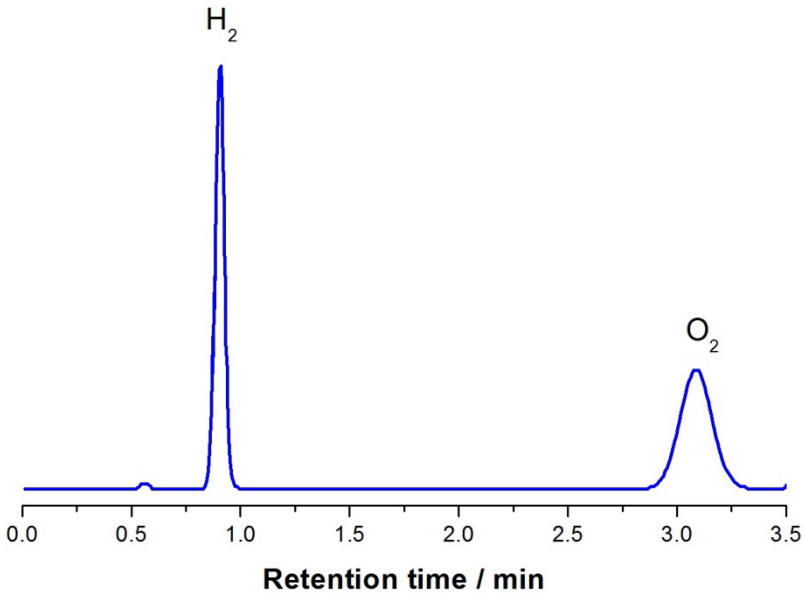

Figure 2.2 Analysis of evolved gas by Gas Chromatography (GC)

time 0.9 min and 3.1 min respectively (Figure 2.2). The quantity of the both the gases are calculated from the area of the respective peaks.

According to the Faraday's second law of electrolysis, the amount of oxygen produced is directly proportional to the amount of charge passed,

$$m = Q / nF \qquad 2.10$$

where ‘m’ is the number of moles of oxygen, Q is the total charge passed to the cell, ‘n’ is the number of electrons transferred in the electrode reaction and F is the Faraday constant. Oxygen evolution is a four electron transfer reaction. Thus, the Faradaic efficiency is calculated as nO_2 / (Q /4F).

References:

1. Jean-Pierre, J.; Henry, M.; Livage, J., *Metal oxide chemistry and synthesis: from solution to solid state*. Wiley-Blackwell: 2000.
2. Abbott, E. H.; Rao, C., *Journal of the American Chemical Society* **1995,** *117*, 10604.
3. Patil, K., *Chemistry of nanocrystalline oxide materials: combustion synthesis, properties and applications*. World Scientific: 2008.
4. Segal, D., *Chemical synthesis of advanced ceramic materials*. Cambridge University Press: 1991; Vol. 1.
5. Segal, D., *Journal of Materials Chemistry* **1997,** *7*, 1297.
6. Patil, D.; Patil, P.; Subramanian, V.; Joy, P. A.; Potdar, H. S., *Talanta* **2010,** *81*, 37.
7. Moore, J. J.; Feng, H. J., *Progress in Materials Science* **1995,** *39*, 243.
8. Moore, J. J.; Feng, H. J., *Progress in Materials Science* **1995,** *39*, 275.
9. Costa, A.; Tortella, E.; Morelli, M.; Kiminami, R., *Journal of magnetism and magnetic materials* **2003,** *256*, 174.
10. Sileo, E. E.; Rotelo, R.; Jacobo, S. E., *Physica B: Condensed Matter* **2002,** *320*, 257.
11. Patil, K. C.; Aruna, S. T.; Ekambaram, S., *Current Opinion in Solid State and Materials Science* **1997,** *2*, 158.
12. Patil, K. C.; Aruna, S. T.; Mimani, T., *Current Opinion in Solid State and Materials Science* **2002,** *6*, 507.
13. Chick, L. A.; Pederson, L.; Maupin, G.; Bates, J.; Thomas, L.; Exarhos, G., *Materials Letters* **1990,** *10*, 6.
14. Cullity, B. D.; Stock, R. S., *Elements of X-ray Diffraction*. Addison-Wesley Reading, MA: 1978.
15. Klug, H. P.; Alexander, L. E., *X-ray diffraction procedures*. 1954.
16. Patterson, A. L., *Physical Review* **1939,** *56*, 978.
17. The software is freely available from http://www.ccp14.ac.uk.
18. Thomas, G., Transmission electron microscopy of metals. John Wiley & Sons Inc: 1962.

19. Williams, D. B.; Carter, B., *Transmission Electron Microscopy IV: Spectrometry*. Plenum Press: 1996.
20. Somorjai, G. A.; Li, Y., *Introduction to surface chemistry and catalysis*. John Wiley & Sons: 2010.
21. Watts, J. F.; Wolstenholme, J., *An introduction to surface analysis by XPS and AES*. 2003
22. Lowell, S.; Shields, J. E.; Thomas, M. A.; Thommes, M., *Characterization of porous solids and powders: surface area, pore size and density*. Springer Science & Business Media: 2012; Vol. 16.
23. Cullity, B. D.; Graham, C. D., *Introduction to magnetic materials*. John Wiley & Sons: 2011.
24. Foner, S., *Review of Scientific Instruments* **1959,** *30*, 548.
25. Džimbeg-Malčić, V.; Barbarić-Mikočević, Ž.; Itrić, K., *Tehnički vjesnik* **2011,***18*, 117.
26. http://www.sigmaplot.co.uk/products/peakfit/peakfit.php

Chapter 3

Nanostructured Co_3O_4 for electrochemical oxygen evolution

3.1 Introduction

Oxygen evolution reaction (OER) is the key step and high energy consuming reaction in the electrochemical water splitting for the production of the high energy density fuel, hydrogen. At present, Ru- and Ir-based oxide compounds are used widely as the anode materials for the oxygen evolution reaction. Recent research work has been focused on developing non-precious metal oxides for the oxygen evolution to reduce the capital cost of hydrogen production [1]. In particular, nanostructures of earth abundant transition metal oxides are shown to have promising catalytic activities for oxygen evolution, compared to the precious metal oxides such as RuO_2 and IrO_2. However, the working conditions such as high temperature and the alkaline medium corrode the electrode material as well as the experimental setup. To resolve this, ideally, a rationally engineered electrocatalyst should, therefore, work near neutral pH with lower overpotential at room temperature. Also, the material should have good activity and stability in the electrolyte solution and have to be environmentally benign for safer use, along with lower cost and higher abundance.

Not many studies are reported in the literature on water splitting in neutral electrolyte solutions, due to the instability of the catalysts in the neutral medium. Nocera and his group reported neutral and benign environment-efficient catalysts for oxygen evolution, like cobalt based polyoxometalate/phosphate (denoted as Co-Pi) and nickel boride (denoted as Ni-B_i) [2-3]. Ahn and Tilley have reported nanostructured $Co(PO_3)_2$ as anode material for oxygen evolution at neutral pH, at an overpotential of 310 mV at 1 mA/cm^2 [4]. Zhao *et al* has studied WO_3/Ag-B based oxygen evolution catalyst which works under mild conditions for water oxidation [5]. In fact, it is a great challenge to enhance the activity and stability of a catalyst near neutral medium, because most of the transition metal oxides are not stable in a neutral medium under water oxidation conditions [6].

It has been proved that the simultaneous presence of both lower and higher oxidation states of metal is essential for efficient OER catalysts [7]. Spinel- and perovskite-type oxides are well known for OER (mostly in an alkaline medium) because of their stability and catalytic activity which result from the mixed-valent nature of the metal ions involved in such oxides [8-9]. Among the reported mixed valence compounds for oxygen evolution, the spinel-type oxide Co_3O_4 has received much attention due to its favorable redox property, thermodynamic stability and electrocatalytic properties [10].

The spinel-type transition metal oxide Co_3O_4 is a p-type magnetic semiconductor with a wide range of applications in many technological important areas such as heterogeneous catalysis, anode material in lithium rechargeable batteries, supercapacitors, sensors, solar energy absorber, electrochromic devices, etc. Co_3O_4 has Co^{3+} in the octahedral sites and Co^{2+} in the tetrahedral sites. Different nanostructures and morphologies of Co_3O_4 have been reported as catalysts for the oxygen evolution reaction in alkaline medium. Sun *et al* reported atomically thin 'non-layered' cobalt oxide porous sheets as a catalyst for oxygen evolution due to the low coordinated Co^{3+} active sites on the surface [11]. Studies on the effect of the size of Co_3O_4 on oxygen evolution showed that reducing the particle size with increasing the surface area improves the catalytic activity [12-13]. Likewise, Co_3O_4 nanostructures with highly reactive crystal planes are even more attractive due to their excellent electronic properties and catalytic activities as well as electrochemical energy conversion [14-15]. For example, Co_3O_4 with the exposed (110) surfaces, where the density of Co^{3+} is shown to be larger when compared to the other crystal planes, show enhanced catalytic activity for CO oxidation and high storage capacity in lithium ion batteries [16-18]. The higher catalytic activity for CO oxidation is ascribed to preferential adsorption of the reactant molecules on the octahedrally coordinated Co^{3+} ions. Octahedral Co^{3+} plays an important role in the mechanism of OER, which acts an active site. The conversion of Co(III)-OH to Co(IV)-OH is associated with the O-O bond formation [19]. Also, the significant role of tetrahedral Co^{2+} is also identified from the *in situ* spectroscopic studies on Co_3O_4 for the OER [20]. Tetrahedral Co^{2+} in Co_3O_4 initiates the formation of μ-OO peroxide moieties which is the key intermediate in the mechanism of four-electron transfer OER [20].

Our group has earlier synthesized morphological controlled, porous Co_3O_4 nanorods by a template-free co-precipitation digestion method. The porous Co_3O_4 nanorods have been shown to be efficient for applications in a supercapacitor, Li-ion battery, CO sensor and catalytic oxidation of p-cresol [21-23].This chapter describes studies on the electrocatalytic activity of porous Co_3O_4 nanorods for oxygen evolution reaction. The results using the nanorods are also compared using Co_3O_4 nanoparticles. Morphology-controlled Co_3O_4 nanorods are obtained through a co-precipitation digestion method by adapting optimized synthetic conditions, as reported previously, and the nanoparticles are synthesized by an autocombustion method. The objective of the work is to study the intrinsic role of Co_3O_4 as a catalyst for the oxygen evolution reaction and to compare the difference in the morphologies of the nanostructures in the OER.

3.2 Studies on Co_3O_4 nanorods

A detailed electrocatalytic property of Co_3O_4 nanorods for the oxygen evolution reaction at different pH ranging from 4 to 14 is studied. More significantly, the stability of the catalyst has been studied in the acidic and neutral medium, where the catalyst is usually prone to corrosive attack resulting in thermodynamic instability of the catalyst.

3.2.1 Synthesis

Co_3O_4 nanorods were prepared by the coprecipitation-digestion method, as reported earlier [22]. Analytical grade $Co(NO_3)_2.6H_2O$ and K_2CO_3 were used as the starting materials. Initially, 100 ml of distilled water was taken in a three-necked round bottom flask (RBF) and purged with argon gas for 1 hour to remove the excess oxygen present. The distilled water was then slowly heated to 70 ºC on a heating mantle. Two 250 ml separating funnels containing 0.0339 M of $Co(NO_3)_2.6H_2O$ solution and 0.0627 M of K_2CO_3 solution were connected on the two necks of the RBF, and a water condenser was connected to the third neck. The two solutions were added simultaneously to the water, heated in the RBF. Concentrations of the acidic and basic solutions were optimized through trial experiments for maintaining the pH in the range 7 to 8. The precipitate obtained after completion of addition was digested in the mother liquor, at the same temperature, for 8 hours. The precipitate formed was thoroughly washed with distilled water, several times, to avoid K^+ ion contamination and further dried in an oven at 70 ºC, overnight. The obtained precursor wasidentified as cobalt hydroxy carbonate [22], and it was calcined at 300 ºC for 5 hours in the air, to obtain the cobalt oxide.

3.2.2 X-ray diffraction

The XRD pattern of the synthesized Co_3O_4 is shown in Figure 3.1. The experimental pattern is compared with the simulated pattern of Co_3O_4. The powder XRD pattern is simulated using the PCW software and the crystallographic parameters of Co_3O_4 for space group Fd3m and the cubic lattice parameter a = 8.0840 Å (JCPDS # 09-0418). All the peaks in the experimental pattern match with that in the simulated pattern, suggesting the formation of Co_3O_4 in single phase form without any impurities. The lattice parameter is calculated as 8.077 Å by least-squares fitting of the experimental pattern and is in good agreement with the reported value for Co_3O_4 (a = 8.0840 Å, JCPDS # 09-0418). The relatively broader peaks in the experimental pattern indicate nanocrystalline nature of the sample. The average crystallite

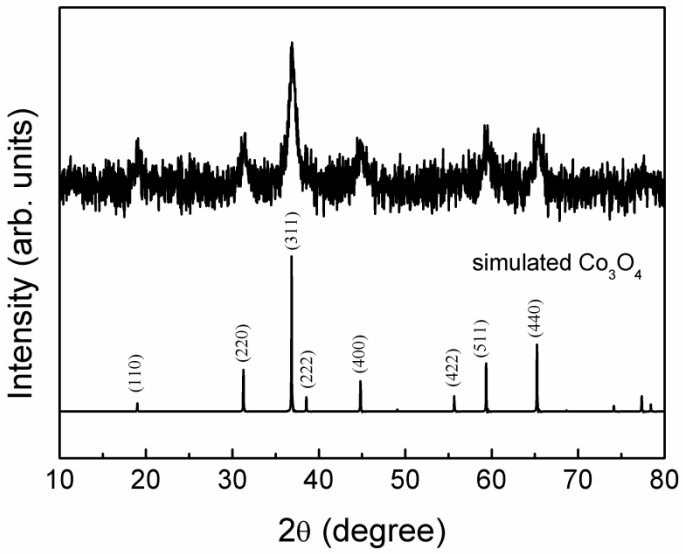

Figure 3.1 Powder XRD patterns of the Co_3O_4 nanorods, compared with the simulated pattern

size is calculated from the full width at half maxima (FWHM) of the major peak (311) using the Scherrer formula (section 2.3.1, chapter 2) as 11±1 nm.

3.3.3 TEM studies

The TEM images shown in Figure 3.2 reveal the morphological features of the Co_3O_4 nanorods. The average length of the rods is obtained as 20–30 nm with a diameter of 6–8 nm. Also, these nanorods are composed of spherical particles. The observed d-spacing in the lattice fringes, as shown in Figure 3.2(b) & (d) matches with the d-spacing of (220) atomic plane. In the conventional coprecipitation synthesis of fcc metal oxides, the preferred morphology or the equilibrium shape is truncated cuboctahedron with (111) and (100) planes at the surfaces as predicted by Wulff construction [24]. This is due to the low surface energy of these planes and hence the lower surface free energy of the desired structure, where the surface energy of the planes increases in the order $\gamma_{111}<\gamma_{100}<\gamma_{110}$. However, a different shape other than the equilibrium shape can be attained under a definite driving force like supersaturation and temperature [24]. In the present case, the rod-shaped cobalt hydroxy carbonate precursor was synthesized and further converted to Co_3O_4 nanorods after calcination. Here, the carbonate anions might have acted as a structure directing agent during

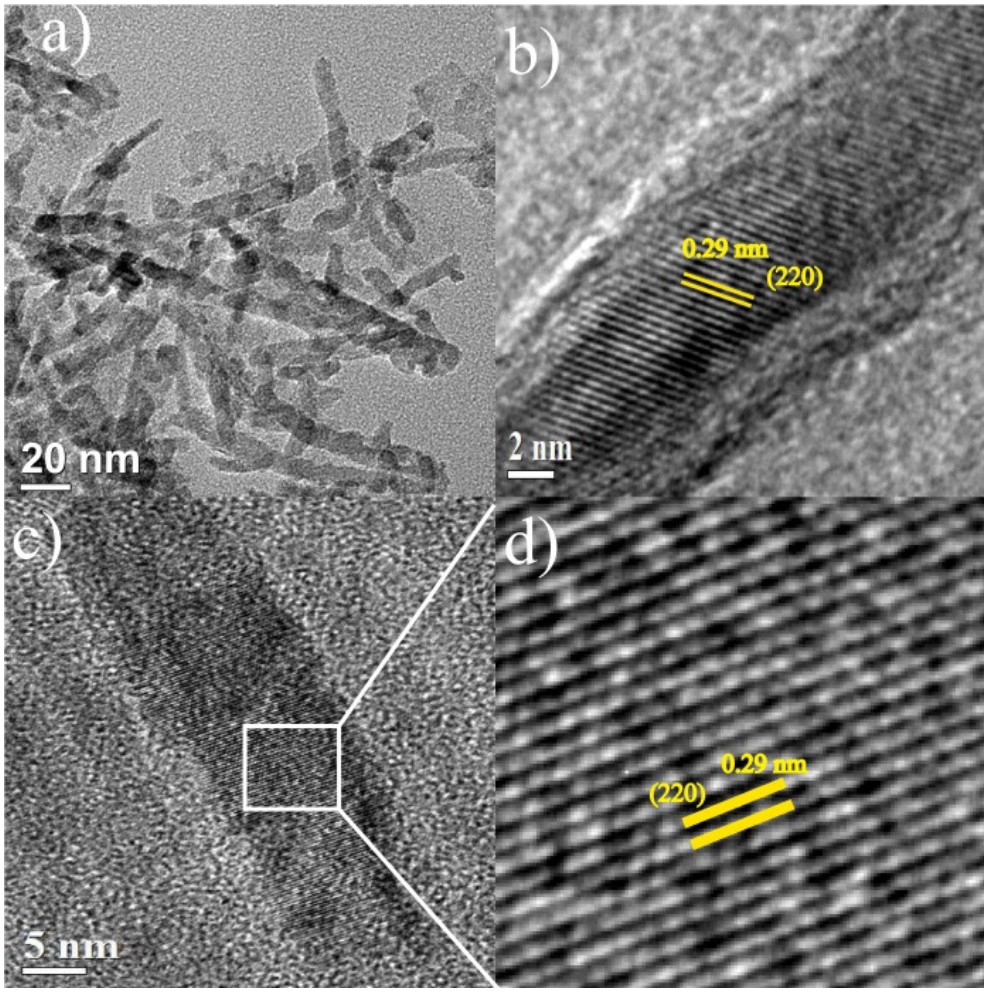

Figure 3.2 TEM images of Co_3O_4 nanorods (a,b,c), and (d) is the magnified image of (c)

the formation of the oxide which inhibited the crystal growth in the particular direction by specific adsorption in the planes [15]. Hence, the crystal is allowed to grow only in certain directions, and forms elongated nanorods in the (110) direction, as evident from the TEM images.

3.2.4 Surface area and porosity

To get information about the surface area and the nature of pores, the calcined cobalt oxide was subjected to Brunauer-Emmett-Teller (BET) surface area measurements. Figure 3.3 shows hysteresis loop of nitrogen adsorption-desorption isotherm of Co_3O_4 nanorods. The shape of the hysteresis loop confirms type IV isotherm [25], and indicate the porous nature of the material. The surface area is obtained as 100 m^2/g. The inset in Figure 3.3 shows the pore size distribution in the range of 2-10 nm. All these results indicate the formation of highly

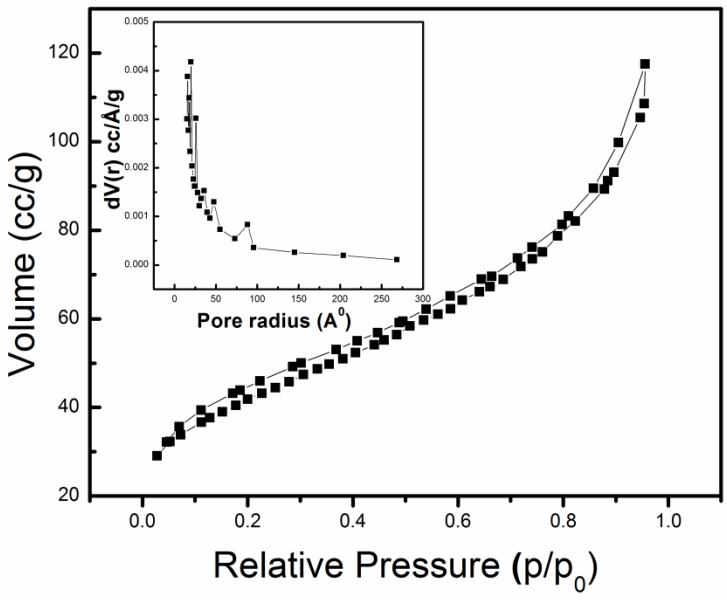

Figure 3.3 Nitrogen adsorption-desorption curve of Co_3O_4 nanorods. Inset: pore size distribution

porous nanorods with the very high surface area and sharp pore size distribution, which is a key requirement for many technologically important applications, including electrochemical water splitting.

3.2.5 Cyclic voltammetry

The electrochemical and redox properties of the catalyst can be well studied by cyclic voltammetry technique. The prepared catalyst ink (section 2.4.2, Chapter 2) is coated on a 3 mm diameter glassy carbon electrode, and standard calomel electrode (0.1 M KCl) is used as the reference electrode. 0.1 M KH_2PO_4 was used as the electrolyte, for pH 4. For pH 7, the electrolyte was made by mixing 42.2 ml of 0.1 M KH_2PO_4 and 57.8 ml of 0.1 M K_2HPO_4 to obtain 100 ml of phosphate buffer according to the Henderson-Hasselbalch equation [26]. 0.1 M KOH solution is used as the electrolyte for pH = 13. Figure 3.4 shows comparative cyclic voltammograms of Co_3O_4 nanorods at different pH (using 0.1 M phosphate buffer for pH 4 and pH 7 and 0.1 M KOH for pH 13) with different scan rates revealing many remarkable features corresponding to the fingerprint of Co_3O_4 [27]. All the voltammograms show two oxidation peaks A1 and A2 which have been assigned to oxidation of Co^{2+} to Co^{3+} and $Co^{3+}$to Co^{4+}, respectively, and peak C1 corresponds to the reduction of Co^{4+} to Co^{3+} as reported [28-29]. Further, the peak in the cathodic region at less positive potentials can be ascribed to the reduction of Co^{3+} to Co^{2+}.

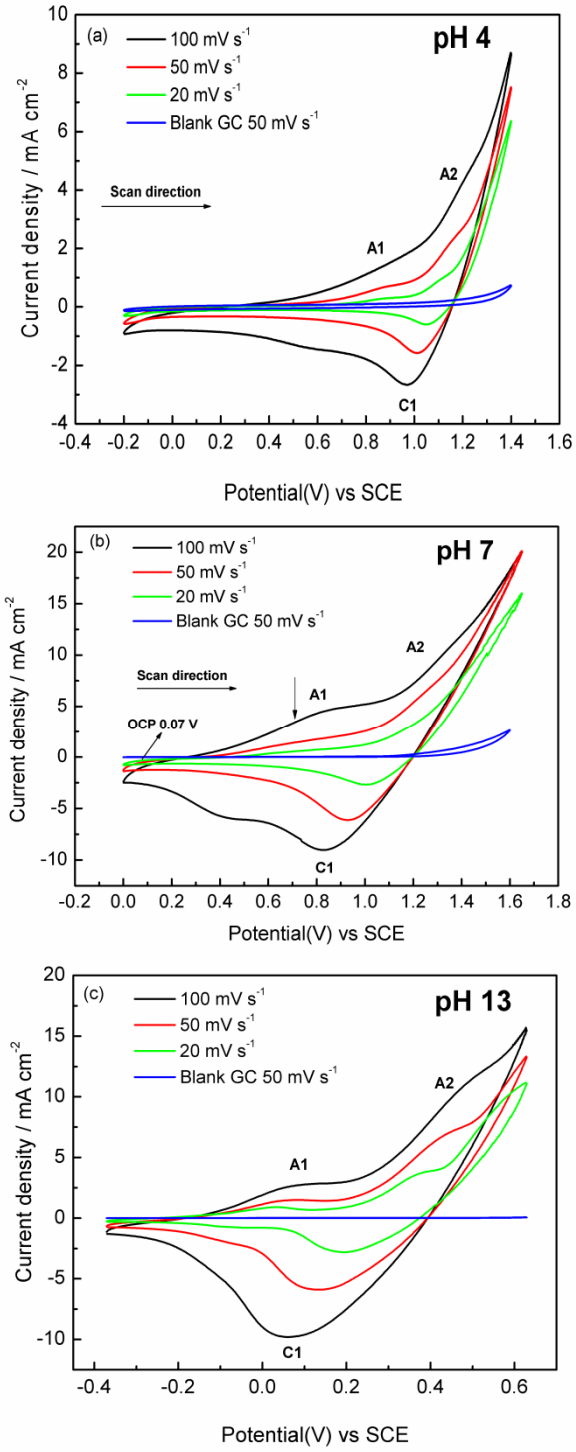

Figure 3.4 Cyclic voltammograms of Co_3O_4 nanorods coated on a glassy carbon electrode (GC) (a) at pH 4, (b) at pH 7 and (c) at pH 13, at different scan rates as indicated in the Figure. CV using the blank glassy carbon (GC) electrode is also shown for comparison.

As evident from Figure 3.4, when the scan rate is increased, the redox peaks A1 and A2 shift towards more positive potential whereas the redox peak C1 shifts towards the negative side. The cyclic voltammograms show the onset potential for oxygen evolution at 0.7 V (*vs.* SCE) at pH 7. Usually, metal cations at higher oxidation states are proposed to be active sites for oxygen evolution [30-31]. Trasatti proposed that oxygen evolution can happen only when the electrode potential is larger than the potential at which a metal ion is oxidized to higher oxidation state in the metal oxide [32]. Therefore, the rise in the anodic current peak at 1.143 V (at pH 7) shows that Co^{4+} is presumably the active site which is responsible for oxygen evolution.

3.4.2 Tafel plots

The primary criteria for an efficient electrocatalyst for oxygen evolution is that it should have less overpotential, defined as $\eta = (E_{app} - E_{iR}) - 1.23 - (0.059\ pH)$, where η is the overpotential for water oxidation, E_{app} is the applied potential (*vs.* NHE), and E_{iR} is the potential drop due to uncompensated resistance [3]. The electrocatalytic activity of material for oxygen evolution can be assessed more reliably by the galvanostatic Tafel polarization technique (section 2.4.3, Chapter 2). The overpotential (η) *vs.* log (current density (j)) curves (Figure 3.5) shows a straight line with a Tafel slope, after manual correction for uncompensated resistance. The experiment has been carried out at different pH values ranging from 4 to 13 (Figure 3.5(a)) facilitating the variation in the kinetics for oxygen evolution. The overpotential at 1 mA cm^{-2}, exchange current density (*x*-axis intercept of the Tafel line at the low-current densityregion) and Tafel slope is given in Table 3.1 for a reliable comparison. From the overpotential values, it is clear that the porous Co_3O_4 nanorods have good activity in the neutral medium with an overpotential as low as of 385 mV, which is important for energy efficient environmentally benign water splitting in photoelectrochemical cells. The exchange current density value of $4.7 \times 10^{-9} Acm^{-2}$ reflects good catalytic activity. Similarly, at pH 4, the values of overpotential and exchange current density are 389 mV and $6.5 \times 10^{-7} Acm^{-2}$, respectively. Interestingly, the catalyst shows higher exchange current density, along with a lower overpotential, as compared to that reported for the cobalt based oxygen evolution catalyst (denoted as Co-Pi) by Nocera and co-workers (η=410 mV, j_0 ~4–6 $\times 10^{-11}$A cm^{-2}, at pH 7) [3, 33]. Higher exchange current density implies high catalytic activity.

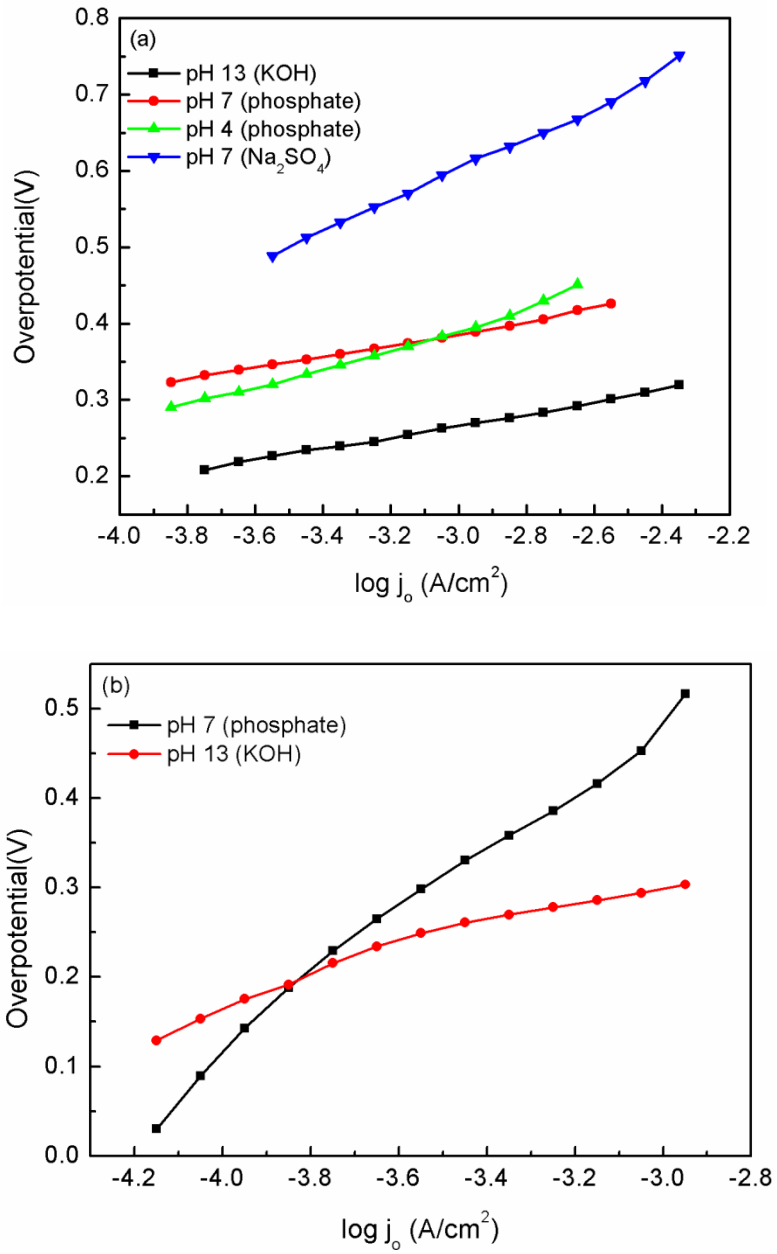

Figure 3.5 Galvanostatic iR corrected Tafel plots of (a) Co_3O_4 nanorods at different pH values, as indicated, and (b) 20% Pt/C at different pH values, as indicated.

Co_3O_4 is a well-known oxygen evolution catalyst in the alkaline medium [34]. However, lowering the pH causes reduction in the hydroxide ion concentration, thereby the activity also decreases. Moreover, Co_3O_4 is not stable in weakly alkaline, neutral and acidic medium under water oxidation condition as per the potential-pH diagrams [10]. This is because, when the H^+ ion concentration increases, the H^+ ions accumulate on the surface and thereby destabilizes the hydrated structure [34]. The Tafel plot of Co_3O_4 nanorods in 0.1 M Na_2SO_4 (pH 7) (Figure 3.5(a)) gives higher overpotential and higher Tafel slope (η =606 mV

at 1 mA cm^{-2}, Tafel slope of 200 mV, Table 1) which shows the instability in neutral medium. Using phosphate buffer as electrolyte solution greatly solves the problem of diffusing the protons from the Co_3O_4 surface by effectively driving away the protons from the Co_3O_4 surface to the bulk of the solution and decreases the overpotential and Tafel slope.

Table 3.1 Overpotential and exchange current density parameters from Tafel plots

Catalyst	**Electrolyte**	**pH**	**Overpotential (η) at 1 mA cm^{-2} (mV)**	**Exchange current density (A cm^{-2})**	**Tafel slope (mV)**
Co_3O_4 nanorods	0.1M KH_2PO_4	4	389	6.5×10^{-7}	120
Co_3O_4 nanorods	0.1M (KH_2PO_4 + K_2HPO_4)	7	385	4.7×10^{-9}	70
Co_3O_4 nanorods	0.1M KOH	13	266	3.1×10^{-7}	76
Co_3O_4 nanorods	0.1 M Na_2SO_4	7	606	1.0×10^{-6}	200
20 % Pt/C	0.1M (KH_2PO_4 + K_2HPO_4)	7	486	3.0×10^{-5}	332
20 % Pt/C	0.1 M KOH	13	300	3.9×10^{-7}	88

In terms of exchange current density and overpotential values, the present material has a higher activity than that of the catalysts Co-B_i (η = 450 mV at 1 mA cm^{-2}, $j_o = 2.1 \times 10^{-12}$ A cm^{-2}) and Ni-B_i (η = 415 mV at 1 mA cm^{-2}, $j_o = 5.8 \times 10^{-18}$ A cm^{-2}) at pH 9.2, reported in the literature [35]. The electrocatalytic activity has also been studied in 0.1 M KOH (pH 13). It shows a very less overpotential of 266 mV with an exchange current density of 3.1×10^{-7}A cm^{-2}. When compared to Co_3O_4/graphene composite [36], the present Co_3O_4 nanorods show 174 mV less overpotential under similar conditions. The activity of Co_3O_4 nanorods is compared with that of 20% Pt/C under identical conditions (Figure 3.5(b)), and it is found that Co_3O_4 nanorods show 100 mV less overpotential at pH 7 and ~40 mV less overpotential at pH 13 than that for 20% Pt/C (Table1). All these results convincingly prove that Co_3O_4 nanorods can be an efficient and cost-effective non-noble metal oxide catalyst for the sluggish oxygen evolution reaction.

Table 3.2 Comparison of electrocatalytic activity of Co_3O_4 nanorods with the reported literature

Catalyst	pH	Overpotential at 1 mA/cm^2 (mV)	Exchange current density (A/cm^2)	References
Co-Bi	9	450	2.1×10^{-12}	[35]
Ni-Bi	9	415	5.8×10^{-18}	[35]
Co_3O_4 nanorods	7	385	4.7×10^{-9}	Present work
Co_3O_4/graphene composite	13	440	-	[36]
Co_3O_4 nanorods	13	266	3.1×10^{-7}	Present work

3.2.7 Impedance analysis

To have some insights into the mechanism of oxygen evolution, impedance analysis has been carried out. All the impedance measurements were done over the frequency range of 1 Hz – 1 MHz, with 10 mV amplitude. All the impedance data were fitted with the equivalent circuits and extracted the parameters by using ZView 3.4 software [37]. Figure 3.6 shows the Nyquist plot of Co_3O_4 nanorods in 0.1 M phosphate buffer (pH 7) under open circuit potential (OCP) condition. The plot consists of a semicircle in the high-frequency region followed by a linear part in the low-frequency region. The semicircular part can be ascribed to the charge transfer processes in the system, while the linear portion gives information about the diffusion of the electrolyte from bulk into the electrode surface as has been reported previously [38]. However, the impedance analysis of the same system with applied bias provides more information with respect to oxygen evolution. Accordingly, Figure 3.7 (a,b) shows the Nyquist plots of Co_3O_4 nanorods in 0.1 M phosphate buffer (pH 7) at different applied potentials on SCE. The nature of the plot changes dramatically with applied potential than that observed at OCP. For example, the linear portion gradually changes to another semicircle at 1 V. Interestingly, the diameter of the second semicircle (at low-frequency region) decreases with increasing potential and the corresponding resistance is very less (11.2 Ω cm^2) at 1.6 V.

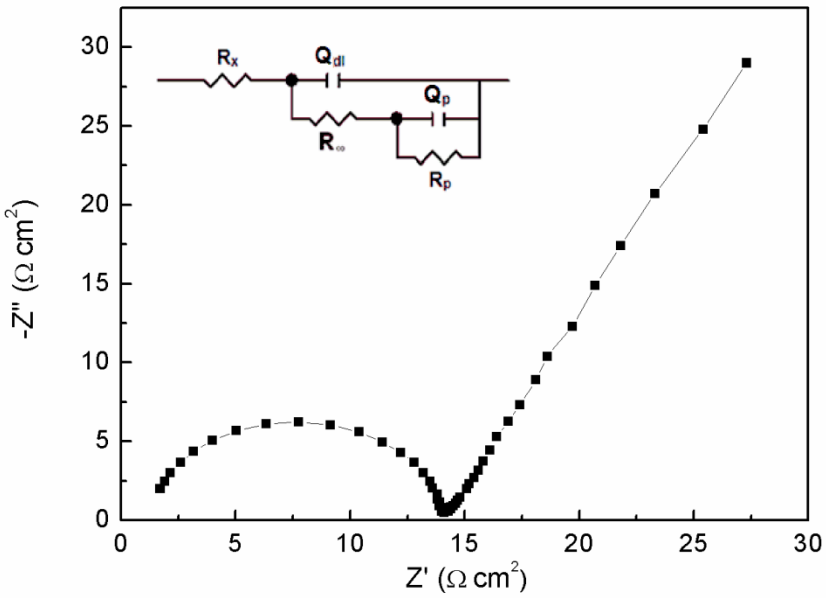

Figure 3.6 Nyquist plots of Co_3O_4 nanorods in 0.1 M phosphate buffer (pH 7) at OCP condition. The inset shows the equivalent circuit used for the data analysis.

The equivalent circuit shown in the inset of Figure 3.6 is used to fit the impedance plots obtained at different applied potentials. In this equivalent circuit, R_x refers to the solution resistance, Q_{dl} refers to the double layer capacitance, R_∞ refers to the charge transfer resistance, R_p, and Q_p refers to the resistance and capacitance associated with adsorption of reaction intermediates, respectively. The same equivalent circuit for the Faradaic reaction, OER, has been suggested in many reports [30, 39-42]. The two semicircles showed in Figure 3.7(b) are somewhat flattened, and therefore, the capacitance in the equivalent circuit can be best described by a constant phase element instead of a true capacitance, as reported in the literature [38]. The constant phase element (CPE) is defined as:

$$Z_{CPE} = \frac{1}{Q(j\omega)^n}$$

where, Q represents the frequency independent parameter and *n* represents the deviation from the ideal behavior of the capacitance. In fact, the equivalent circuit with CPE is found to give a good fit to the experimental data, and it has been shown that, in the case of solid electrodes, this is due the increased roughness and in homogeneity of the surface active sites [38, 43].

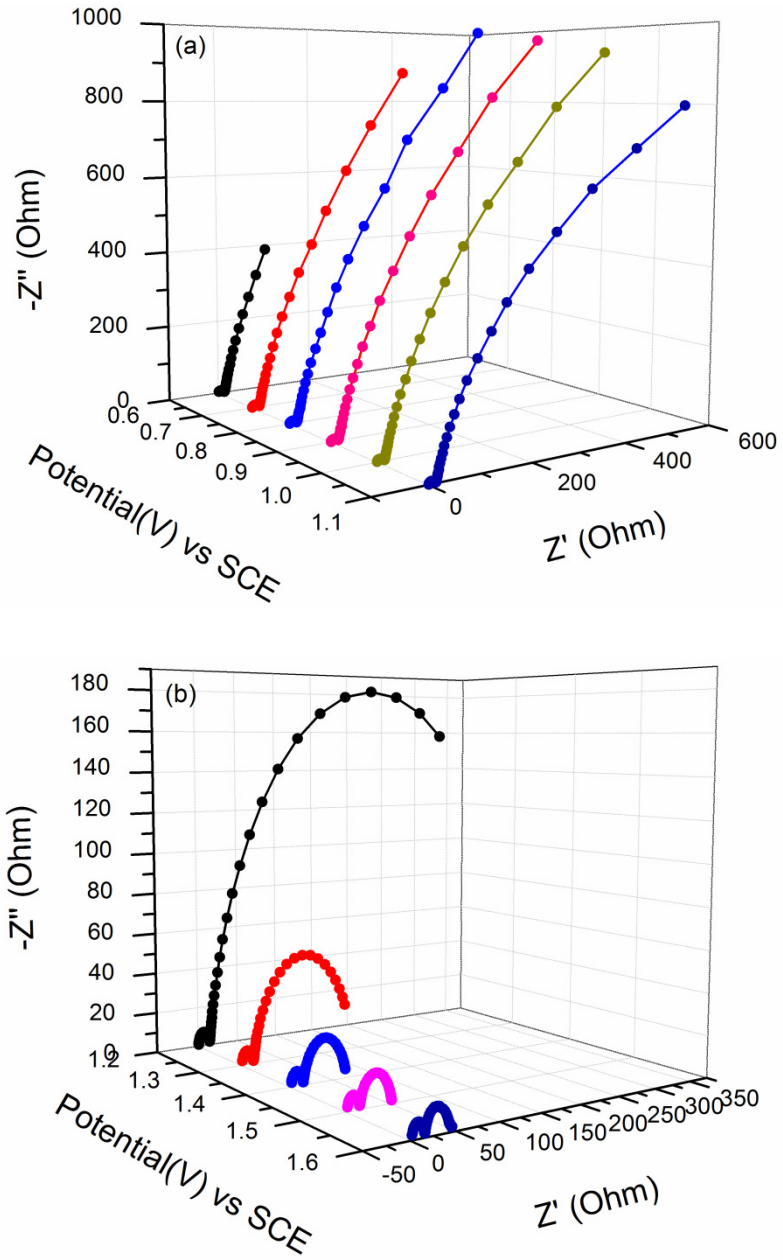

Figure 3.7 (a, b) Nyquist plots of Co_3O_4 nanorods in 0.1 M Phosphate buffer (pH 7) at different applied potentials (a,b)

Figure 3.7(a,b) shows that the high-frequency semicircle is not affected by the applied potential and therefore, it is arising from the resistive/capacitive behavior of the electrical double layer. The diameter of the low-frequency semicircle is reduced with the increasing applied potential, and this can be assigned to the capacitive/resistive behavior associated with the adsorption of the reaction intermediates formed during the charge transfer process. Higher potential facilitates charge transfer across the Co_3O_4–electrolyte interface and hence the diameter of the low-frequency semicircle is reduced at higher potentials. The Faradaic reaction, in this case, can be describedin terms of theequivalent circuit shown in the inset of

Figure 3.6. The validity of the equivalent circuit has been tested by Kramers-Kronig transformation [44], which gives again a good fit (Figure 3.8). The values of the different equivalent circuit elements at different applied potential are shown in Table 3.3.

Table 3.3 Values of the fitting parameters evaluated from equivalent circuit shown in Figure 3.6 at the different applied potentials.

Applied Potential (V)	χ^2	R_x (Ωcm^2)	Q_{dl} ($S\ s^n\ cm^{-2}$)	n_1	R_∞ (Ωcm^2)	Q_p ($S\ s^n\ cm^{-2}$)	n_2	R_p (Ωcm^2)
0.6	5.79×10^{-4}	0.97	4.14×10^{-7}	0.97	12.13	0.000482	0.89	6665
0.7	6.35×10^{-4}	1.05	4.18×10^{-7}	0.97	12.16	0.000540	0.89	3603
0.8	6.42×10^{-4}	1.04	4.21×10^{-7}	0.97	12.17	0.000555	0.88	2061
0.9	6.97×10^{-4}	0.93	4.23×10^{-7}	0.97	12.18	0.000585	0.88	1011
1.0	7.08×10^{-4}	0.87	4.24×10^{-7}	0.97	12.21	0.000675	0.87	196.3
1.1	6.12×10^{-4}	0.93	3.62×10^{-7}	0.98	12.00	0.000916	0.81	53.96
1.2	2.90×10^{-4}	1.04	3.44×10^{-7}	0.98	12.06	0.001114	0.77	34.12
1.3	1.97×10^{-4}	1.24	3.29×10^{-7}	0.98	12.29	0.001705	0.72	25.83
1.4	1.81×10^{-4}	1.33	3.31×10^{-7}	0.98	12.80	0.002028	0.74	17.78
1.5	1.16×10^{-4}	1.37	2.90×10^{-7}	0.99	13.16	0.001895	0.72	13.19
1.6	1.03×10^{-4}	1.34	2.80×10^{-7}	0.99	13.65	0.000948	0.77	11.24

Figure 3.9 shows the plot of resistance (R_p) and capacitance (Q_p) associated with the Faradaic reaction at different potentials. The figure shows that, as the potential increases, the capacitance also increases up to the potential 1.4 V. After this potential, the capacitance (Q_p) suddenly decreases at 1.5 V. The decreasing trend continues beyond 1.5 V. The variation of the resistance (R_p) with applied potential is also in line with this behavior. This kind of behavior is due to the surface redox transitions in the oxidation of Co^{3+} to Co^{4+}, as

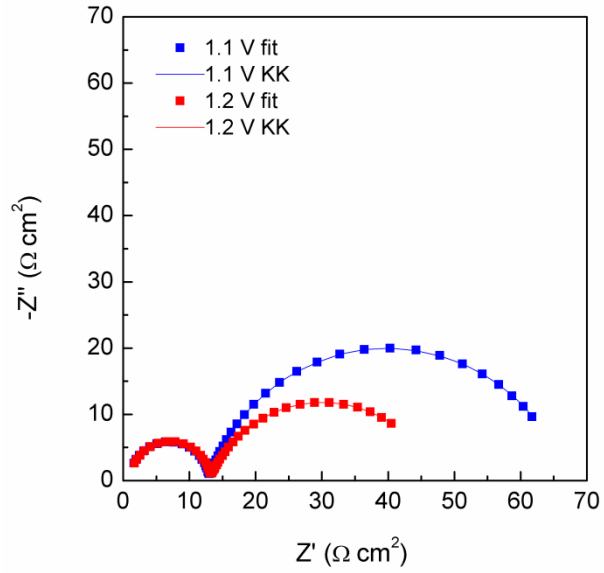

Figure 3.8 Impedance fitting at 1.1 V, 1.2 V (symbols) and the corresponding Kramers-Kronig transformations (lines)

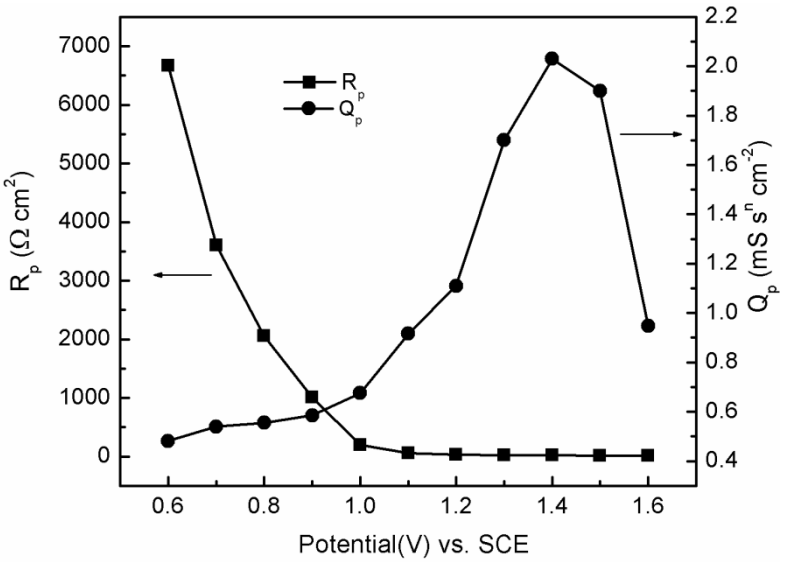

Figure 3.9 Variation of R_p and Q_p with the potential

reported in the literature for Co_3O_4 in the basic medium [39, 45]. This can be correlated to the redox peak (A2) in the cyclic voltammogram (Figure 3.2). In fact, beyond 1.4 V, the potential surpasses the capacitive charging, and so the applied potential is mostly used for bringing down the activation energy for oxygen evolution and hence the improved kinetics is observed at this point.

3.2.8 Turnover Frequency (TOF)

The activity of a catalyst can be expressedin terms ofturn over frequency (TOF). TOF is defined as the number of reactant molecules getting converted into product molecules in unit time per active site. In the present case, it is calculated as the number of O_2 molecules formed per active site at a current density of 1 mA cm^{-2} (overpotential of 385 mV at pH = 7). The TOF is measured using the procedure given in the literature [46]. To calculate the number of active sites per electrochemically accessible surface area (EASA), the roughness factor of the catalyst is determined.

Roughness factor is determined from the experimental value of the double layer capacitance [47]. As per this method, cyclic voltammetry curves were recorded at different scan rates in the non-Faradaic region (0 to 0.2 V) using 0.1 M phosphate buffer solution as the electrolyte with an assumption that double layer charging is the only process in the potential range (Figure 3.10(a)). The slope of the straight line part of the capacitive current *vs.* scan rate gives the double layer capacitance. This method assumes that the capacitance of the smooth surface of an oxide is 60 μF irrespective of the nature of the oxide [47]. From Figure 10(b), the slope of the straight line is obtained as 3470 μF, and the roughness factor is calculated as 57.8. A 3 mm diameter glassy carbon electrode is used as the substrate. From this, EASA is calculated as 4.08 cm^2 using the following equation.

$$\text{EASA} = \text{Roughness factor} \times \text{geometrical area}$$

From the EASA value, the number of the surface Co atoms is calculated. Thisis calculated by assuming that the (110) plane is exposed. The value is obtained as 9.01×10^{14} cobalt atoms/cm^2. Then, TOF is calculated as:

$$TOF = \frac{Currentdensity \times N_A}{4F \times Roughness\ factor \times surface\ cobalt\ atoms\ per\ cm^2}$$

The calculated TOF for the present Co_3O_4 nanorods is obtained as 0.424 $s^{-1}$when considering that only surface Co atoms are active, whereas the value is obtained as 2.94×10^3 s^{-1} when considering that all the Co atoms are active. The lower limit of TOF for oxygen evolution for the present Co_3O_4 nanorods is calculated as 4.15×10^{-3} s^{-1} at the overpotential

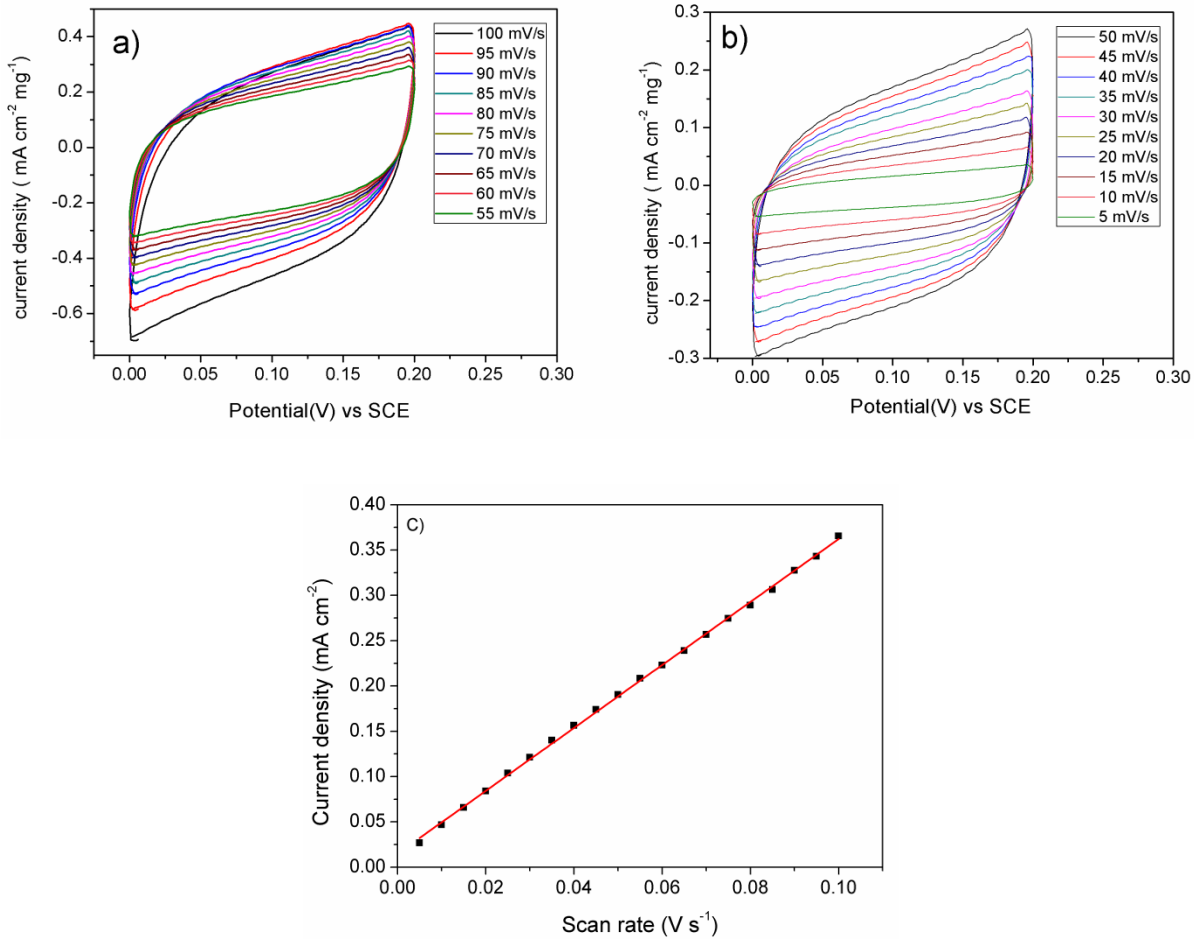

Figure 3.10(a,b) Cyclic voltammetry of Co_3O_4 nanorods at different scan rates in 0.1 M phosphate buffer (pH 7) in the non-Faradaic potential region (0–0.2 V) (for clarity, in between scan rates are not shown) **(c)** Capacitive current density as a function of scan rate from (a,b).

of 410 mV which is larger than the TOF reported for the Co-Pi catalyst (~2×10^{-3} s^{-1} at 410 mV overpotential) [48]. Similarly, the present value is also larger than that reported (8×10^{-4} s^{-1}) for Co_3O_4 nanorods, prepared in mesoporous silica as a template, under photochemical conditions [48].The enhanced catalytic activity of the present Co_3O_4 nanorods towards the oxygen evolution reaction may be attributed to the combination of several factors including the high porosity, higher surface area, enrichment of Co^{3+} ions on the surface of the nanorods apart from the (110) orientation of the rods.

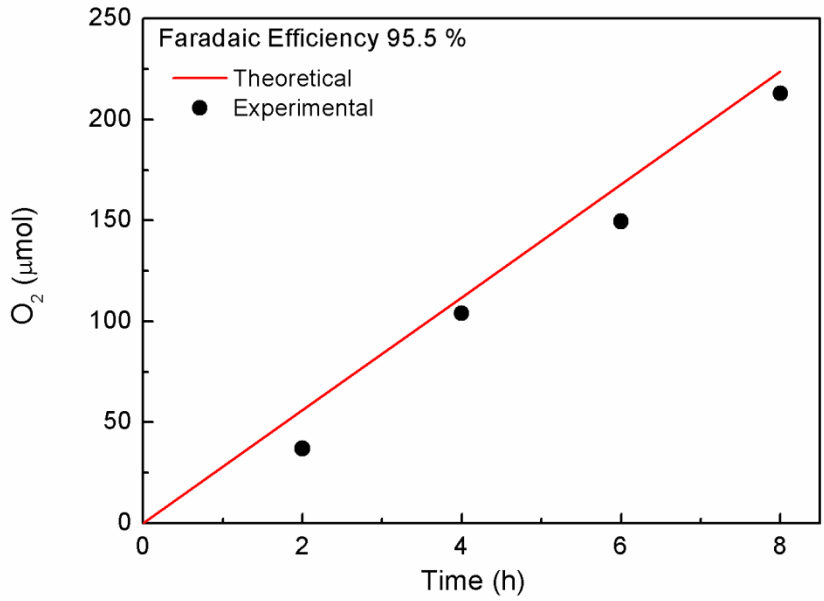

Figure 3.11 Quantitative evolution of oxygen as a function of time of electrolysis. Electrolysis is performed at 1 mA cm^{-2} in 0.1 M pH 7 phosphate buffer solution at room temperature

3.2.9 Quantitative oxygen evolution

The electrocatalytic oxygen evolution has been performed at 1 mA $cm^{-2}$to quantify the rate of oxygen evolution as well as to calculate the Faradaic efficiency of the catalyst (Figure 3.11). Stainless steel (SS316) mesh with the area of 3 cm^2 has been used as an electrode with the catalyst loadings of 1 mg cm^{-2}. The electrolytic reaction has been carried out for 8 hours, and the gas mixture was taken out from the cell at equal intervals and injected into the gas chromatograph (more details on section 2.4.4, chapter 2). Here, the quantity of the collected oxygen gas (n_{O2}) is directly measured with respect to time. According to the Faraday's second law of electrolysis, the amount of oxygen produced is directly proportional to the amount of charge passed,

$$m = Q / nF$$

where 'm' is the number of moles of oxygen, Q is the total charge passed to the cell, 'n' is the number of electrons transferred in the electrode reaction and F is the Faraday constant. Oxygen evolution is a four electron transfer reaction. Thus, the Faradaic efficiency is calculated as n_{O2} / (Q /4F), and it gives a very high Faradaic efficiency of 95.5 %. The rate of oxygen evolution is calculated as 26.6 µmol h^{-1}.

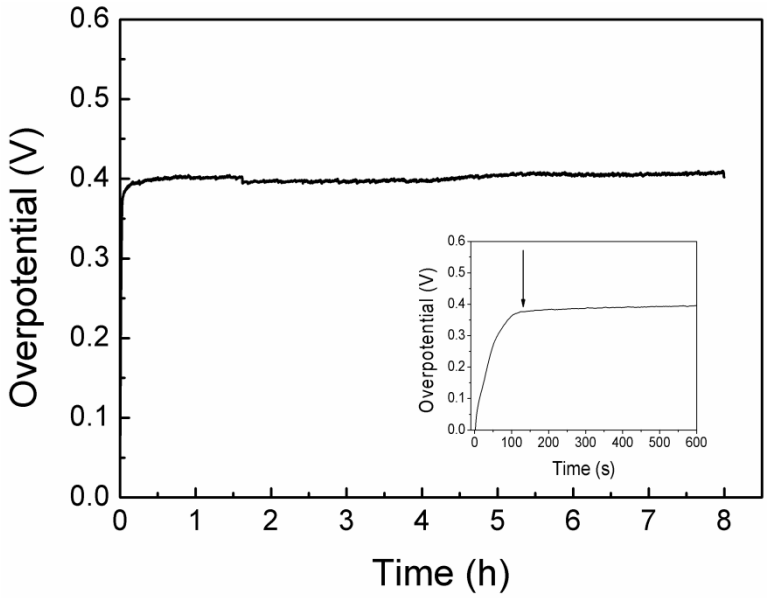

Figure 3.12Stability of Co_3O_4 nanorods at 1 mA cm^{-2} with respect to time at pH 7. The inset shows the enlarged figure showing the onset of oxygen evolution.

3.2.10 Stability measurements

In addition to the high TOF, low onset potential and high Faradaic efficiency sustained stability is also an important parameter for the characterization of an electrocatalyst for oxygen evolution, since oxygen evolution occurs in a highly oxidative environment. Hence, to verify the stability of the catalyst used, electrolysis has been done for 8 hours at pH 7 at a current density of 1 mA cm^{-2}. The glassy carbon electrode is used as the substrate, and the catalyst is loaded as 1 mg cm^{-2}. As shown in Figure 3.12, the overpotential does not change with time, up to 8 hours, showing the prolonged catalytic activity of the catalyst. To study the property of the catalyst after the electrolysis, a large amount of the catalyst (20-25 mg) is coated on the stainless steel plates, and electrolysis has been done at pH 4 and 7 with the applied current of 1 mA per milligram of the catalyst. Figure 3.13(a,b) shows the XRD pattern of the catalyst before and after the electrolysis at pH 4 and pH 7. Since there is no change in the powder XRD patterns of the catalyst before and after the electrolysis (Figure 3.13), it is proved that the material is highly stable under OER condition. The clear electrolyte solution after the electrolysis was tested for cobalt content by ICP analysis. The electrolyte used at pH 7 showed 0.2 ppm (20 mg of catalyst used), and the electrolyte used at pH 4 showed 5.9 ppm (25 mg of catalyst used) of cobalt content after 8 hours of electrolysis. The negligible amounts of cobalt in the electrolyte after electrolysis also confirm the stability

of the catalyst under OER conditions. All these data ostensibly prove that the catalyst is capable of working in a wide pH range of 4–14, for a longer time, without degradation.

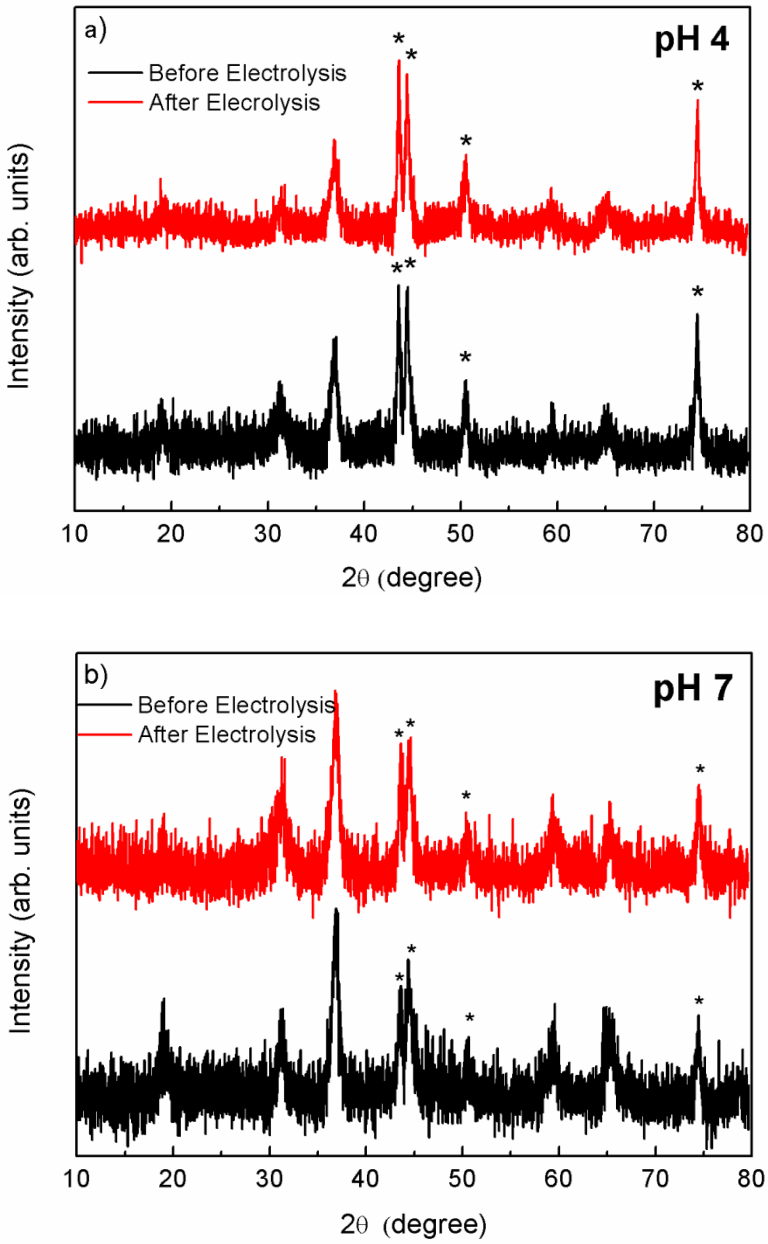

Figure 3.13 Powder XRD patterns of the Co_3O_4 nanorods before and after the electrolysis, for 8 hours, (a) at pH 4 and (b) at pH 7. The peaks indicated with * belongs to the stainless steel (SS316) substrate

Density functional theory studies of water adsorption and oxidation at Co_3O_4 (110) surface [49-50] showed that the surface is energetically favored for the dissociative adsorption of water and the low dissociative barriers indicated that Co_3O_4 (110) surface could be easily hydroxylated. Moreover, for the high surface coverage of water molecules, like in an electrochemical cell, it is predicted that the overpotential will be as low as 390 mV. The present result (overpotential of 385–400 mV) interestingly, matches well with these theoretical predictions. It has been emphasized by Trasatti [32] that metal cations change into their higher oxidation states before the oxygen evolution and those higher-valent cations act as active sites. Accordingly, the cyclic voltammogram of Co_3O_4 nanorods (Figure3.2) showed that oxidation of Co^{3+} to Co^{4+} precedes the oxygen evolution. Hence, it can be assumed that Co^{4+} is presumably the active center for oxygen evolution which originates from Co^{3+} in the course of the electrochemical reaction [51]. Therefore, the higher population of Co^{3+} in the nanorods due to the (110) orientation is probably one of the reasons for the enhanced catalytic activity for oxygen evolution for the present porous nanorods.

3.3 Studies on Co_3O_4 nanoparticles

Electrocatalytic activity of morphology-controlled Co_3O_4 nanorods prepared by co-precipitation-digestion under optimized synthesis condition was described in the previous section. The catalytic activity of the as-prepared Co_3O_4 nanorods was tested under a wide range of pH including the neutral pH, which is known to be a harsh condition since $Co_3O_4$is not stable thermodynamically under neutral pH condition at the applied potentials [53]. As discussed in the previous section, very less overpotential and high exchange current density resulted for the Co_3O_4 nanorods at neutral pH. It could be correlated with the characteristic features of the material such as high surface area, porous nature and dominant exposure of (110) plane which is known to be surface exposed and responsible for the high catalytic activity. However, the obtained results regarding the overpotential when compared to materials with comparable features, reported in the literature, suggests the possibility of other structural aspects such as the distribution of cations in the two different coordination environments in the spinel structure, with different oxidation states and spin state, etc. To unearth the above-mentioned fact, Co_3O_4 with a different morphology (nanoparticles) and physical properties (surface area and porosity) was prepared via an autocombustion method and studied for its electrocatalytic activity for oxygen evolution reaction under alkaline condition.

3.3.1 Synthesis

Co_3O_4 nanoparticles were synthesized by an autocombustion method. More detailed information on the synthetic methodology can be found in Chapter-2. Cobalt nitrate ($Co(NO_3)_2.6H_2O$) and glycine were taken in the mole ratio of 1:0.45 and dissolved in minimum amount of distilled water and stirred vigorously to obtain a uniform solution. The mixed solution was evaporated slowly at 200 ºC, on a hot plate, to initiate the autocombustion reaction in a controlled manner. After the evaporation of water, the resulting thick mass burnt spontaneously to obtain a fluffy powder mass of cobalt oxide.

3.3.2 X-ray diffraction

The XRD pattern of the as-synthesized Co_3O_4 powder is shown in Figure 3.14. The position and intensities of all the peaks are well matched with the reference pattern (JCPDS # 09-0418) of Co_3O_4 and confirm the formation of cubic spinel phase. All the peaks in the experimental patterns are somewhat broad indicating nanocrystalline nature of the sample. The average crystallite size calculated from the full width at half maximum (FWHM) of the major peak (311) using the Scherrer formula is 7 nm.

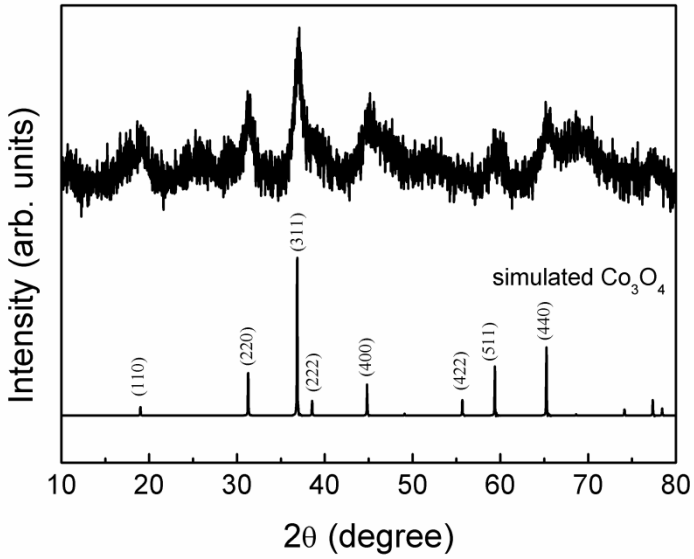

Figure 3.44 Powder XRD patterns of the Co_3O_4 nanoparticles compared with the simulated pattern

3.3.3TEM studies

Figure 3.15 reveals that the morphology of Co_3O_4 synthesized by the autocombustion method. The image shows flaky-type particles forming clusters. Similar morphological

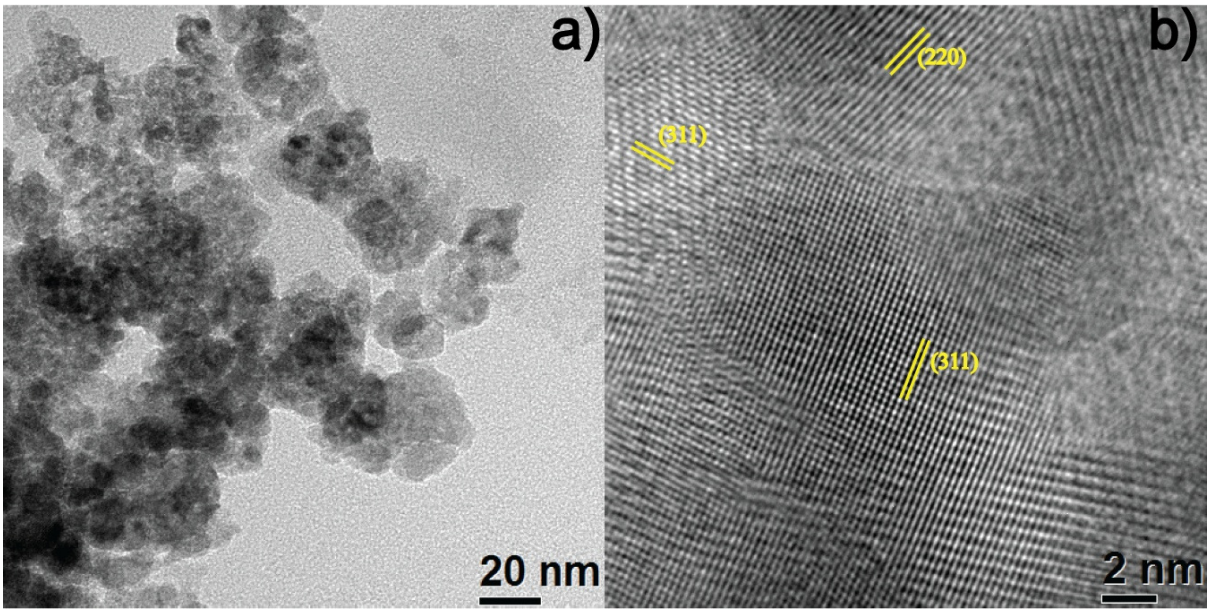

Figure 3.15 TEM images of Co_3O_4 nanoparticles (a) and the corresponding lattice spacing (b)

features have been reported for different types of oxides synthesized by the glycine-nitrate Combustion process [54]. Since the combustion reaction is very rapid, it is very difficult to control the morphology in the case of the auto-combustion method resulting in a cluster of small sized particles. All the particles are spherical in nature and aggregated. Figure 3.15(b) shows some of the lattice fringes with the d-spacing 2.5 Å and 2.9 Å matching well with the d-spacing of (311)and (220) planes respectively.

3.3.4 Surface area

Brunauer-Emmett-Teller (BET) surface area measurement in Figure 3.16 shows the hysteresis loop of nitrogen adsorption-desorption isotherm. The surface area is found to be 70 m^2/g.

3.3.5 X-ray photoelectron spectroscopy

To get detailed information about the environment of the cations in the structure, both Co_3O_4 nanorods and nanoparticles were subjected to X-ray photoelectron spectroscopy (XPS) analysis. In the case of Co_3O_4 spinel, the presence of both 2+ and 3+ ions can be confirmed by XPS studies. In principle, any change in the oxidation state reflects in XPS binding energy change due to chemical effects. For the spinel type cobalt, it is well reported that the energy separation between Co $2p_{3/2}$ and Co $2p_{1/2}$ is approximately 15.1 eV [52]. The XPS spectra of

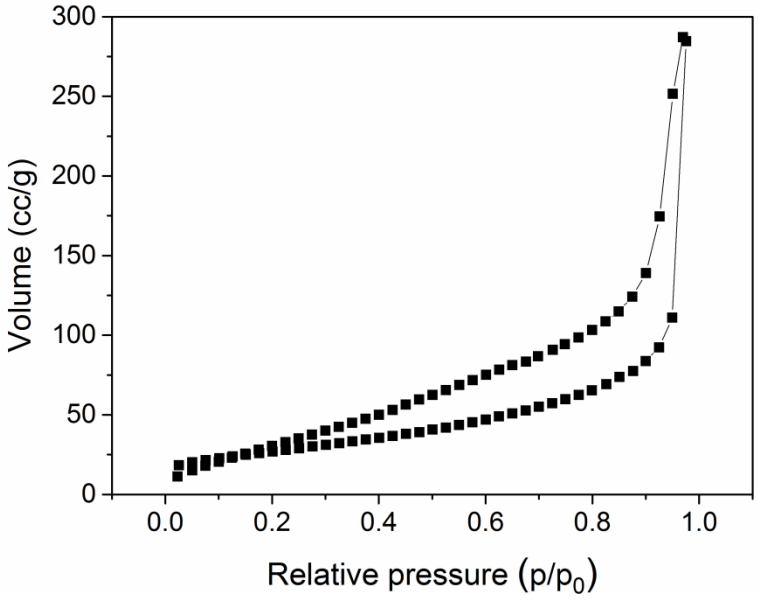

Figure 3.16 Nitrogen adsorption-desorption curve of the Co_3O_4 nanoparticles

both the Co_3O_4 nanorods and nanoparticles are shown in Figure 3.17. It clearly shows two major peaks with binding energy values of 780.3 eV and 795.4 eV, corresponding to Co $2p_{3/2}$ and $2p_{1/2}$ core levels, respectively, of the Co_3O_4 phase. Lack of prominent shake-up satellite peaks in the Co 2p spectra further suggests the presence of mainly Co_3O_4 phase [53]. For cobalt compounds with 2+ valence state (paramagnetic), a strong satellite peak is expected around 6 eV above the Co $2p_{3/2}$ [54]. Hence, the mixed valence Co_3O_4 with a contribution

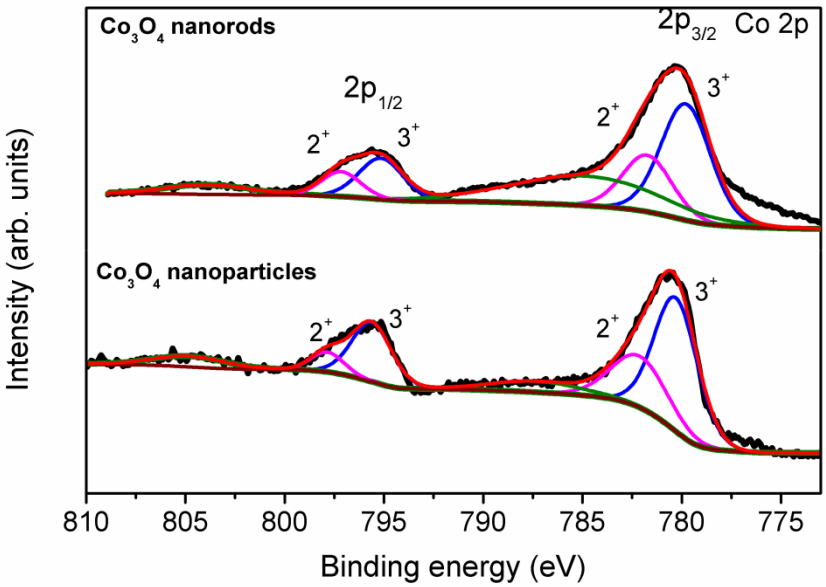

Figure 3.17 XPS spectra Co_3O_4 nanoparticles and Co_3O_4 nanorods

from Co^{2+}, together with Co^{3+} which does not show any satellite peaks, resulted in a weak satellite that confirms the minor component of Co^{2+}. From the characteristic features of XPS of Co_3O_4 nanorods and nanoparticles, the formation of Co_3O_4 can be confirmed. Also, the fitting of the XPS spectrum clearly indicates the almost similar ratio of Co^{2+} and Co^{3+} for Co_3O_4 nanorods and nanoparticles.

3.5.4 Electrocatalytic studies of cobalt oxide nanoparticles

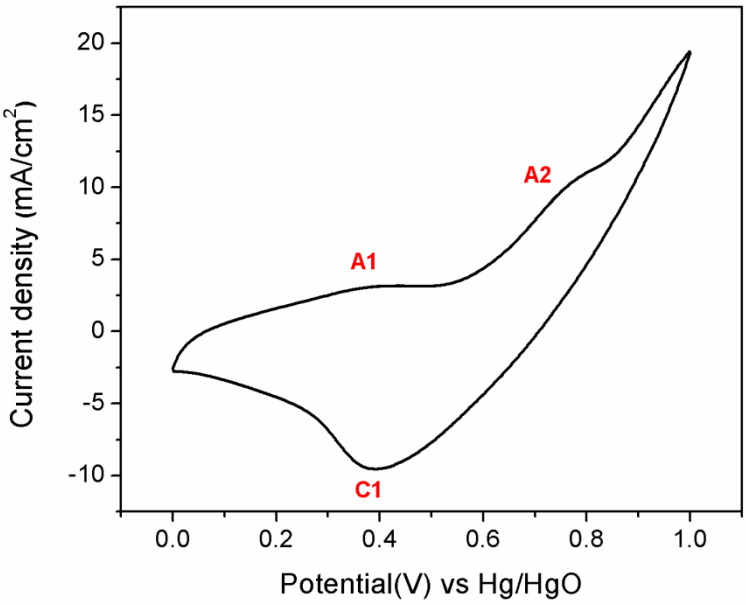

Figure 3.18 Cyclic voltammetry curve of Co_3O_4 nanoparticles in 0.1 M KOH at the scan rate of 50 mV/s

Figure 3.18 shows the cyclic voltammogram of Co_3O_4 nanoparticles in 0.1 M KOH at the scan rate of 50 mV/s, and it is almost similar to the cyclic voltammogram Co_3O_4 nanorods (Figure 3.4(c)). It shows the characteristic redox behavior of cobalt oxide. The voltammogram exhibit two anodic peaks (Al, A2) corresponding to oxidation of Co^{2+} to Co^{3+}, and Co^{3+} to Co^{4+}, respectively. And the observed cathodic peak (C1) is due to the reduction of Co^{4+} to Co^{3+}. The electrocatalytic comparison of Co_3O_4nanoparticles and Co_3O_4 nanorods has been done at pH 13 by using 0.1 M KOH solution as an electrolyte. Since KOH solution has higher conductivity than the phosphate electrolyte, the electrocatalytic comparison is more effective in KOH electrolyte.

To have a better understanding of the electrocatalytic behavior of Co_3O_4 nanorods and nanoparticles at pH 13, their Tafel plots are compared and shown in Figure 3.18. Both the

Tafel plots show similar behavior in the low current density region and slightly deviated in the higher current density region. Table 3.4 shows the kinetic parameters extracted from the Tafel plots like overpotential, Tafel slope and exchange current density.

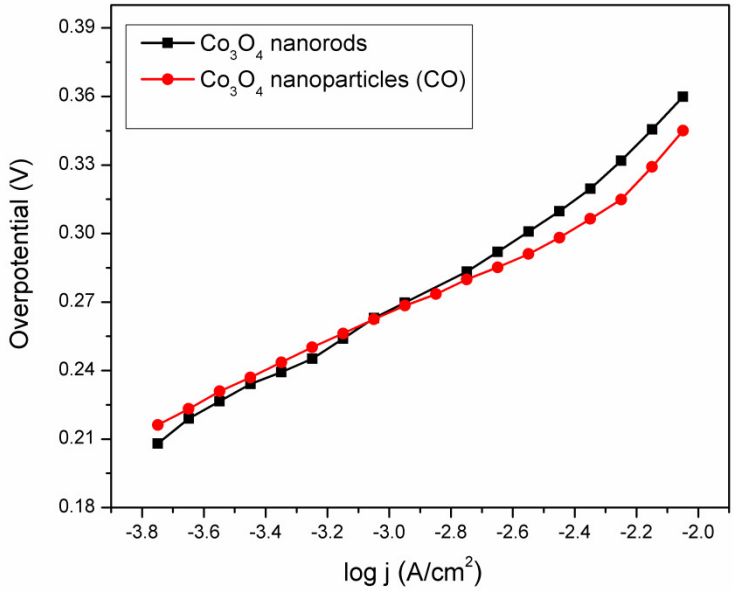

Figure 3.18 Galvanostatic iR corrected Tafel plots of Co_3O_4 nanorods and Co_3O_4 nanoparticles.

Table 3.4 Overpotential and exchange current density parameters from Tafel plots

Catalyst	η at 1 mA/cm^2 (mV)	η at 5 mA/cm^2 (mV)	Tafel slope (mV)	Exchange current density (A/cm^2)	BET surface area (m^2/g)
Co_3O_4 nanorods	266	326	76	3.1×10^{-7}	100
Co_3O_4 nanoparticles	266	311	62	5.2×10^{-8}	70

3.3.7 Magnetic susceptibility

The inset of Figure 3.19 shows the temperature-dependant DC magnetization curves of Co_3O_4 nanorods and Co_3O_4 nanoparticles and behavior of the curves show that both are paramagnetic in nature. For further analysis, the DC magnetization curves are converted into $1/\chi$ vs. T. Figure 3.19 shows the $1/\chi$ vs. T plots and above 100 K both the nanoparticles and nanorods show a straight-line behaviour and follows the Curie-Weiss law, $\chi = C/(T-\theta)$, where C is the Curie constant and θ is the Weiss temperature.From the fit to the straight lines above 100 K, C (1/slope) is obtained as 2.80 emu K mol^{-1} and 2.87 emu K mol^{-1}for the Co_3O_4

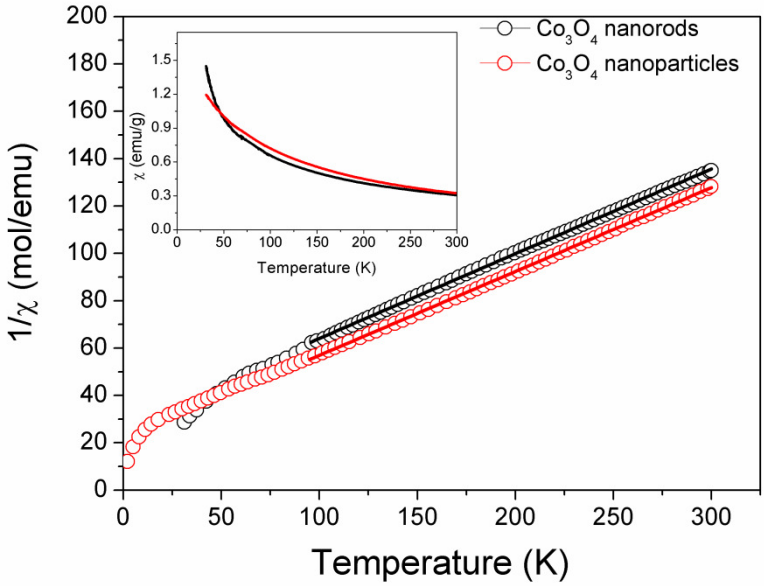

Figure 3.19 Temperature dependence of the inverse susceptibility of Co_3O_4 nanorods and Co_3O_4 nanoparticles, (inset) DC magnetization curves of Co_3O_4 nanorods and Co_3O_4 nanoparticles

nanorods and nanoparticles, respectively. (Section 2.3.5, chapter 2) The Curie constant C is given by [55]:

$$C = Ng^2\mu_B{}^2 S (S+1)/3k$$

where N is the Avogadro number, g is g-factor (= 2), k is the Boltzmann constant and $\mu_B$is Bohr magneton, the unit for the magnetic moment of an electron.

Table 3.5 Curie constant and spin values of Co_3O_4 from magnetic measurements

Sample code	Curie constant (emu K mol^{-1})	Total spin (S)	Spin contribution from Co^{3+}
Co_3O_4 nanorods	2.80	1.92	0.42
Co_3O_4 nanoparticles	2.87	1.94	0.45

Usually, in the bulk Co_3O_4, $Co^{2+}$is in the high-spin configuration (d^7, $t_{2g}{}^5e_g{}^2$, S = 3/2) and Co^{3+} prefers the low-spin configuration (d^6, $t_{2g}{}^6e_g{}^0$, S = 0). Therefore, the paramagnetic moment is contributedby the three unpaired electrons from Co^{2+}. However, the calculated total spin values are larger than the expected spin value of 1.5, as shown in Table 3.5. Thus, the obtained higher spin values could be due to the additional paramagnetic contribution from Co^{3+}. The spin contribution from Co^{3+} is calculated by subtracting the contribution from Co^{2+}

(S=1.5) and shown in Table 3.5. The spin contribution from Co^{3+} is almost equal to the contribution from one electron (S = 0.5), suggesting that one of the Co^{3+}, is likely to be present in the intermediate ($t_{2g}^5e_g^1$) or high-spin ($t_{2g}^4e_g^2$) configuration. Thus, the enhanced electrocatalytic activities of Co_3O_4 nanorods and nanoparticles compared to the other Co_3O_4 nanostructures with the similar surface area, reported in the literature, could be due to the unpaired electrons in part of the Co^{3+} present. Inspired from the possible contribution of spin states in the electrocatalytic activities, more detailed studies are carried out by controlling/restricting the population of Co^{3+} and Co^{2+} by suitable substitution in Co_3O_4. These results are discussed in the subsequent chapters.

3.4 Comparison of the activities of nanorods and nanoparticles

Comparison of the electrocatalytic activities of nanorods and nanoparticles of Co_3O_4, synthesized by two different methods, showed that both gave same overpotential value (266 mV) at 1 mA/cm^2 whereas the nanoparticles showed relatively low overpotential (311 mV) than for the nanorods (326 mV) at 5 mA/cm^2 (Table 3.4).Thus, even though the surface area of the Co_3O_4 nanoparticles (70 m^2/g) is lesser than that for the nanorods (100 m^2/g), the nanoparticles show comparatively higher electrocatalytic activity for the OER than by the nanorods. To understand further, overpotential values of the Co_3O_4 nanorods and nanoparticles are compared with the overpotential values of cobalt oxides reported in the literature in Table 3.6.

Table 3.6 Overpotential of Cobalt oxides with a variable surface area for the oxygen evolution reaction, taken from the literature.

Catalyst	Overpotential	BET surface area (m^2/g)	Reference
Co_3O_4 nanowire arrays	375 mV (at 1 mA/cm^2)	74	[56]
Ultrathin Co_3O_4 nanoplates	258 mV (at 1 mA/cm^2)	161	[57]
Co_3O_4 nanoplates	596 mV (at 5 mA/cm^2)	88	[57]
Co_3O_4 nanoplates	535 mV (at 5 mA/cm^2)	107	[57]

For the surface area of 70-90 m^2/g, comparable to that of the nanoparticles in the present work, the observed overpotential values are 375 mV (at 1 mA/cm^2) and 596 mV (at 5 mA/cm^2) for Co_3O_4 nanowire arrays[56] and Co_3O_4 nanoplates[56], respectively. However, in the present work, Co_3O_4 nanoparticles has a similar surface area (70 m^2/g) and the overpotential is 266 mV (at 1 mA/cm^2) and 311 mV (at 5 mA/cm^2), which is lesser than the overpotential values of Co_3O_4 nanowire arrays and Co_3O_4 nanoplates reported in the literature.

For Co_3O_4 nanoplates with asurface area of 107 m^2/g, the overpotential reported is 535 mV (at 5 mA/cm^2), whereas, for Co_3O_4 nanorods with the similar surface area, overpotential is obtained as 326 mV (at 5 mA/cm^2) [57]. Similarly, for ultrathin Co_3O_4 nanoplates with high surface area of 161 m^2/g, overpotential of 258 mV (at 1 mA/cm^2) is achieved, comparable to the overpotential (266 mV, at 1 mA/cm^2) achieved forCo_3O_4 nanorods and Co_3O_4 nanoparticles with the lesser surface area (100 and 70 m^2/g, respectively) in the present work.

The above discussion suggests that higher surface area of the catalyst is not the only parameter to reduce the overpotential for the oxygen evolution reaction. Even with the less surface area, similar or lower overpotential values are observed in Co_3O_4 with different nanostructures. It clearly suggests few other governing factors responsible for electrocatalytic activity for the oxygen evolution in Co_3O_4, in the present case. As shown above, XPS clearly revealed identical cationic environment for Co_3O_4 nanorods and nanoparticles. Further, to get an in-depth information, Co_3O_4 nanorods and Co_3O_4 nanoparticles are subjected to magnetic measurements, which suggested the presence of part of Co^{3+} in the intermediate or high-spin state, which could be the crucial factor for the lower overpotential and enhanced catalytic activity in the present work.

3.5 Conclusions

Co_3O_4 nanorods and nanoparticles are synthesized by a co-precipitation digestion method and autocombustion method, respectively. Both nanostructures showed excellent catalytic activity for oxygen evolution reaction, with relatively less overpotential and high current density, an important reaction for hydrogen generation via water splitting. Even though the superior catalytic performance of the Co_3O_4 nanorods could be correlated well with the dominant exposure of the (110) crystal plane, which is known to catalytically active, with the high surface area and porous nature, the nanoparticles with relatively less surface area also showed similar results pointing to a different contribution. Magnetic susceptibility measurements

suggested the possible contribution from a part of the Co^{3+} ions present, probably on the surface of the nanostructures, in their intermediate or high-spin state. Thus, the present study indicates that the electronic structure of the Co^{3+} ions influences the electrocatalytic response of Co_3O_4 towards oxygen evolution reaction.

References

1. Zheng, Y. R.; Gao, M. R.; Gao, Q.; Li, H. H.; Xu, J.; Wu, Z. Y.; Yu, S. H., *Small* **2015,** *11*, 182.
2. Dincă, M.; Surendranath, Y.; Nocera, D. G., *Proceedings of the National Academy of Sciences* **2010,** *107*, 10337.
3. Kanan, M. W.; Nocera, D. G., *Science* **2008,** *321*, 1072.
4. Ahn, H. S.; Tilley, T. D., *Advanced Functional Materials* **2013,** *23*, 227.
5. Zhao, Q.; Yu, Z.; Yuan, W.; Li, J., *International Journal of Hydrogen Energy* **2012,** *37*, 13249.
6. Pourbaix, M., *Atlas of electrochemical equilibria in aqueous solutions.* Pergamon Press, Oxford **1974**.
7. Trasatti, S., *Electrochimica Acta* **1984,** *29*, 1503.
8. Matsumoto, Y.; Sato, E., *Materials Chemistry and Physics* **1986,** *14*, 397.
9. Lipkowski, J.; Ross, P. N., *The electrochemistry of novel materials*. VCh New York: 1994.
10. Takeno, N. *Atlas of Eh–pH Diagrams. Intercomparison of Thermodynamic Databases.* ; Japan Open File Report: 2005.
11. Sun, Y. F.; Gao, S.; Lei, F. C.; Liu, J. W.; Liang, L.; Xie, Y., *Chemical Science* **2014 ,***5*, 3976.
12. Grzelczak, M.; Zhang, J.; Pfrommer, J.; Hartmann, J.; Driess, M.; Antonietti, M.; Wang, X., *Acs Catalysis* **2013,** *3*, 383.
13. Esswein, A. J.; McMurdo, M. J.; Ross, P. N.; Bell, A. T.; Tilley, T. D., *The Journal of Physical Chemistry C* **2009,** *113*, 15068.
14. Xie, X.; Shen, W., *Nanoscale* **2009,** *1*, 50.
15. Sun, H. Q.; Ang, H. M.; Tade, M. O.; Wang, S. B., *Journal of Materials Chemistry A* **2013,** *1*, 14427.
16. Xie, X.; Li, Y.; Liu, Z. Q.; Haruta, M.; Shen, W., *Nature* **2009,** *458*, 746.
17. Xiao, J.; Kuang, Q.; Yang, S.; Xiao, F.; Wang, S.; Guo, L., *Scientific reports* **2013,** *3*, 2300.
18. Liu, D.; Wang, X.; Wang, X.; Tian, W.; Bando, Y.; Golberg, D., *Scientific reports* **2013,** *3*, 2543.
19. Zhang, M.; de Respinis, M.; Frei, H., *Nature Chemistry* **2014,** *6*, 362.

20. Wang, H.-Y.; Hung, S.-F.; Hsu, Y.-Y.; Zhang, L.; Miao, J.; Chan, T.-S.; Xiong, Q.; Liu, B., *The Journal of Physical Chemistry Letters* **2016,***7*, 4847.
21. Vijayanand, S.; Kannan, R.; Potdar, H. S.; Pillai, V. K.; Joy, P. A., *Journal of Applied Electrochemistry* **2013,** *43*, 995.
22. Patil, D.; Patil, P.; Subramanian, V.; Joy, P. A.; Potdar, H. S., *Talanta* **2010,** *81*, 37.
23. Kshirsagar, V. S.; Vijayanand, S.; Potdar, H. S.; Joy, P. A.; Patil, K. R.; Rode, C. V., *Chemistry Letters* **2008,** *37*, 310.
24. Viswanath, B.; Kundu, P.; Halder, A.; Ravishankar, N., *Journal of Physical Chemistry C* **2009,** *113*, 16866.
25. Sing, K. S.; Gregg, S., *Adsorption, surface area and porosity*. Academic Press, London: **1982**
26. Po, H. N.; Senozan, N. M., *Journal of Chemical Education* **2001,** *78*, 1499.
27. Boggio, R.; Carugati, A.; Trasatti, S., *Journal of Applied Electrochemistry* **1987,** *17*, 828.
28. Švegl, F.; Orel, B.; Grabec-Švegl, I.; Kaučič, V., *Electrochimica Acta* **2000,** *45*, 4359.
29. Švegl, F.; Orel, B.; Hutchins, M.; Kalcher, K., *Journal of the Electrochemical Society* **1996,** *143*, 1532.
30. Lyons, M. E. G.; Brandon, M. P., *International Journal of Electrochemical Science* **2008,** *3*, 1386.
31. Lyons, M. E. G.; Brandon, M. P., *Journal of Electroanalytical Chemistry* **2010,** *641*, 119.
32. Trasatti, S., *Electrochimica Acta* **1991,** *36*, 225.
33. Surendranath, Y. Oxygen evolution mediated by co-based thin film electrocatalysts. Doctoral dissertation, Massachusetts Institute of Technology, 2011.
34. He, J.; Peng, Y.; Sun, Z.; Cheng, W.; Liu, Q.; Feng, Y.; Jiang, Y.; Hu, F.; Pan, Z.; Bian, Q.; Wei, S., *Electrochimica Acta* **2014,** *119*, 64.
35. Surendranath, Y.; Bediako, D. K.; Nocera, D. G., *Proceedings of the National Academy of Sciences of the United States of America* **2012,** *109*, 15617.
36. Suryanto, B. H. R.; Lu, X. Y.; Zhao, C., *Journal of Materials Chemistry A* **2013,** *1*, 12726.
37. Johnson, D., ZPlot, ZView Electrochemical Impedance Software, Version 2.3 b. In *Scribner Associates, Inc*, 2000.
38. Barsoukov, E.; Macdonald, J. R., *B.E.conway, in Impedance spectroscopy: theory, experiment, and applications*. Wiley. com: 2005.

39. Costa, F. R.; Franco, D. V.; Da Silva, L. M., *Electrochimica Acta* **2013,** *90*, 332.
40. Mellsop, S.; Gardiner, A.; Marshall, A., *Electrocatalysis* **2014,** *5*, 445.
41. Palmas, S.; Ferrara, F.; Mascia, M.; Polcaro, A. M.; Ruiz, J. R.; Vacca, A.; Piccaluga, G., *International Journal of Hydrogen Energy* **2009,** *34*, 1647.
42. Wu, X.; Ma, H.; Chen, S.; Xu, Z.; Sui, A., *Journal of the Electrochemical Society* **1999,** *146*, 1847.
43. Choquette, Y.; Brossard, L.; Lasia, A.; Menard, H., *Journal of the Electrochemical Society* **1990,** *137*, 1723.
44. Urquidi-Macdonald, M.; Real, S.; Macdonald, D. D., *Journal of the Electrochemical Society* **1986,** *133*, 2018.
45. Palmas, S.; Ferrara, F.; Vacca, A.; Mascia, M.; Polcaro, A. M., *Electrochimica Acta* **2007,** *53*,400.
46. Yeo, B. S.; Bell, A. T., *Journal of the American Chemical Society* **2011,** *133*, 5587.
47. Trasatti, S.; Petrii, O., *Journal of Electroanalytical Chemistry* **1992,** *327*, 353.
48. Surendranath, Y.; Kanan, M. W.; Nocera, D. G., *Journal of the American Chemical Society* **2010,** *132*, 16501.
49. Xu, X. L.; Li, J. Q., *Surface Science* **2011,** *605*, 1962.
50. Chen, J.; Selloni, A., *Journal of Physical Chemistry Letters* **2012,** *3*, 2808.
51. McAlpin, J.; Surendranath, Y.; Dinca, M.; Stich, T.; Stoian, S.; Casey, W.; Nocera, D.; Britt, R., *Journal of the American Chemical Society* **2010,** *132*, 6882.
52. Tan, B. J.; Klabunde, K. J.; Sherwood, P. M. A., *Journal of the American Chemical Society* **1991,** *113*, 855.
53. Chuang, T. J.; Brundle, C. R.; Rice, D. W., *Surface Science* **1976,** *59*, 413.
54. Langell, M. A.; Anderson, M. D.; Carson, G. A.; Peng, L.; Smith, S., *Physical Review B* **1999,** *59*, 4791.
55. Cullity, B. D.; Graham, C. D., *Introduction to magnetic materials*. John Wiley & Sons: 2011.
56. Li, Y.; Hasin, P.; Wu, Y., *Advanced Materials* **2010,** *22*, 1926.
57. Zhou, X.; Xia, Z.; Tian, Z.; Ma, Y.; Qu, Y., *Journal of Materials Chemistry A* **2015,** *3*, 8107.

Chapter 4

Role of Co^{2+} in Co_3O_4 on the electrochemical oxygen evolution

4.1 Introduction

Spinel Co_3O_4 is identified as one of the potential electrocatalysts for oxygen evolution reaction [1]. The mixed-valent nature of the metal ions in Co_3O_4 (Co^{3+} in the octahedral sites and Co^{2+} in the tetrahedral sites) is known to be supportive of the efficient OER activity, with excellent thermodynamic stability. Hence, for such a non-precious metal oxide with the superior electrocatalytic property when compared to the precious metal based oxides such as RuO_2 and IrO_2, further improvement in terms of activity, with a primary focus to reduce the overpotential, is highly inevitable. In the previous chapter, it is found that Co_3O_4 nanostructures with different morphologies show enhanced electrocatalytic activity for OER. It is found that spherical nanoparticles of Co_3O_4 synthesized by a simple auto-combustion reaction are equally active compared with the porous nanorods prepared by a precipitation reaction.

Although, as like any functional material, the surface area, porosity, pore size, and morphology might influence the overall activity during OER, there are various other parameters which need to be addressed for a thorough understanding and designing of an efficient and economic OER electrocatalyst based on the spinel oxide Co_3O_4. Based on the characteristic properties and structural aspects, there are various parameters which could influence the overall electrocatalytic performance during OER. These are: (1) role of Co^{2+} and Co^{3+} ratio and their distribution in the two different crystallographic sites; (2) spin state of Co^{3+} such as high-spin, low-spin, and intermediate spin; and (3) e_g electron occupancy, etc. For Co_3O_4, the octahedrally coordinated Co^{3+} is anticipated to influence the catalytic activity through preferential adsorption of the reactant molecules.

It is decided to control the redox couple Co^{2+}/Co^{3+} in Co_3O_4 by partially replacing Co^{2+} with Zn^{2+} as in $ZnCo_2O_4$, to evaluate the influence of Co^{2+} on the OER performance. Zn^{2+} is known to occupancy the tetrahedral site in the spinel lattice. Also, the ionic size of Zn^{2+} (0.6 Å) is comparable with that of Co^{2+} (0.58 Å) [2].To compare their catalytic activity, different compositions of Zn-substituted Co_3O_4 were synthesized under identical conditions, following the auto-combustion method as reported in the previous chapter, to achieve a meaningful comparison. Inorder to achieve a more detailed information, a systematic variation of Zn has been followed for the synthesis of $Zn_xCo_{3-x}O_4$ where x = 0.2, 0.4, 0.6, 0.8 and 1. Further, all the as-prepared compositions are subjected to various characterizations such as XRD, BET surface area, TEM, UV-Vis spectra, magnetic and electrocatalytic

measurements to get a detailed understanding of the characteristic properties and the properties are correlated with the OER activity to identify the best possible catalytic formulation.

4.2 Synthesis

For the preparation of Zn-substituted cobalt oxide, $Zn_xCo_{3-x}O_4$ the auto-combustion method is followed. Detailed information of the synthetic methodology is described in Chapter 2. Briefly, stoichiometric amounts of cobalt nitrate, $Co(NO_3)_2.6H_2O$, and zinc nitrate $Zn(NO_3)_2.6H_2O$, dissolved in minimum amount of distilled water was mixed with glycine dissolved in minimum amount of distilled water and stirred vigorously to obtain a uniform solution. The mixed solution was evaporated slowly at 200 ℃, on a hot plate to initiate the auto-combustion reaction in a controlled manner. After the evaporation of water, the resulting thick mass burnt spontaneously to form a fluffy powder mass of zinc cobalt oxide. More detailed information such as composition, the mole ratio of metal ion(s) to glycine and respective sample code is given in Table 4.1.

Table 4.1 Details of composition and mole ratio of metal ions and glycine used

Sample code	**Composition**	**Mole ratio of $Zn(NO_3)_2.6H_2O$**	**Mole ratio of $Co(NO_3)_2.6H_2O$**	**Mole ratio of Metal nitrate to Glycine**
CO	Co_3O_4	0	3	1:0.45
ZCO 2	$Zn_{0.2}Co_{2.8}O_4$	0.2	2.8	1:0.42
ZCO 4	$Zn_{0.4}Co_{2.6}O_4$	0.4	2.6	1:0.39
ZCO 6	$Zn_{0.6}Co_{2.4}O_4$	0.6	2.4	1:0.36
ZCO 8	$Zn_{0.8}Co_{2.2}O_4$	0.8	2.2	1:0.345
ZCO 10	$ZnCo_2O_4$	1	2	1:0.30

In the present study, the lowest possible metal to glycine ratio was used for all the synthesis to get smaller particle size. For example, for the sample CO(Co_3O_4), the lowest possible glycine ratio was 1:0.45. Below this metal to glycine ratio, combustion did not occur. The presence of Zn reduced the minimum required glycine ratio. Thus, for ZCO10($ZnCo_2O_4$), the lowest possible glycine ratio was 1:0.3. For each composition, the lowest metal to glycine ratio was optimized by trials.

4.3 Characterization of as-prepared samples

4.3.1 X-ray diffraction

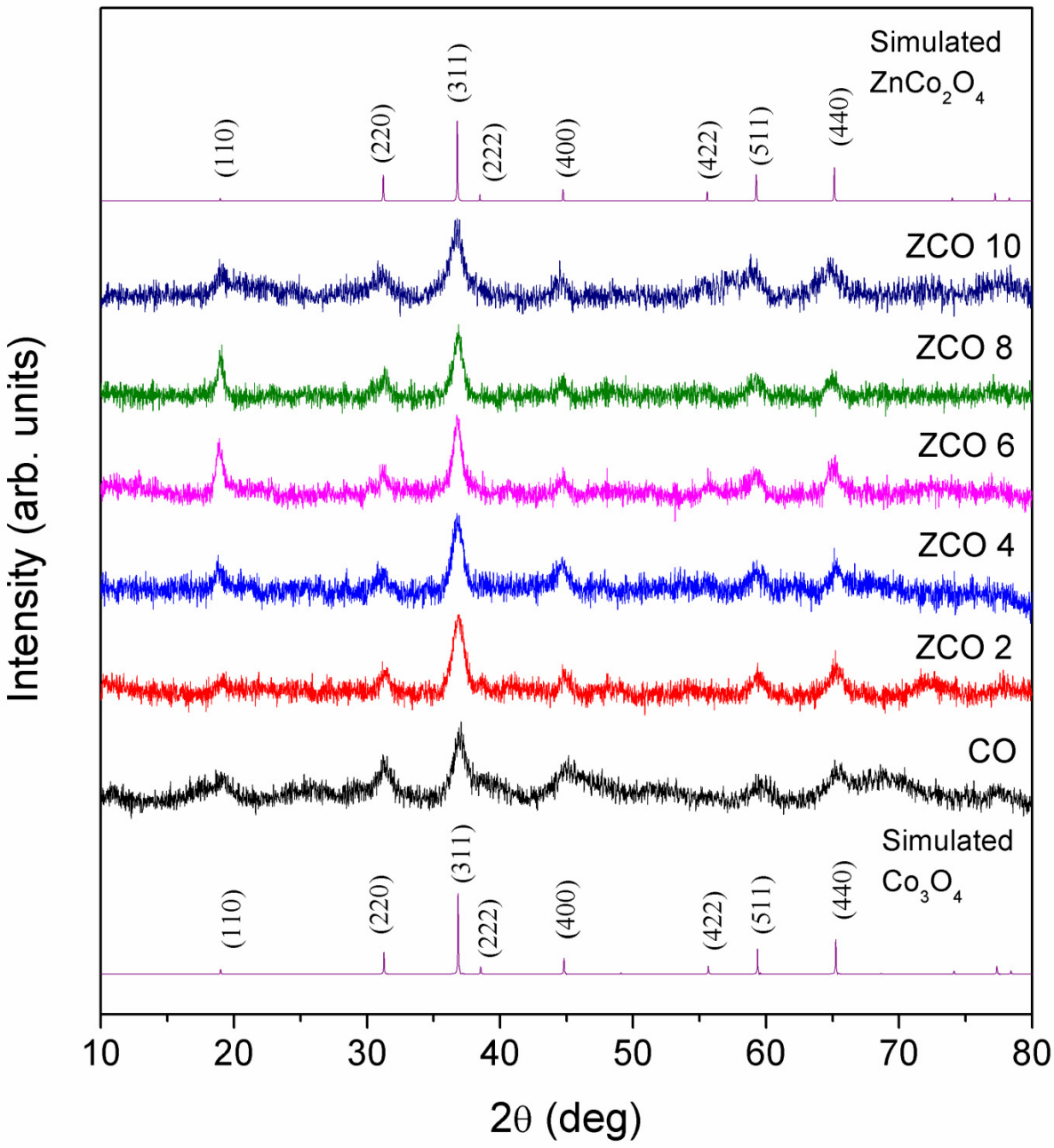

Figure 4.1 XRD patterns of the Zn-substituted cobalt oxide compositions compared with the with the simulated patterns of the end members

Figure 4.1 shows the powder XRD patterns of cobalt oxide (CO) and the zinc-substituted cobalt oxides (ZCO 2 to ZCO 10). The experimental patterns are compared with the simulated pattern of Co_3O_4 and $ZnCo_2O_4$. The powder pattern is simulated using the space group Fd3m and the corresponding cubic lattice parameter a = 8.084 Å for Co_3O_4 (JCPDS # 09-0418) and 8.0946 Å (JCPDS # 23-1390) for $ZnCo_2O_4$.

The experimental patterns match very well with the simulated ones confirming the formation of spinel phase. Also, it is clearly evident from the XRD patterns that the peaks are shifted gradually to lower 2θ values as a function of substitution of Zn (x from 0.2 to 1.0). Since Zn^{2+} has higher ionic radius (0.6 Å) compared to Co^{2+} (0.58 Å), substitution of Co^{2+} by Zn^{2+} increases the lattice parameter of the spinel lattice and hence increase in the d-spacing resulting in a shift towards the lower 2θ. The XRD patterns are matched with the simulated patterns using the PowderCell software and the lattice parameters are calculated by least-squares fitting. As expected, the lattice parameter increases with increasing Zn substitution. The calculated lattice parameters are given in Table 4.2 and a gradual increase in lattice parameter as a function of Zn doping is clearly evident. The lattice parameter reported for $ZnCo_2O_4$ is 8.0946 Å (JCPDS # 23-1390). In the present study, for ZCO 10 ($ZnCo_2O_4$) a larger lattice parameter of 8.1430 Å obtained. This can be due to the partial occupation of Zn^{2+} in the octahedral sites which has higher ionic radius than Co^{3+}. The average crystallite sizes are calculated using the Scherrer formula as shown Table 4.2.

Table 4.2 Lattice parameter and crystallite size of $Zn_xCo_{3-x}O_4$

Sample code	**lattice parameter a (Å)**	**Crystallite size (±1 nm)**
CO	8.075	7
ZCO 2	8.090	6
ZCO 4	8.084	11
ZCO 6	8.108	12
ZCO 8	8.116	10
ZCO 10	8.143	11

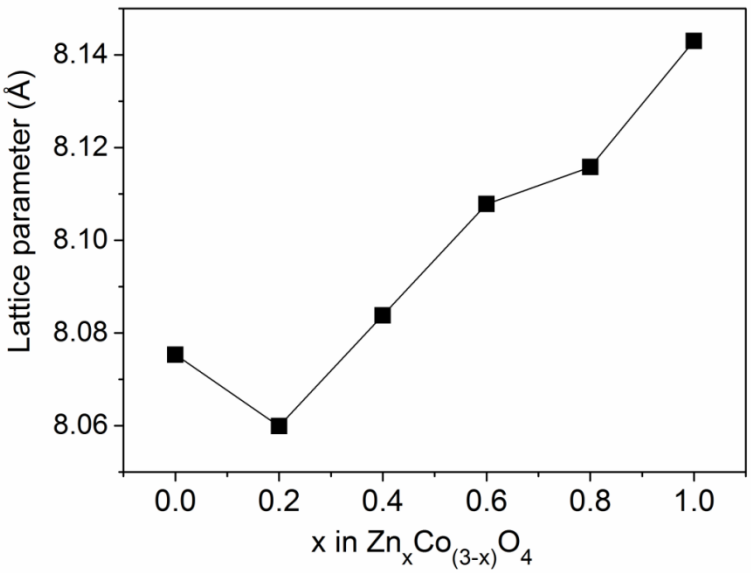

Figure 4.2 Variation of lattice parameter with the Zn content in $Zn_xCo_{3-x}O_4$

4.3.2 TEM studies

Figure 4.3 shows the TEM images of the as-prepared $Zn_xCo_{3-x}O_4$ powders. It is apparent from the images that the particles are spherical in nature and aggregated together into small clusters. Also, it is evident from the images that the particles are approximately 6-10 nm in size. The changes in the mole ratio of metal to glycine (Table 4.1) from CO to ZCO 10 did not affect the morphology and particle size considerably.

4.3.3 Surface area

Results of the nitrogen adsorption-desorption studies on $Zn_xCo_{3-x}O_4$ powders are shown in Figure 4.4. The nature of the hysteresis loop confirms type IV isotherm and it is a characteristic behavior of the mesoporous materials [3]. The BET surface area of all the samples is given in Table 4.3. It is clearly evident from Table 4.3 that the surface area is increasing gradually with increasing Zn content in $Zn_xCo_{3-x}O_4$ and reaches a maximum surface area of 119 m^2/g for ZCO 8 and decreased further for ZCO 10.

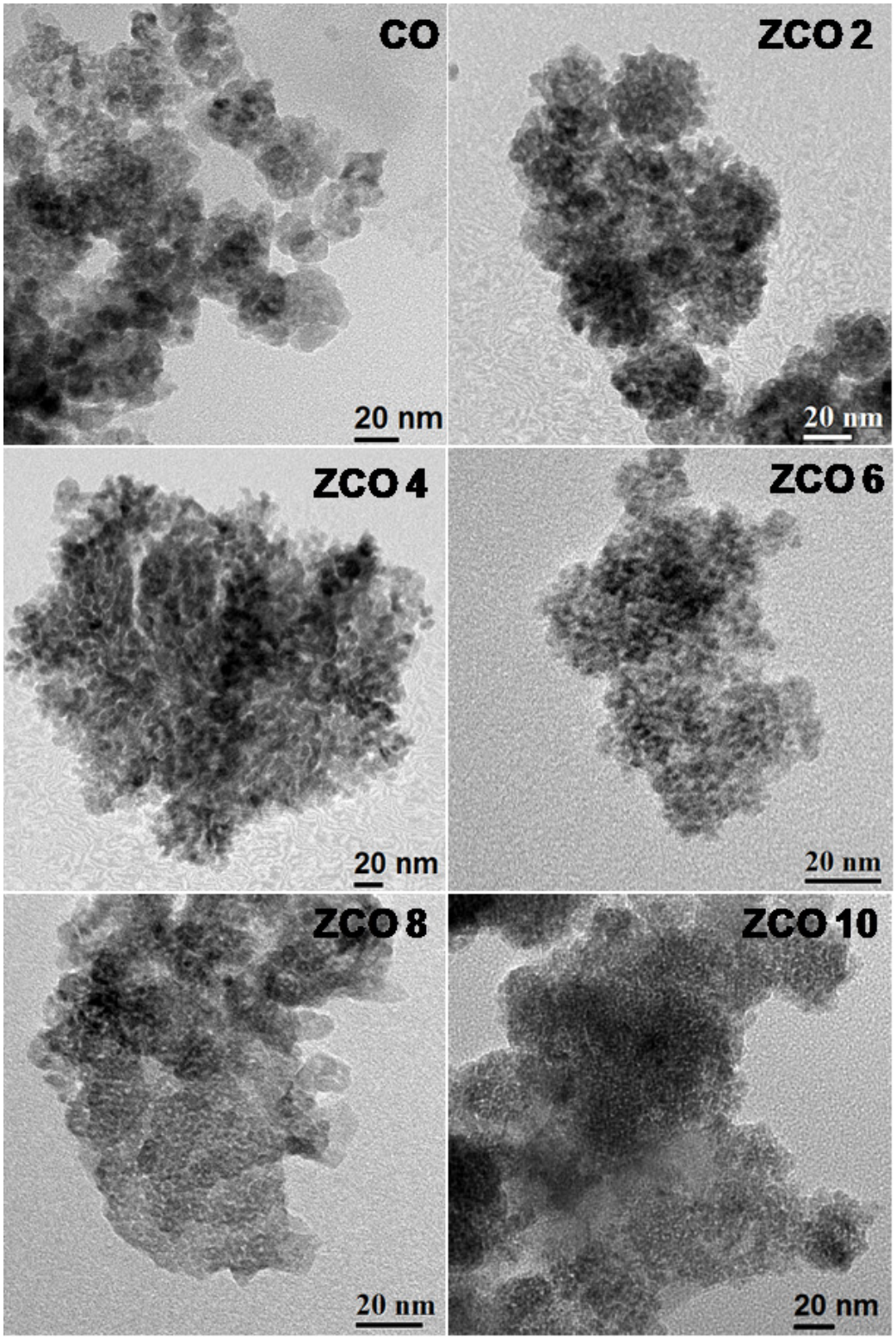

Figure 4.3 TEM images of different compositions in $Zn_xCo_{3-x}O_4$

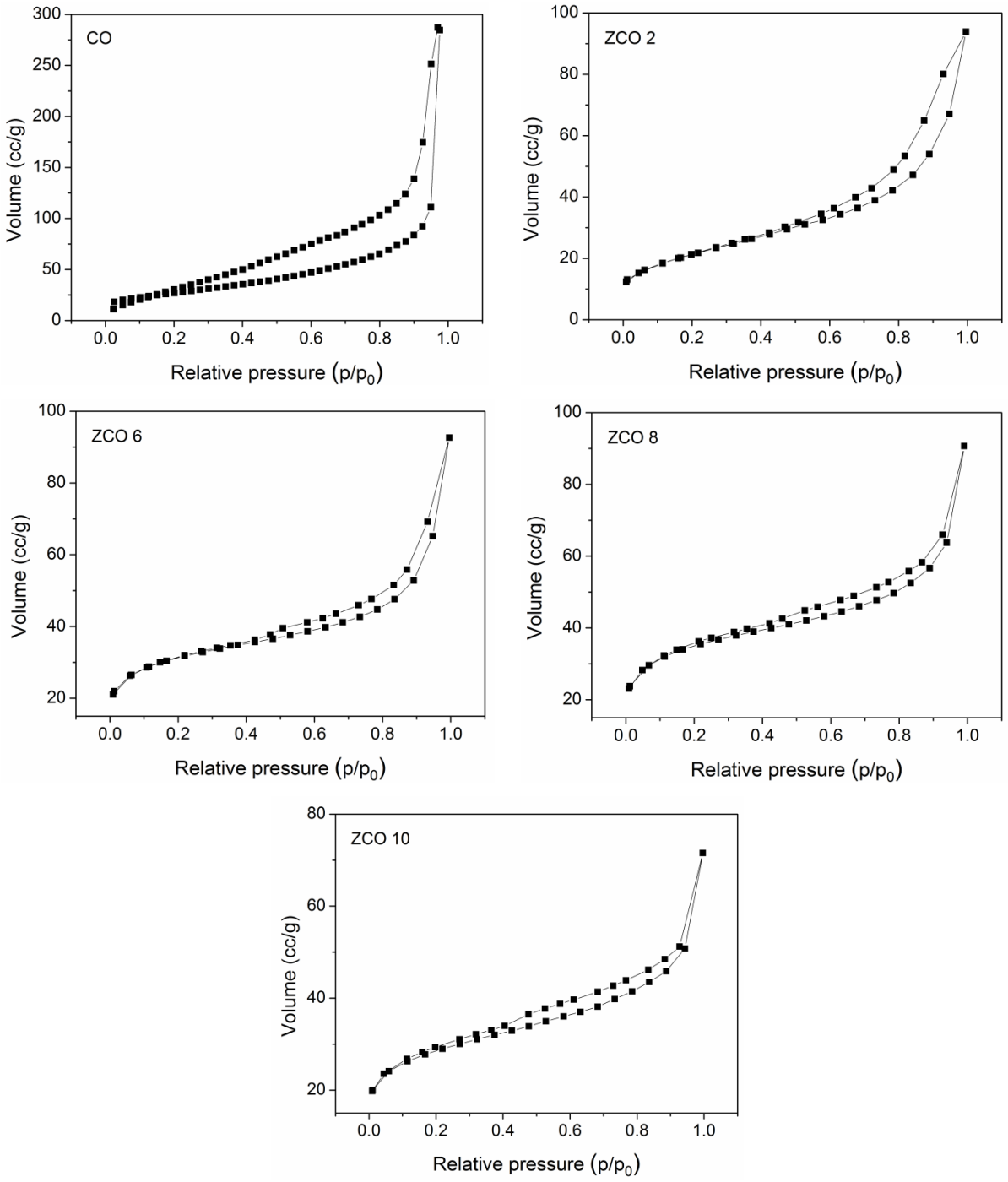

Figure 4.4 Nitrogen adsorption-desorption curves of $Zn_xCo_{3-x}O_4$ in different compositions

Table 4.3 BET surface area of $Zn_xCo_{3-x}O_4$

Sample code	BET surface area (m^2/g)
CO	70
ZCO 2	76
ZCO 6	106
ZCO 8	119
ZCO 10	97

4.3.4 X-ray photoelectron spectroscopy

X-ray photoelectron spectroscopy (XPS) studies have been carried out to get information on the oxidation states of Co in Co_3O_4. In general, upon changes in the oxidation state, changes in the XPS binding energy (BE) can be expected from the chemical effects. In the case of cobalt, the BE value of inner-shell electrons of Co^{3+} ions is smaller than that of Co^{2+} ions. It can be due to the smaller effective charge due to the higher degree of covalency of the bonds. For the spinel type cobalt oxide, the energy separation between Co $2p_{3/2}$ and Co $2p_{1/2}$ is approximately 15.1 eV [4]. Figure 4.5(a, b) shows the XPS spectra of representative samples of $Zn_xCo_{3-x}O_4$. The binding energy separation of the sample CO, which corresponds to Co_3O_4 is in agreement with the literature values. The XPS spectrum of CO shows two major peaks with binding energy values of 780.6 eV and 795.5 eV, corresponding to Co $2p_{3/2}$ and $2p_{1/2}$ core levels, respectively, of the Co_3O_4 phase [5-6]. The formation of Co_3O_4 is further confirmed by the presence of a weak satellite peak between the main peaks Co $2p_{3/2}$ and Co $2p_{1/2}$ [5, 7]. The typical satellite peak is observed at a binding energy value of 789.6 eV, about 9.03 eV higher than the BE of Co $2p_{3/2}$. Lack of prominent shake-up satellite peaks in the Co 2p spectra further suggests the presence of mainly Co_3O_4 phase. The Cobalt compounds of valence 2+ are paramagnetic and have a strong satellite peak around 6 eV above the Co $2p_{3/2}$ line, whereas Co^{3+} does not show any satellites. The mixed valence Co_3O_4 has a weak satellite peak that characterizes the minor component Co^{2+}. Thus the XPS measurement confirms the formation of Co_3O_4. The Co 2p spectra of Zn-substituted samples ZCO 4 and ZCO 8 are also shown in the Figure. The observed binding energy values for ZCO 4 and ZCO 8 is 780.21 (Co $2p_{3/2}$); 795.6 (Co $2p_{1/2}$) and 779.54 (Co $2p_{3/2}$); 794.66 (Co $2p_{1/2}$) respectively. For the ZCO 4 and ZCO 8 samples the Co $2p_{3/2}$ - Co $2p_{1/2}$peak separation is obtained as 15.1 eV, which is comparable to that observed for CO (Figure 4.5a). Compared to Co_3O_4 (CO), a negative shift is observed in the Co 2p spectra for the Zn substituted samples (ZCO4 and ZCO8). This is probably due to the incorporation of Zn^{2+} in Co_3O_4, which reduces the population of Co^{2+} [8] and the Co 2p spectra is mainly from Co^{3+} which has smaller BE for the inner-shell electrons than for Co^{2+}. The Co 2p spectra are fitted to get information on the Co^{2+} and Co^{3+} content in the different samples. Table 4.4 shows the Co^{2+}/Co^{3+} ratio calculated by integrating the area under the individual curves of the XPS spectra. It shows that Co^{2+}/Co^{3+} ratio decreases with increasing the Zn content in the samples from CO to ZCO 8.

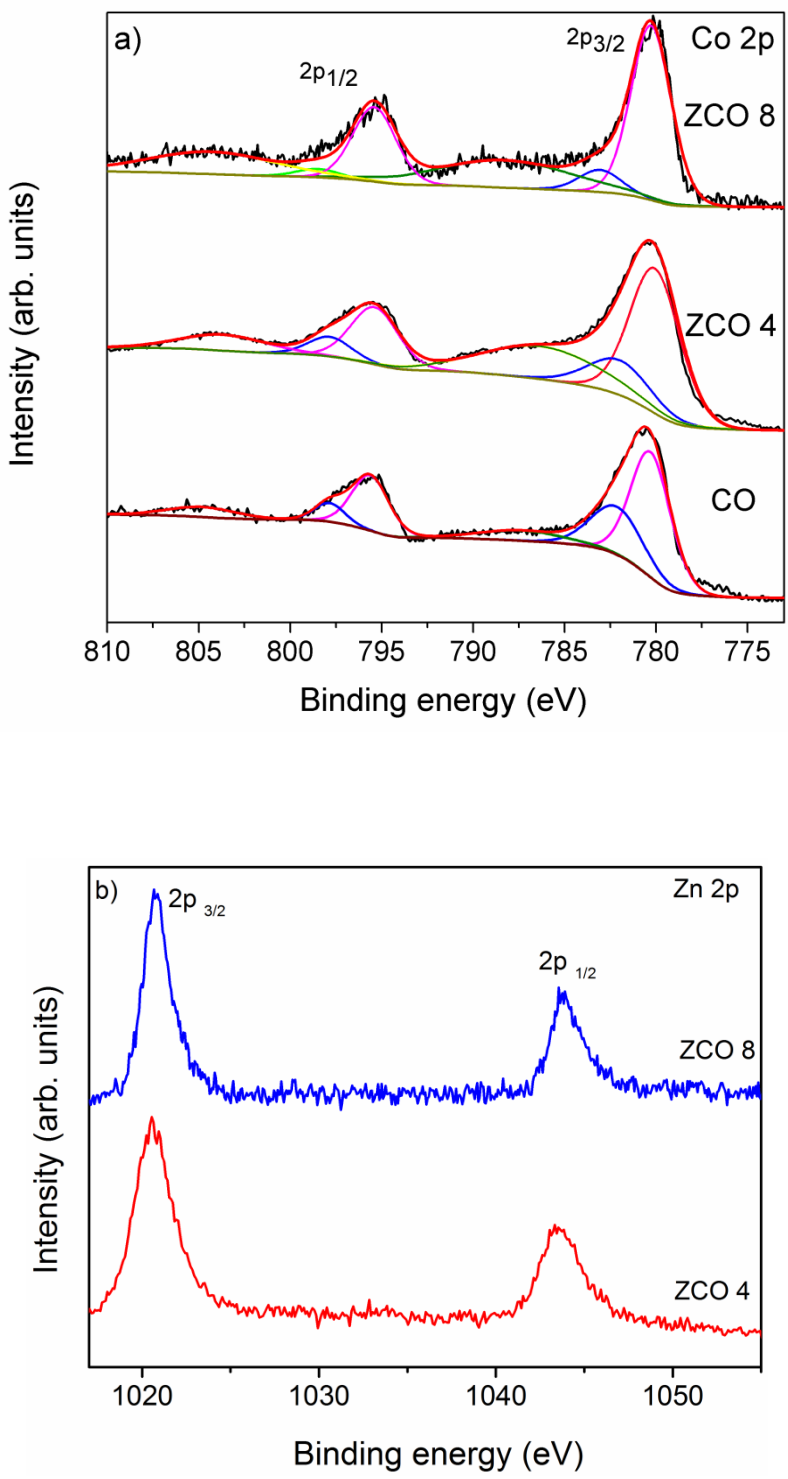

Figure 4.5. Co 2p and Zn 2p XPS spectra of $Zn_xCo_{3-x}O_4$.

Table 4.4 Comparisons of the ratios of Co^{2+}/Co^{3+}obtained from the XPS spectra

Sample name	Co^{2+}/Co^{3+}	Expected ratio
CO (Co_3O_4)	0.49	0.5
ZCO 4 ($Zn_{0.4}Co_{2.6}O_4$)	0.31	0.3
ZCO 8 ($Zn_{0.8}Co_{2.2}O_4$)	0.11	0.1

Also, for Zn substituted samples, a weak satellite peak is observed at a binding energy of about ~788.86 eV, which is a characteristic feature of the presence of cobalt in the +3 oxidation state supporting the effectiveness of Zn substitution to precisely control the oxidation state of cobalt. The Zn 2p spectra shows two peaks with binding energy values 1020.5 (Zn $2p_{3/2}$) and 1043.3 eV (Zn $2p_{1/2}$) for ZCO 4; and 1020.1 eV (Zn $2p_{3/2}$) and 1043.05 eV (Zn $2p_{1/2}$) for ZCO 8, respectively. The binding energy difference value between Zn $2p_{3/2}$ - Zn $2p_{1/2}$ is approximately 22.8 (ZCO 4) and 22.9 eV (ZCO 8) confirming the presence of Zn in +2 oxidation state [9].

4.3.5 Magnetic susceptibility

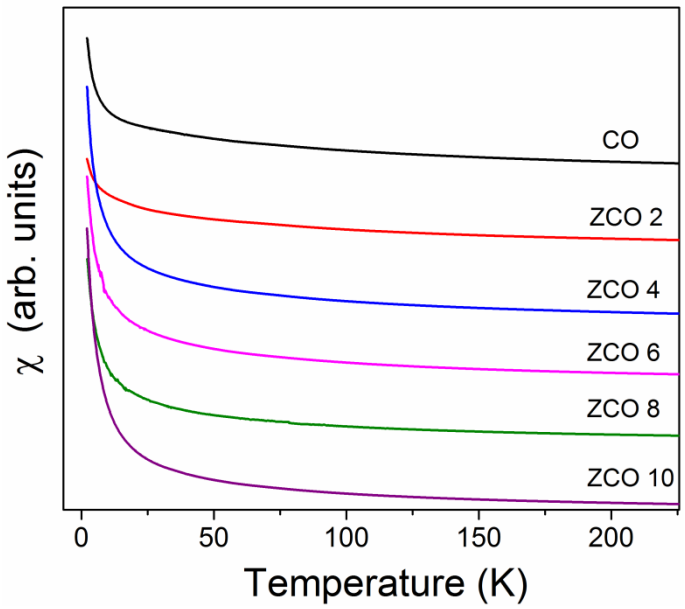

Figure 4.6 DC magnetic susceptibility curves of $Zn_xCo_{3-x}O_4$.The curves are shifted along the y-axis.

Figure 4.6 shows DC magnetic susceptibility curves of the as-prepared Zn substituted Co_3O_4 measured in a magnetic field of 1 T. The magnetic susceptibility curves clearly indicate the

paramagnetic behavior of the samples. Figure 4.7 shows the 1/χ vs T curves. Above 100 K all curves show straight-line behavior and follow the Curie-Weiss law [10]. The inverse of the slope of the straight line gives the Curie constant, and the total spin is calculated from the Curie constant as described in section 2.3.5, chapter 2.

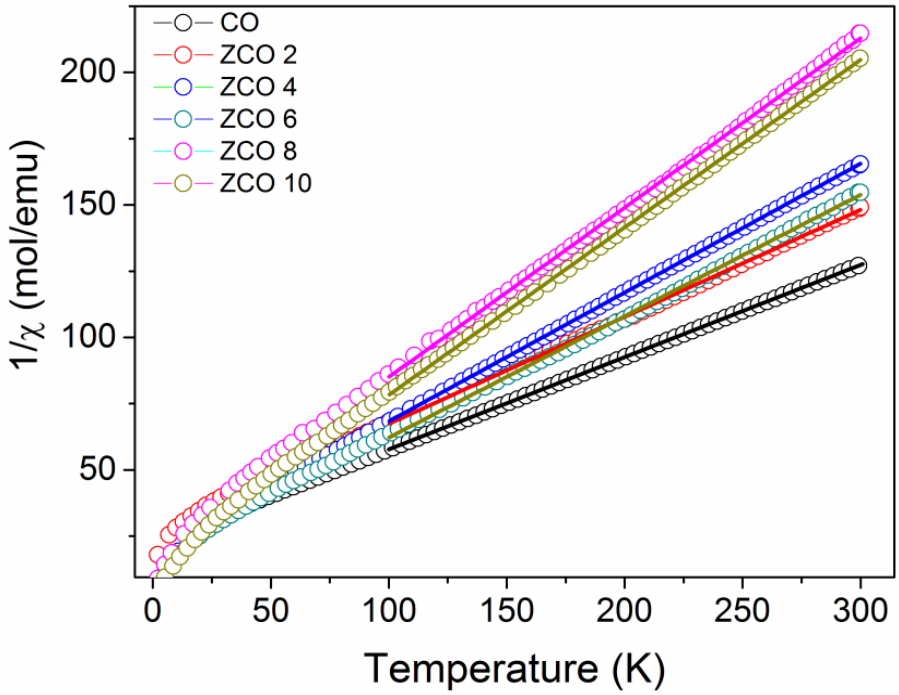

Figure 4.7 Temperature variation of the inverse susceptibilities of $Zn_xCo_{3-x}O_4$. The solid lines are fit to the Curie-Weiss law.

In general, Co^{2+} is d^7 high spin system with 3 unpaired electrons and its spin value is equal to S =3/2. Ideally, in Co_3O_4, Co^{3+} is in the low spin state and the total magnetic moment is mainly coming from the unpaired electrons in the Co^{2+} [11-13]. Based on this, we have calculated the magnetic moment of $Zn_xCo_{3-x}O_4$ by two different assumptions (i) two Co^{3+} are in the low-spin state (ii) one Co^{3+} is in the low-spin state and one Co^{3+} is in the high-spin state. The total spin calculated based on these assumptions are plotted in Figure 4.8 and compared with the experimentally obtained spin values. The experimental spin values are in between the values calculated using the two assumptions. The Figure shows that when the Zn content in $Zn_xCo_{3-x}O_4$ increases, the spin values are approaching towards a combination of high-spin Co^{3+} + low-spin Co^{III}. Thus, with increasing Zn content in $Zn_xCo_{3-x}O_4$, the population of high spin Co^{3+} increases. To get a clear picture of the spin contribution from high-spin Co^{3+}, the spin contribution from Co^{2+} is subtracted from the total spin and plotted in Figure 4.9.

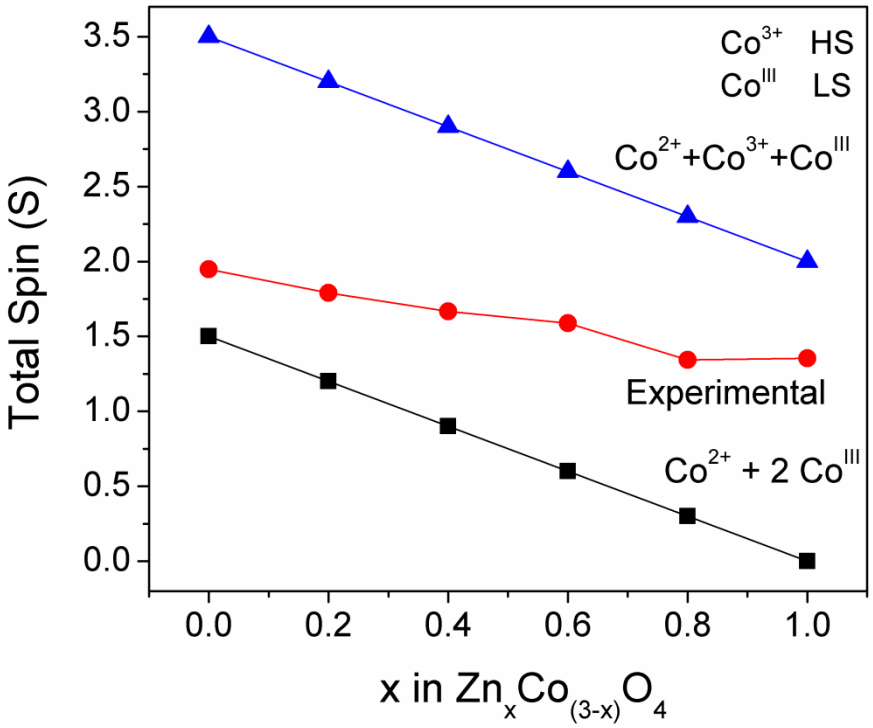

Figure 4.8. Comparison of experimental spin values of $Zn_xCo_{3-x}O_4$, with the two assumptions as described in the text.

$$\text{spin contribution from } Co^{3+} = \text{Total spin} - (1 - x)\frac{3}{2}$$

Figure 4.9 clearly shows that the spin contribution from Co^{3+} is increasing gradually with increasing the Zn content in $Zn_xCo_{3-x}O_4$. The calculated Curie constant and the spin values are given in Table 4.5.

Table 4.5 Curie constant and spin values of $Zn_xCo_{3-x}O_4$ from the magnetic studies

Sample code	Curie constant (emu K mol^{-1})	Total spin	Spin contribution from Co^{3+}
CO	2.87	1.94	0.45
ZCO 2	2.48	1.79	0.59
ZCO 4	2.20	1.66	0.77
ZCO 6	2.05	1.58	0.99
ZCO 8	1.55	1.34	1.04
ZCO 10	1.58	1.35	1.35

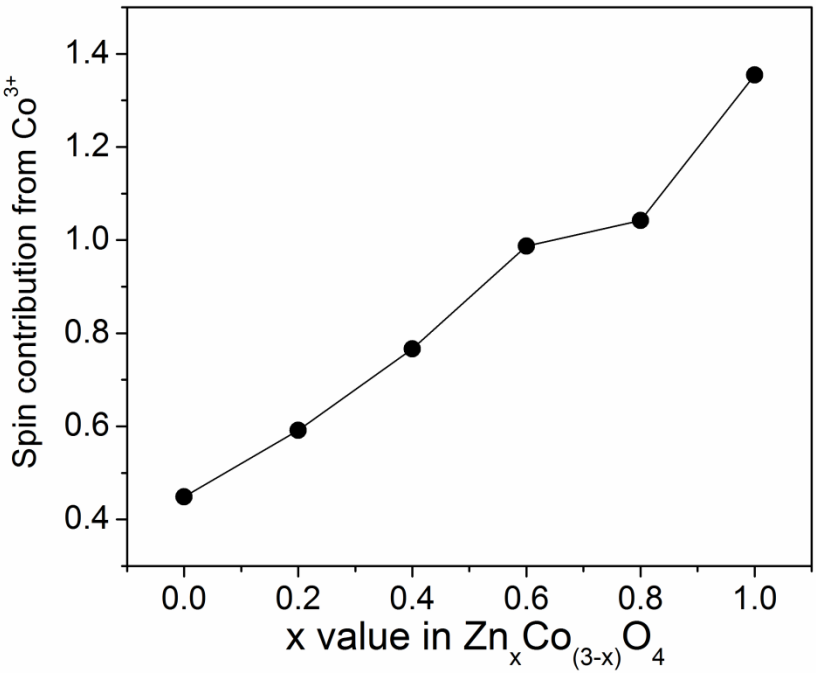

Figure 4.9 Spin contribution from Co^{3+} in $Zn_xCo_{3-x}O_4$.

4.3.6 UV-Visible spectroscopy

UV-Visible spectroscopy was utilized to study the electronic structure of $Zn_xCo_{3-x}O_4$. The absorption spectra recorded in the range of 200 – 2000 nm are shown in Figure 4.10(a,b). In $Zn_xCo_{3-x}O_4$, the substitution of Zn is expected to replace the Co^{2+}. This is apparently evident from the decrease in the intensity of peak related to Co^{2+} transitions at higher wavelength region (1200 -1800 nm) with an increase in the Zn content, as shown in Figure 4.11 after correcting for the baseline. For a further detailed analysis and clarity, all the absorption spectra are deconvoluted using the peakfit software using the Gaussian deconvolution function. The deconvoluted spectra are shown in Figure 4.12.

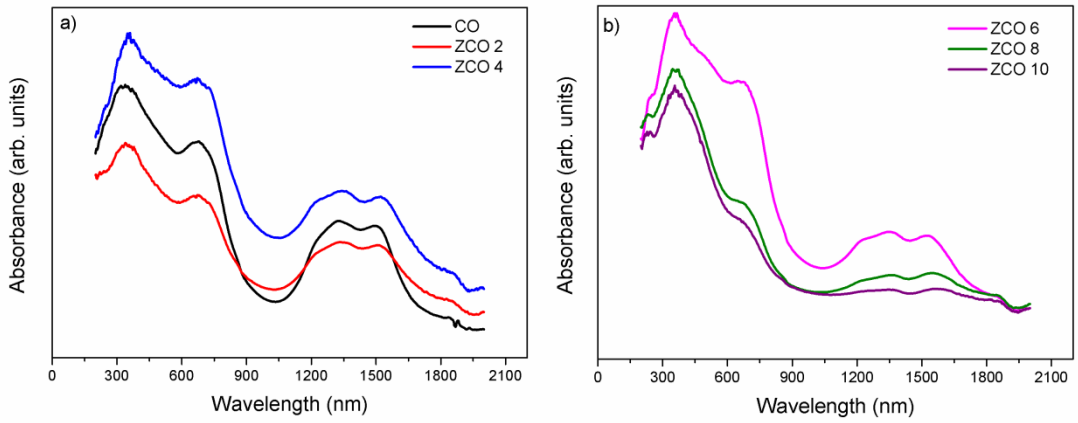

Figure 4.10 (a,b) Absorption spectra of $Zn_xCo_{3-x}O_4$ without baseline correction

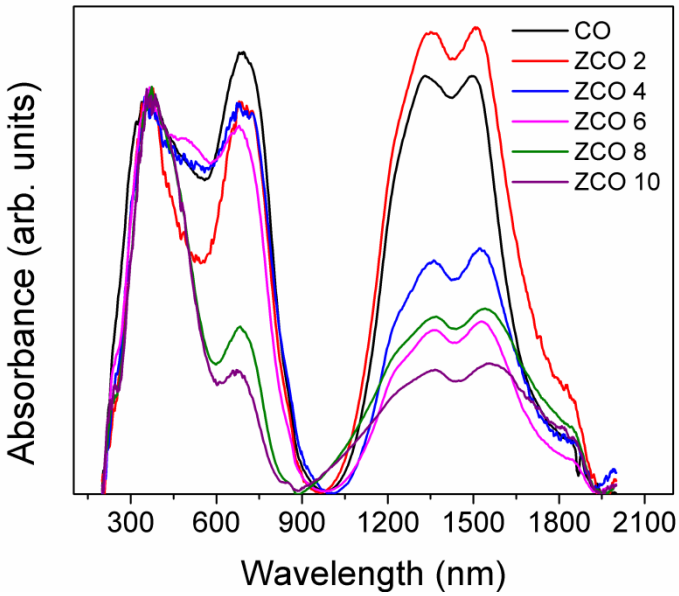

Figure 4.11 Absorption spectra of $Zn_xCo_{3-x}O_4$ after baseline correction and normalization with respect to the peak at 350 nm.

The peak assignments are given in the Table 4.6. The absorption spectra consist of all the characteristic features of Co_3O_4 and $ZnCo_2O_4$ [14-19].The deconvolution of the spectra discloses some interesting features about the electronic structure of the Zn substituted cobalt oxide. Peak 1 in the range of 334 – 359 nm (3.70 – 3.46 eV) can be assigned to the Ligand to Metal Charge Transfer (LMCT) from p O^{2-} to d Co^{3+} [15]. High-spin Co^{3+} d-d transition can be confirmed from the peak 2 obtained in the range 2.77 – 2.44 eV (446-506 nm). During this transition, charge transfer happens from antibonding orbital $\sigma^* e_g^{\alpha} \rightarrow \sigma^* e_g^{\beta}$ of octahedral Co^{3+} [20]. The charge transfer transition between t_{2g} states of octahedral Co^{3+} to the t_2 states of tetrahedral Co^{2+} is evident from peak 3, the transition at 1.8 – 1.75 eV (691.55 – 709.4 nm) [16]. Further, the decrease in intensity of this transition due to Zn substitution confirms the replacement of Co^{2+} with Zn^{2+}. A minor transition in the region 1.47 – 1.44 eV (844 – 863 nm) is also observed as a result of some electronic transitions caused by the oxygen vacancies [15]. The d-d transition from Co^{2+} $\pi^2 t_2$ to Co^{3+} $\sigma^* e$ can be matched to peak 5 in the region 1 - 1.02 eV (1232 - 1219 nm) [16]. Peak 6 (0.925 -0.912 eV, 1339.3 – 1360 nm) can be assigned to the transition from Co^{2+} to e_g^* Co^{3+} [16]. Peak 7 is due to Co^{2+} $\pi^* e$ to Co^{2+} $\pi^* t_2$, obtained at 0.825 - 0.78 eV (1503 - 1588 nm) [16].

The peak in the region 2.77 – 2.44 eV (446 - 506 nm) is due to the presence of Co^{3+} high-spin in the lattice. Usually, in Co_3O_4 and $ZnCo_2O_4$, Co^{3+} prefers the octahedral site with

low-spin configuration, which is diamagnetic and possesses no magnetic moment. It is

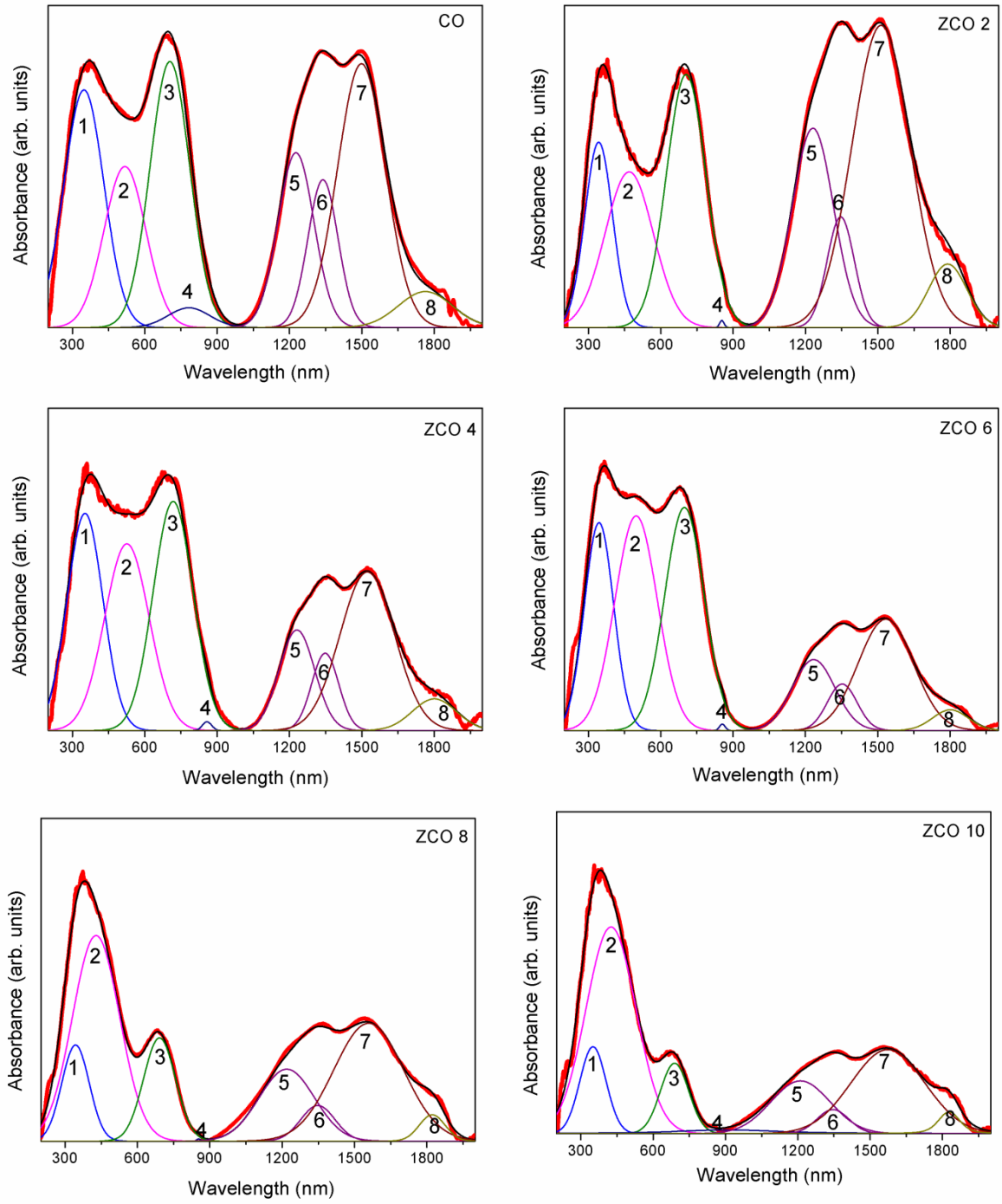

Figure 4.12 Deconvoluted absorbance spectra of $Zn_xCo_{3-x}O_4$

because the splitting Δ_0 (19000 cm^{-1}) [12] is much higher than the electron pairing energy of11600 cm^{-1} [21]. However, Belova *et al* reported that in non-stoichiometric Co_3O_4 films, the tetragonal distortion creates crystal lattice defects which stabilize Co^{3+} high-spin configuration in the octahedral sublattice. Also, the authors carried out Self-consistent field $X\alpha$ scattered wave cluster method (SCF X αSW) calculations to get detailed information

Table 4.6 Assigned transitions for the deconvoluted peaks in the absorption spectra of $Zn_xCo_{3-x}O_4$

No	Energy of the bands		Transition	References
	in eV	in nm		
Peak 1	3.70 – 3.46	334-359	LMCT $O^{2-} \rightarrow Co^{2+}$	[15]
Peak 2	2.77 – 2.44	446- 506	Co^{3+} (H.S) d-d $\sigma^* e_g^{\alpha} \rightarrow \sigma^* eg^{\beta}$ Co	[20]
Peak 3	1.8 – 1.75	691.5 – 709.4	t_{2g} (Co^{3+}) $\rightarrow t_2$ (Co^{2+})	[16]
Peak 4	1.47 – 1.44	844 – 863	Due to some electronic defects by oxygen vacancies	[15]
Peak 5	1 -1.02	1232 - 1219	Co^{2+} $\pi\ ^2t_2 \rightarrow Co^{3+}$ $\sigma^* e$	[16]
Peak 6	0.925 -0.912	1339.3 – 1360	$Co^{2+} \rightarrow e_g^*$ Co^{3+}	[16]
Peak 7	0.825 - 0.78	1503 - 1588	Co^{2+} $\pi^* e \rightarrow \pi^* t_2$	[16]

about the electronic structure. According to the calculation, the 3d orbitals are split as shown in Figure 4.13. The energy gap between the valence top band (e_g^{α}) and the unoccupied conduction band (e_g^{β}) is 2.61 eV [20] which is matching with the observed band at 2.85 eV.

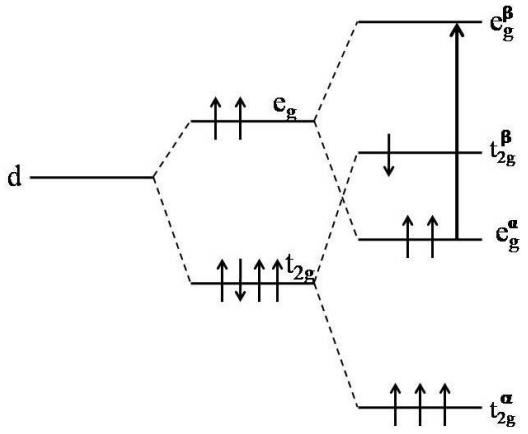

Figure 4.13 3d-energy levels splitting of high spin Co^{3+} ions

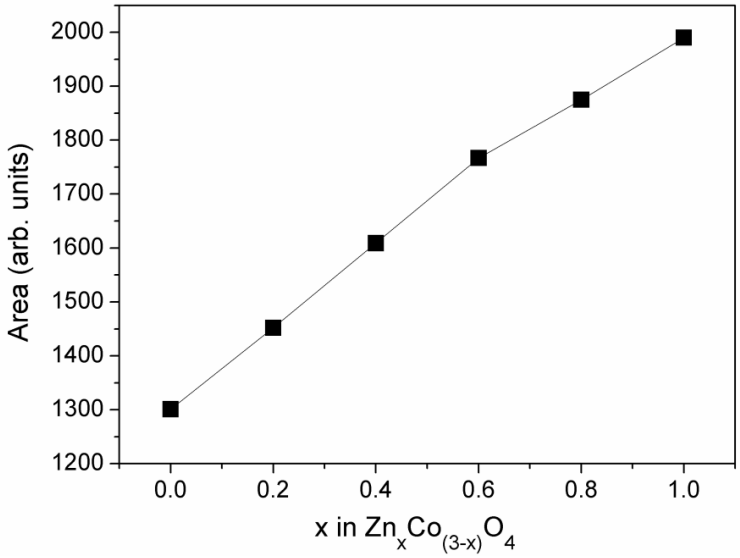

Figure 4.14 Variation of the area of the peak 2 which corresponds to the high-spin Co^{3+} transition as a function of Zn content in $Zn_xCo_{3-x}O_4$

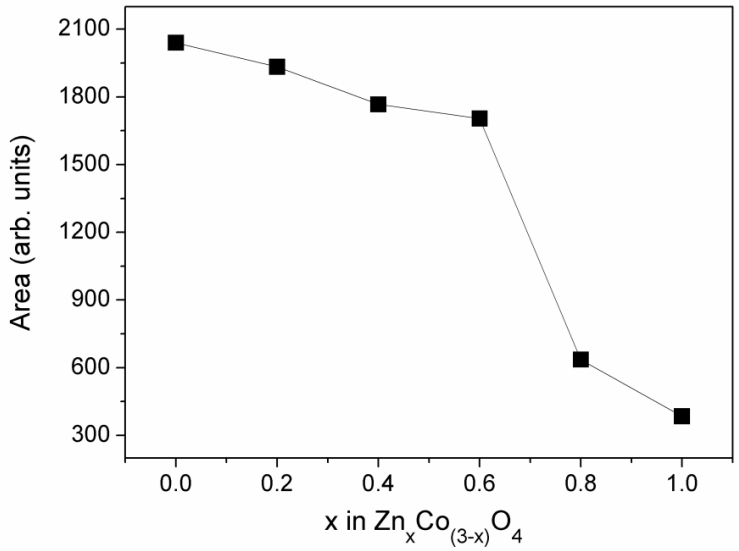

Figure 4.15 Variation of the area of peak 3 which corresponds to the transition from Co^{3+} to Co^{2+} as a function of Zn content in $Zn_xCo_{3-x}O_4$

In the present study, peak 2 is obtained at 2.46, 2.46, 2.45, 2.52, 2.71 and 2.78 eV, respectively, for CO, ZCO 2, ZCO 4, ZCO 6, ZCO 8, ZCO 10. These peaks can be assigned to the transition $\sigma^* e_g^{\alpha} \rightarrow \sigma^* e_g^{\beta}$ Co (Figure 4.13). Moreover, the area of the peak 2 which corresponds to the transition of high-spin Co^{3+}increases with the increase in the Zn content in $Zn_xCo_{3-x}O_4$ (Figure 4.14). It shows that Zn doping increases the population of high-spin Co^{3+}. In a similar way, since Zn^{2+} replaces the Co^{2+}**,** the area of peak 3 which corresponds to the

transition t_{2g} (Co^{3+}) → t_2 (Co^{2+}) also decreases with the increase in the Zn content in $Zn_xCo_{3-x}O_4$ (Figure 4.15).This confirms that Zn^{2+} replaces Co^{2+} in Co_3O_4.

4.4 Electrochemical studies

4.4.1 Cyclic voltammetry

Figure 4.16 shows the cyclic voltammograms of $Zn_xCo_{3-x}O_4$ in 0.1 M KOH. All the samples show the characteristic redox behavior of cobalt oxide [22]. The voltammogram exhibit two anodic peaks (Al, A2) corresponding to oxidation of Co^{2+} to Co^{3+}, and Co^{3+} to Co^{4+}, respectively. The observed cathodic peak (C1) is due to the reduction of Co^{4+} to Co^{3+}. This can be well explained by the following equations [23-24].

$$Co(OH)_2 + OH^- \rightarrow CoOOH + H_2O + e^- \quad \text{(A1)}$$

$$CoOOH + OH^- \rightarrow CoO_2 + H_2O + e^- \quad \text{(A2)}$$

$$CoO_2 + H_2O + e^- \rightarrow CoOOH + OH^- \quad \text{(C1)}$$

During the electrochemical reaction, Co^{3+} to Co^{4+} transition has a vital role in deciding the oxygen evolution reaction activity of cobalt oxide. Also, it is generally accepted that the minimum required potential for OER is higher than the Co^{3+} to Co^{4+} potential [25]. Hence, a precise tuning of cobalt oxide favoring the transition of Co^{3+} to Co^{4+} at a lower potential which in turn would result in higher activity.

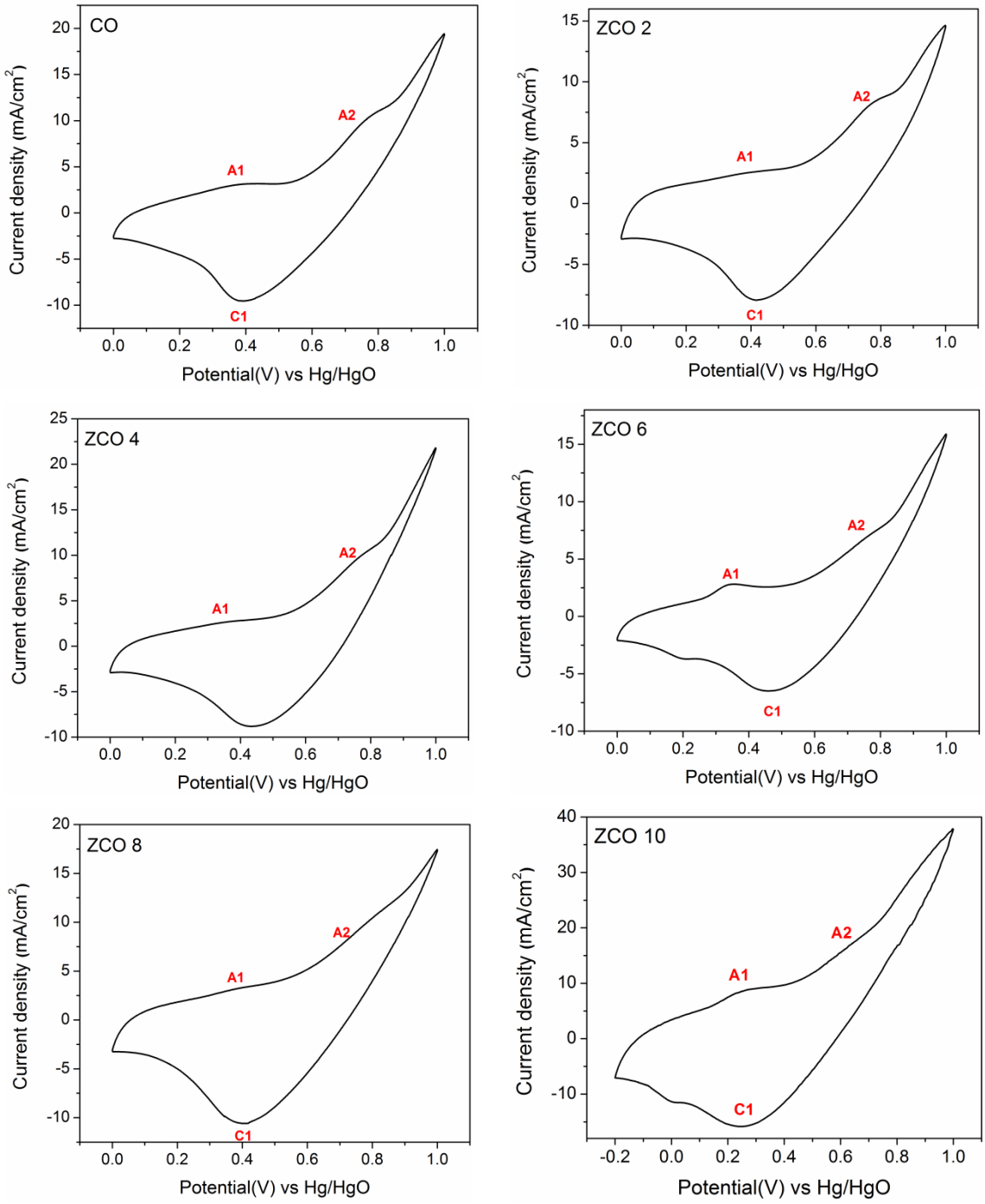

Figure 4.16 Cyclic voltammetry curves of $Zn_xCo_{3-x}O_4$ in 0.1 M KOH, recorded at the scan rate of 50 mV/s

4.4.2 Tafel plots

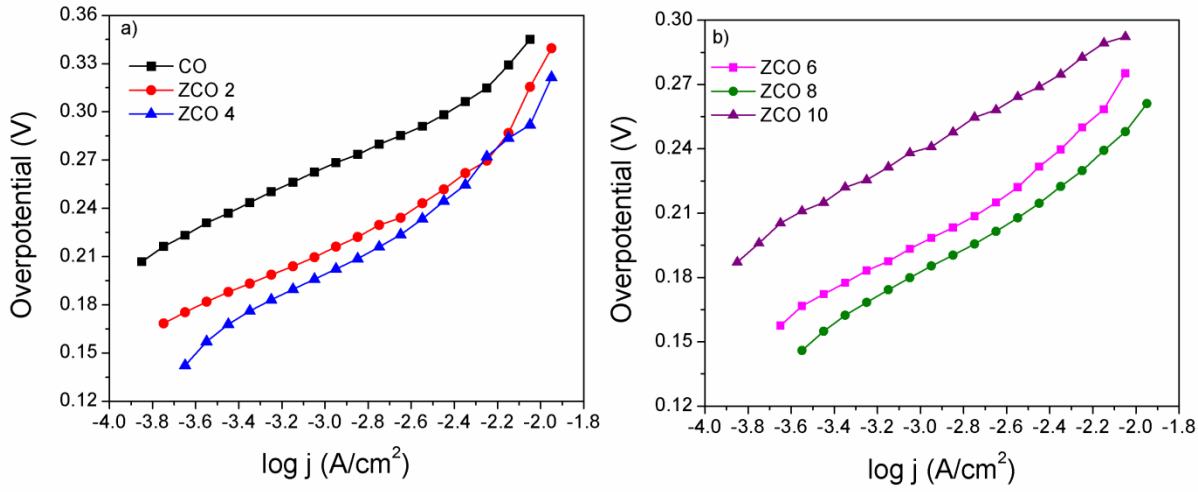

Figure 4.17 (a,b) Tafel plots of $Zn_xCo_{3-x}O_4$.

An efficient electrocatalyst for the OER should have lower overpotential and higher exchange current density for good electrocatalytic activity. Galvanostatic Tafel polarization represented as the overpotential (η) vs log (current density (j)) is a useful technique to reveal the in depth electrochemical properties of electrocatalysts. It gives detailed information about the kinetic parameters such as overpotential, Tafel slope and exchange current density. The parameters above for the different compositions $Zn_xCo_{3-x}O_4$ are given in Table 4.7.The overpotential (η) vs log (current density (j)) curves (Figure 4.17 (a,b)) show a straight line with a Tafel slope after the manual correction for the uncompensated resistance.

Table 4.7 Overpotential, Tafel slope and exchange current density parameters from Tafel plots of $Zn_xCo_{3-x}O_4$.

Sample code	Overpotential(η) at 10 mA/cm^2 (mV)	Tafel slope (mV)	Exchange current density (A/cm^2)
CO	358	62	5.2 x 10^{-8}
ZCO 2	325	65	4.8 x 10^{-7}
ZCO 4	306	76	2.2 x 10^{-6}
ZCO 6	287	67	1.1 x 10^{-6}
ZCO 8	254	68	2.1 x 10^{-6}
ZCO 10	300	60	1.0 x 10^{-7}

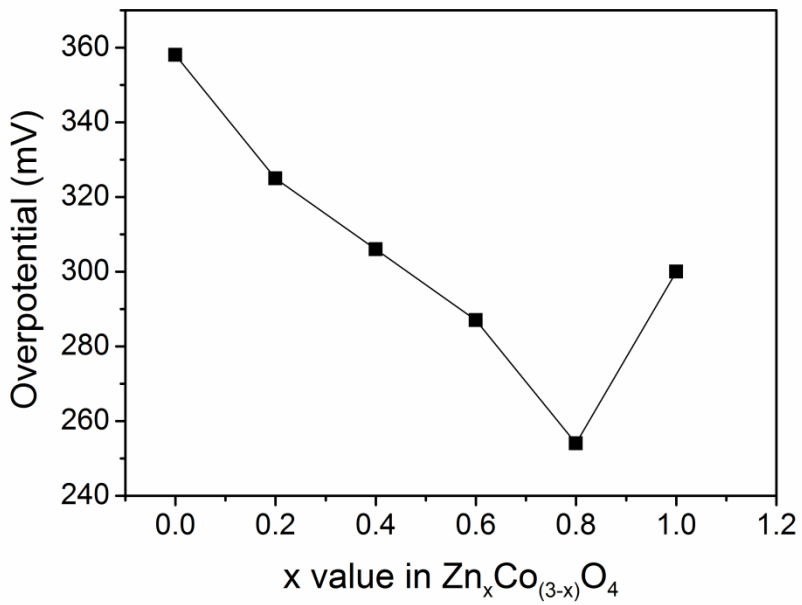

Figure 4.18 Variation of overpotential with the Zn content in $Zn_xCo_{3-x}O_4$

All the catalysts show a very good exchange current density in the range of 10^{-8} - 10^{-6} A/cm^2 with the Tafel slope of 60 - 76 mV and also it is observed that Zn doping increases the exchange current density from 10^{-8} A/cm^2 to 10^{-6} A/cm^2. Higher exchange current density implies higher catalytic activity, represented in terms of lower overpotential. The exchange current density is defined as the rate of the reaction at zero overpotential. From Table 4.7, it is apparent that the overpotential decreases almost linearly as a function of Zn substitution in $Zn_xCo_{3-x}O_4$ up to the value of x = 0.8 (ZCO 8) and further increased for ZCO 10 (x=1) which corresponds to $ZnCo_2O_4$ resulting in higher overpotential due to poor electrocatalytic activity. In the present case, although the Co^{3+} is vital for higher activity, mixed valence nature is mandatory as it is clear from the lower activity of ZCO 10 comprised of only Co^{3+} in the octahedral site (Figure 4.18). Moreover, ZCO 8 has lower overpotential (254 mV) compared to the overpotential of $ZnCo_2O_4$ reported in the literature as 320 mV (at 10mA/cm^2) [8] and 390 mV (at 10 mA/cm^2) [26], which are synthesized by different methods.

4.4.3 Mott-Schottky analysis

Semiconductor electrochemistry plays an important role in the electrocatalysis by metal oxide semiconductors. When a semiconductor is dipped in an electrolyte, immediately it forms electrode-electrolyte interface by aligning the energy levels of the semiconductor and the electrolyte. This is called band bending. For a p-type semiconductor, the Fermi level is lower than the redox potential of the electrolyte. Therefore, the electrons must transfer from

the electrolyte to the electrode to attain the equilibrium, which generates a negative charge in the space-charge region and causes the downward bending in the band edges [27].

Capacitance measurement on the electrode/electrolyte interface has been carried out to see the variation of carrier density on Zn-substitution in $Zn_xCo_{3-x}O_4$ .Mott-Schottky plot, which is a plot of $1/C^2$ *vs* applied potential (V) at a fixed frequency (where, C is the space-charge capacitance of the semiconductor) of 1 kHz is used to analyze the carrier density of $Zn_xCo_{3-x}O_4$.The capacitance measurements are presented as per the equation (Mott-Schottky equation)[28]:

$$\frac{1}{C^2} = \frac{2}{N_A \varepsilon \varepsilon_0 e A^2}\left(E - E_{fb} - \frac{kT}{e}\right)$$

where, C is the interfacial capacitance (i.e., capacitance of the semiconductor depletion layer), ε is the dielectric constant of the material, ε_0 is the permittivity of free space (8.85 x 10^{-12} Fm^{-1}), N_A is the number density (cm^{-3}) of acceptors in the semiconductor (doping level), E is the applied potential, E_{fb} is the flat band potential, T is the absolute temperature (298 K), k is the Boltzmann constant (1.38 x 10^{-23} JK^{-1}) , e is the electron charge (1.6 x 10^{-19} C) and A is the area of the electrode.

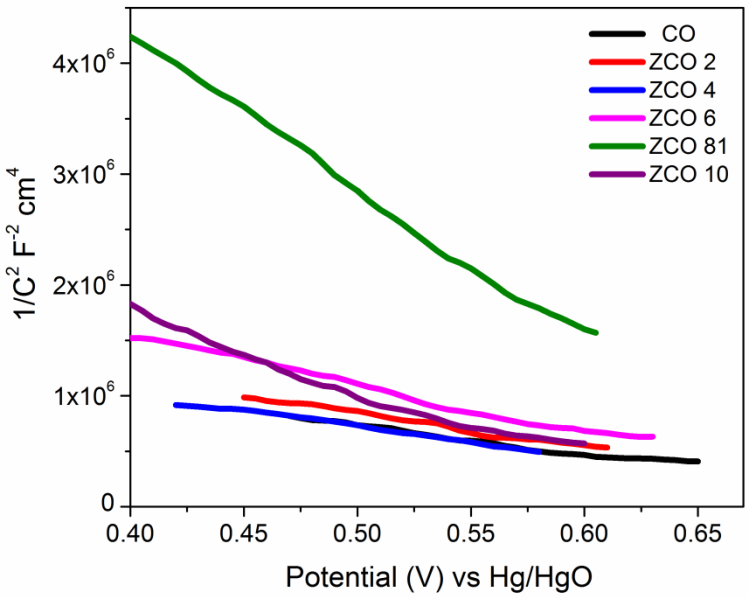

Figure 4.19 Mott-Schottky plots of $Zn_xCo_{3-x}O_4$.

Figure 4.19 shows the Mott-Schottky plots of $Zn_xCo_{3-x}O_4$. The nature of the slope of the straight lines shows that all are p-type semiconductors [27,28]. The slope is equal to

$\frac{2}{N_A \varepsilon \varepsilon_0 e A^2}$ and the carrier density (N_A) is inversely proportional to the slope. Figure 4.20 shows the variation of slope the with respect to the Zn content in $Zn_xCo_{3-x}O_4$. It shows that the slope decreases with increasing Zn content and reaches a minima when x=0.8 (i.e. ZCO 8). It implies that the carrier density (N_A) increases with respect to the Zn content and ZCO 8 has the maximum carrier density.

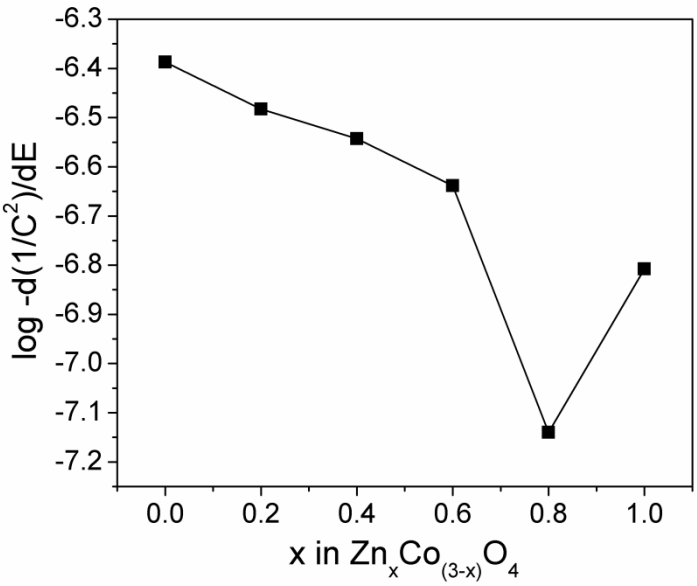

Figure 4.20 Variation of slope of the Mott-Schottky plot with Zn content in $Zn_xCo_{3-x}O_4$.

4.4.4 Quantitative oxygen evolution

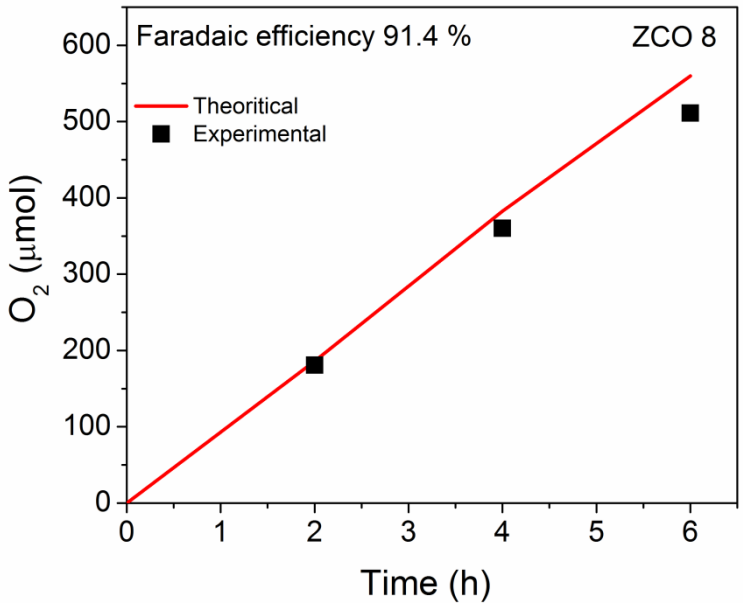

Figure 4.21 Quantitative oxygen evolution as a function of time of electrolysis using ZCO 8.

Quantitative oxygen evolution is measured using the catalyst ZCO 8 which showed the lowest overpotential. The experiment has been carried out by applying a constant current to calculate the Faradaic efficiency of the reaction. Catalyst (ZCO 8) coated on the stainless steel (SS316) mesh is used as the anode and platinum foil as the cathode. The area of the SS316 mesh is 2 cm^2 and the catalyst loading is 1 mg/cm^2.A current of 5 mA/cm^2 is applied for 6 hours, and the gas mixture is collected and analyzed using gas chromatography with an interval of 2 hours. The amount of oxygen gas evolved (µmol) is plotted with as a function of time, and it is compared with the 100 % faradic efficiency (Figure 4.21). The Faradaic efficiency of ZCO 8 is obtained as 91.4 %. The higher Faradaic efficiency confirms that the applied current is utilized only for the oxygen evolution reaction and no more side reactions occur during the measurement.

4.4.5 Roughness factor

Roughness factor is determined from the double layer capacitance measurements [29]. According to this method, cyclic voltammetry curves were recorded in the non-Faradaic region at different scan rates. It is assumed that double layer charging is the only process in

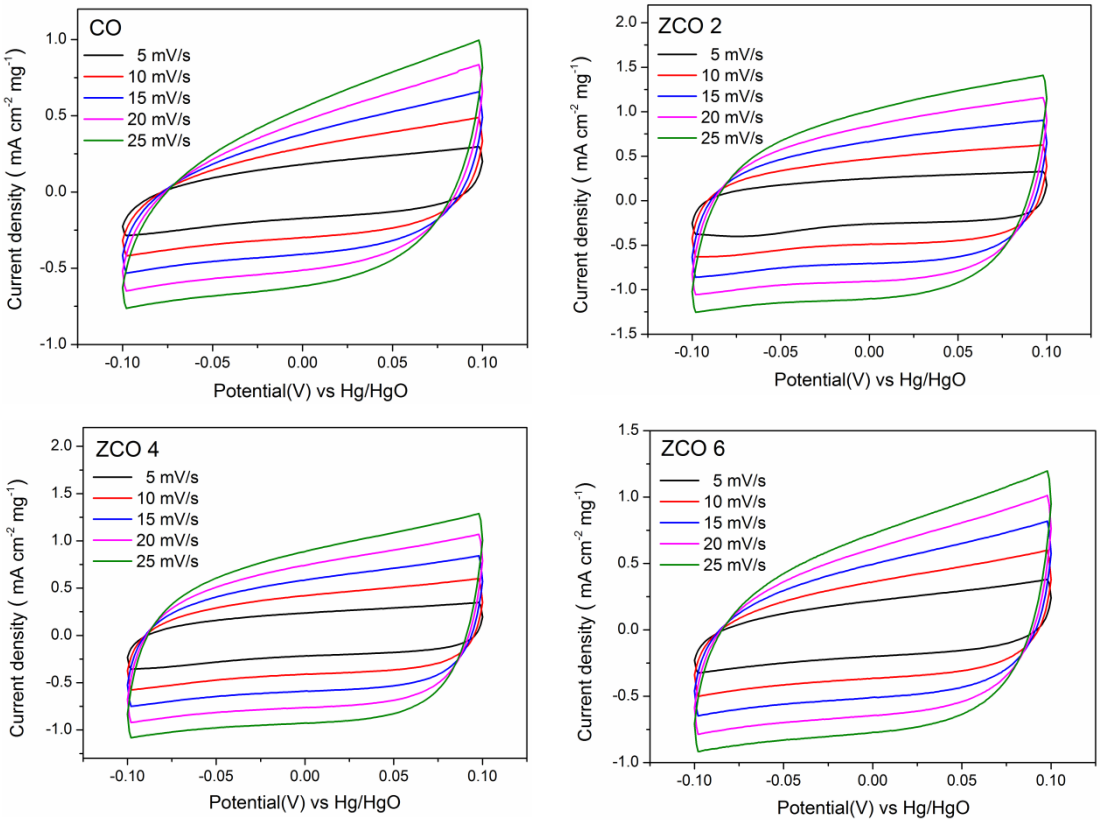

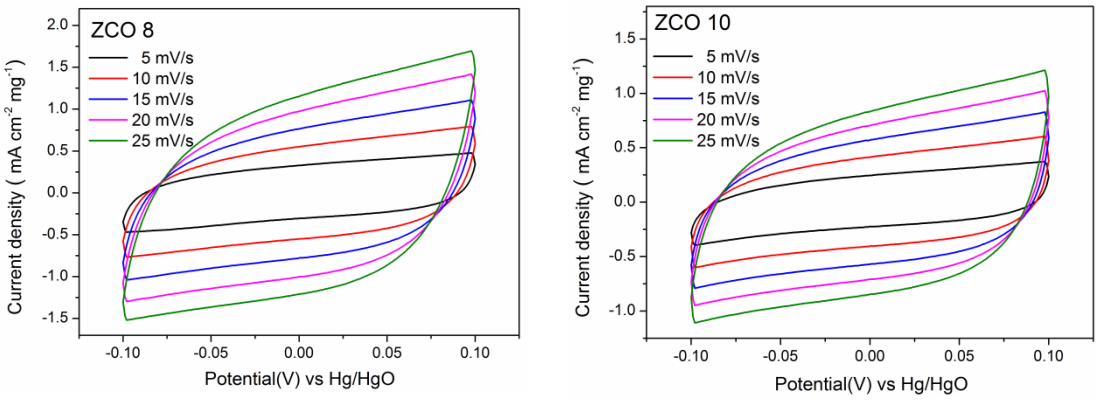

Figure 4.22 Cyclic voltammetry curves of $Zn_xCo_{3-x}O_4$ in 0.1 M KOH at different scan rates in the non-Faradic potential window (-0.1 to 0.1 V).

the potential window. Figure 4.21 shows the linear part of scan rate vs capacitive current. The slope gives the double layer capacitance, and from that, the roughness factor is calculated and tabulated. Table 4.8 shows that all the Zn substituted cobalt oxides have higher roughness factor than the unsubstituted cobalt oxide (Co_3O_4). It clearly shows the favorable nature of Zn-substitution which increases the roughness factor of cobalt oxide, particularly ZCO 8 has the highest roughness factor of 722 among the series of the samples.

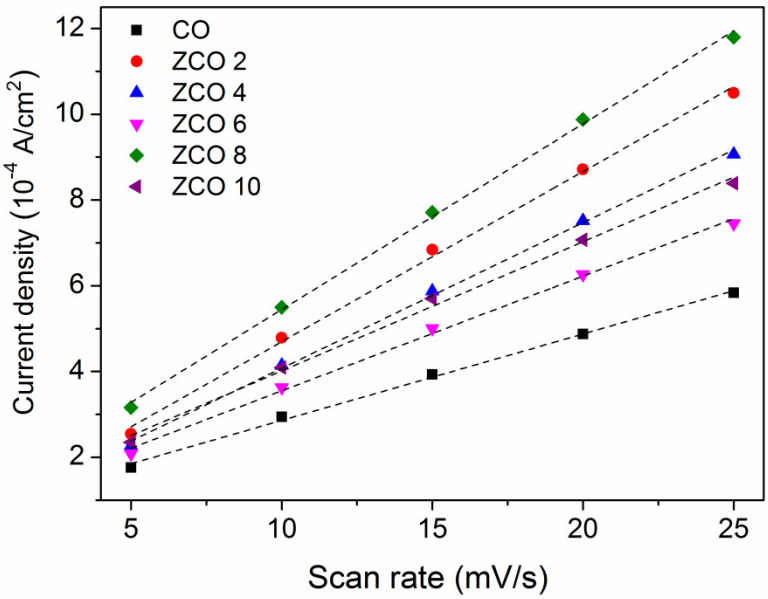

Figure 4.23 capacitive current density as a function of scan rate of $Zn_xCo_{3-x}O_4$

Table 4.8 Roughness factor of $Zn_xCo_{3-x}O_4$

Sample code	Roughness factor (R_f)
CO	337
ZCO 2	662
ZCO 4	567
ZCO 6	447
ZCO 8	722
ZCO 10	502

4.5 Correlation of electronic structure of Co with the oxygen evolution overpotential

Magnetic measurements showed that all the samples are paramagnetic. The Curie-Weiss behaviour (above 100 K) is evident from the $1/\chi$ vs T plot (Figure 4.7) and the calculated values of the Curie constant and total spin are given in Table 4.4. For CO (Co_3O_4) and ZCO 10 ($ZnCo_2O_4$) higher μ_{eff} (4.79 & 3.56 μ_B) is obtained than the μ_{eff} reported for bulk Co_3O_4 and $ZnCo_2O_4$ (4.27 and 2.79 μ_B)[11, 13, 30], which implies that some of the Co^{3+} have unpaired electrons. The results confirmed the presence of unpaired electron in the Co^{3+}. The spin contribution from the unpaired electrons from Co^{3+} increases with the degree of Zn substitution (Figure 4.9). Nevertheless, the existence of intermediate spin cannot be excluded completely as it is difficult to conclude the existence of Co^{3+} in the high-spin state only, which requires further detailed studies [31-32]. However, the existence of high-spin Co^{3+} is supported from the absorption spectral studies on $Zn_xCo_{3-x}O_4$ as shown in Figure 12. As shown in Table 5, the transition corresponds to $\sigma^* e_g^{\alpha} \rightarrow \sigma^* e_g^{\beta}$ Co is due to the presence of Co^{3+} in the high-spin state. Moreover, the area of peak 2 increases with the increasing Zn content in $Zn_xCo_{3-x}O_4$ (Figure 4.14), which matches well with the trend observed for the spin contribution from Co^{3+} with the increasing Zn content (Figure 4.9).

In principle, high-spin Co^{3+} is not stable in the cobalt oxide lattice. However, the presence of high-spin Co^{3+} may be due to crystal lattice distortion like tetragonal distortion which stabilizes the high-spin Co^{3+}. For example, in nanosized stoichiometric $LiCoO_2$, the surface Co^{3+} prefers the high-spin configuration due to the pseudotetrahedral configuration

with the oxygen atoms [33]. Similarly, in ultrathin nanosheets of Co_3S_4, the surface octahedral Co^{3+} prefers high-spin configuration due to the Jahn-Teller distortion [34]. Similarly, high-spin Co^{3+} are found at the tips of $LiCoO_2$ nanorods[36] and DFT studies showed that the surface energy of the surface planes are greatly reduced due to the conversion of the Co^{3+} spin state from low-spin to high-spin [37]. Also, in the surface of non-stoichiometric Co_3O_4 films, the presence of high-spin Co^{3+} is confirmed by the electronic absorption studies [20] .

Zn^{2+} doping in the cubic spinel lattice of cobalt oxide ($Zn_xCo_{3-x}O_4$) increases the electrocatalytic activity for the oxygen evolution reaction by lowering the overpotential as discussed earlier supported by the electrochemical measurements. The increased electrocatalytic activity of $Zn_xCo_{3-x}O_4$ can be well correlated with the change in the electronic structure of $Zn_xCo_{3-x}O_4$. Usually in spinel cobalt oxide, Co_3O_4 , octahedral Co^{3+} prefers the low-spin configuration [12]. However, the magnetic and optical absorption studies on $Zn_xCo_{3-x}O_4$ revealed that all the samples are paramagnetic and not all the Co^{3+} are in the low-spin configuration.

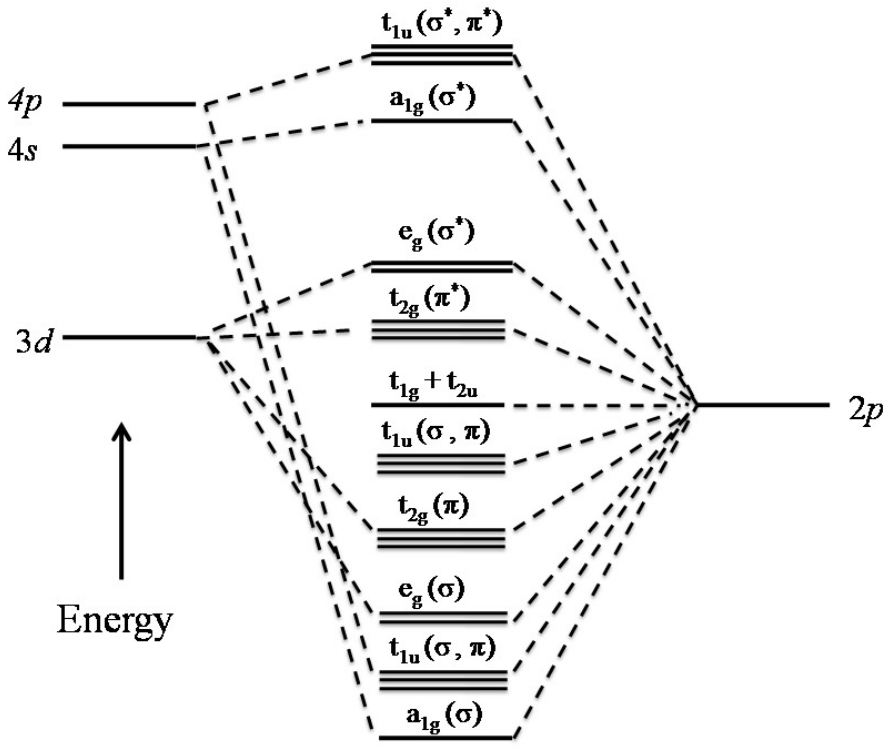

Figure 4.24 Qualitative molecular orbital diagram for octahedrally-coordinated transition metal ion (Figure adapted from [35].

Due to the presence of high-spin in Co^{3+}, the electron filling in the t_{2g} and e_g levels are different. Recently, electron filling at the e_g level is identified as one of the important descriptors for the oxygen evolution reaction [38-39]. From the crystal field perspective, octahedrally coordinated d orbital will be split into many energy levels as shown in Figure 4.24 [35]. Particularly, e_g and t_{2g} levels are very important for the catalysis, which are antibonding in nature, because, these two states are involved in the overlap with the oxygen related adsorbates and intermediates. Among the two states, e_g orbital has stronger overlap with the oxygen related adsorbate due to its sigma bonding nature than the t_{2g} orbital with the pi bonding nature [40-41].Because of these reasons, e_g orbital occupancy has become one of the important descriptors for the oxygen evolution reaction. Recently, Shan-Horn group has shown the correlation between the e_g orbital occupancy and the electrocatalytic activity for the oxygen evolution reaction. The OER activity of the perovskites increases when the e_g orbital occupancy is increasing from zero and reaches a maximum at 1.2 and further increasing of e_g orbital occupancy decreases the OER activity and forms a volcano shape plot, as shown in Figure 4.25 [38]. $Ba_{0.5}Sr_{0.5}Co_{0.8}Fe_{0.2}O_{3-\delta}$ with e_g orbital occupancy of 1.2 has shown the highest electrocatalytic activity for the oxygen evolution [38]. Depends on the e_g orbital occupancy, the rate-determining step (RDS) varies. When the e_g orbital occupancy is less than 1.2 (left side of the volcano plot), deprotonation of oxyhydroxide group to form peroxide ion is proposed as the RDS. When the e_g orbital occupancy is more than 1.2 (right side of the volcano plot), the formation of O-O bond in the OOH adsorbate on B-site ions is proposed as the RDS (Figure 4.26).

In the present study, when the Zn^{2+}content increases in $Zn_xCo_{3-x}O_4$, the population of high spin Co^{3+} increases and resulting in higher electrocatalytic activity for OER. The reason might be the increased high-spin Co^{3+} population resulting in the increase of e_g orbital occupancy of the surface Co^{3+} ions, which are active sites for the OER. Further studies are required to quantify the e_g orbital occupancy of the surface Co^{3+} ions in the spinels. As explained above, e_g orbital forms a strong overlap with the adsorbates and facilitates the electron transfer between the surface Co^{3+} and adsorbates, reaction intermediates and reduces the activation energy and improves the kinetics of the OER.

Erik Bjartnes showed a correlation between the charge carrier density and electrocatalytic activity for the OER [42]. When the Sr content in $La_{1-x}Sr_xCoO_3$ increases, the carrier density increases, thereby increasing the electrocatalytic activity for OER. In a similar way, the correlation between the charge carrier density and electrocatalytic activity has been

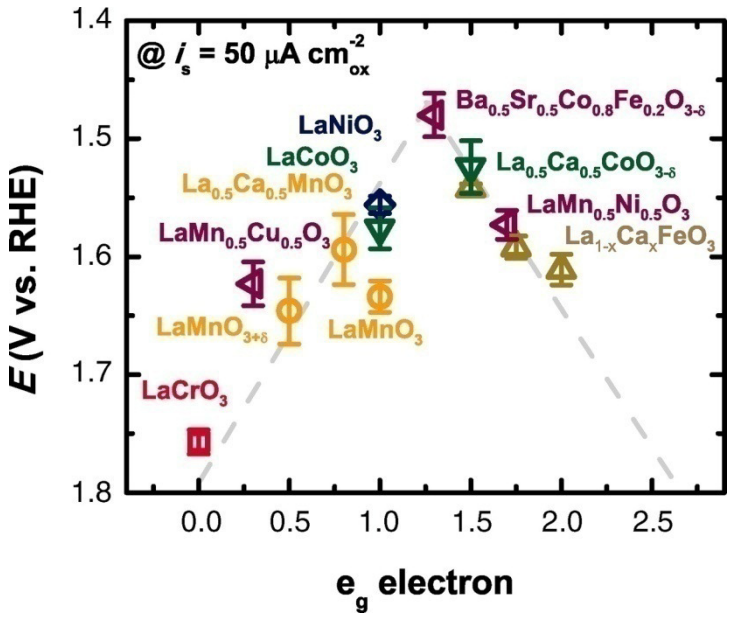

Figure 4.25 Volcano plot showing the relationship between OER catalytic activity, defined as the overpotential at 50 μA cm^{-2}(estimated true oxide surface area), and the e_g orbital occupancy of the B-site transition metal ion. (Figure adapted from [38])

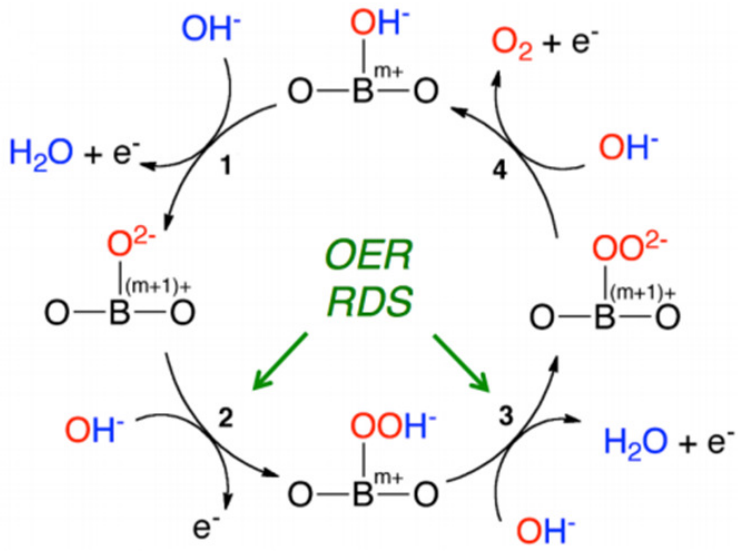

Figure 4.26 Proposed OER mechanism on perovskite oxide catalysts (Figure adapted from [38])

found for $Zn_xCo_{3-x}O_4$. Figure 4.20 shows that when the Zn^{2+} content increases in $Zn_xCo_{3-x}O_4$, the slope of the Mott-Schottky plot is decreased implying that carrier density (N_A) increases on increasing the Zn content and ZCO 8 has the maximum carrier density. Higher carrier

density provides the higher catalytic activity. This change in carrier density trend matches well with the change in the overpotential trend (Figure4.18) for the OER. Particularly, ZCO 10 has less carrier density than ZCO 8 and this is reflected in the electrocatalytic activity alsoi.e., ZCO 10 showed higher overpotential when compared to ZCO 8.

In the spinel Co_3O_4, each Co^{3+} in the octahedral site has connected to six Co^{2+} ions through oxygen (Co^{3+}-O-Co^{2+}). When the Zn^{2+} content increases in $Zn_xCo_{3-x}O_4$, Zn^{2+} replaces Co^{2+} in the tetrahedral site. Hence, the number of Co^{2+} which is connected to the Co^{3+} through oxygen is decreased. As discussed earlier, high spin Co^{3+} population plays a vital role in deciding the OER activity, the Zn^{2+} substitution shows a constant increase in the catalytic activity (CO to ZCO 8). The fully substituted composition (ZCO 10) has only Co^{3+} which exhibited a decreased OER activity as shown in Figure 4.18. This could be correlated with the breakage in Co^{3+}-O-Co^{2+} network chain with completely d orbital filled Zn^{2+}. The result suggests that some Co^{2+}-Co^{3+} connectivity is required for enhanced electrocatalytic activity. Recently, geometrical site dependent water oxidation activity on Co_3O_4 revealed that Co^{2+} in the tetrahedral position has the capability to form CoOOH under applied potential by oxidizing to higher oxidation state [43]. CoOOH is identified as the main active site for OER on Co_3O_4. The comparison of OER electrocatalytic activities of $Co_3O_4$and $ZnCo_2O_4$ by operandomethods showed that Co^{3+} in the octahedral sites tend to form a stable bond with the hydroxyl groups which limits the catalytic activity [43]. In the present study also (Figure 4.18), it is observed that replacing all the Co^{2+} by Zn^{2+} decreases the electrocatalytic activity of ZCO 10 compared to ZCO 8 and reveals the presence of a minimum amount of Co^{2+} enhances the OER electrocatalytic activity of $Zn_xCo_{3-x}O_4$.

4.6 Conclusions

Different compositions of nanostructured zinc-substituted cobalt oxide ($Zn_xCo_{3-x}O_4$) are synthesized by a simple auto-combustion method. The structural and electronic structure of $Zn_xCo_{3-x}O_4$ is studied using XRD, optical absorption, XPS and magnetic measurements which revealed the presence of high-spin Co^{3+} in the different compositions. When, the Zn content increases in $Zn_xCo_{3-x}O_4$, the spin contribution from Co^{3+} increases, which implies increased occupancy of e_g orbital of Co^{3+}. All the samples have been tested for their electrocatalytic activity for the oxygen evolution reaction. When the Zn content is increased in $Zn_xCo_{3-x}O_4$,

the overpotential for OER is decreased. This electrocatalytic activity trend is well correlated with the electronic structure of $Zn_xCo_{3-x}O_4$. Particularly, $Zn_{0.8}Co_{2.2}O_4$ showed the lowest overpotential of 254 mV (at 10 mA/cm^2) for OER, which is comparable to the values reported for precious metal oxide based catalysts. Impedance analysis revealed the correlation between the carrier density and electrocatalytic activity of $Zn_xCo_{3-x}O_4$. Higher carrier density results in higher electrocatalytic activity for OER.

References:

1. Ramsundar, R. M.; Debgupta, J.; Pillai, V. K.; Joy, P. A., *Electrocatalysis* **2015,** *6*, 331.
2. Shannon, R. D., *Acta Crystallographica Section A* **1976,** *32*, 751.
3. Sing, K. S.; Gregg, S., *Adsorption, surface area and porosity*. Academic Press, London: **1982**
4. Tan, B. J.; Klabunde, K. J.; Sherwood, P. M., *Journal of the American Chemical Society* **1991,** *113*, 855.
5. Chuang, T.; Brundle, C.; Rice, D., *Surface Science* **1976,** *59*, 413.
6. Oku, M.; Sato, Y., *Applied Surface Science* **1992,** *55*, 37.
7. Langell, M.; Anderson, M.; Carson, G.; Peng, L.; Smith, S., *Physical Review B* **1999,** *59*, 4791.
8. Liu, X.; Chang, Z.; Luo, L.; Xu, T.; Lei, X.; Liu, J.; Sun, X., *Chemistry of Materials* **2014,** *26*, 1889.
9. Grohmann, I.; Peplinski, B.; Unger, W., *Surface and Interface Analysis* **1992,** *19*, 591.
10. Cullity, B.; Graham, C., *Introduction to Magnetic Materials*. **2008**.
11. Cossee, P., *Recueil Des Travaux Chimiques Des Pays-Bas-Journal of the Royal Netherlands Chemical Society* **1956,** *75*, 1089.
12. Roth, W., *Journal of Physics and Chemistry of Solids* **1964,** *25*, 1.
13. Raveau, B.; Seikh, M., *Cobalt oxides: from crystal chemistry to physics*. John Wiley & Sons: **2012**.
14. Lever, A. B. P., *Inorganic electronic spectroscopy*. Elseveir: **1968**.
15. Lenglet, M.; Jørgensen, C. K., *Chemical Physics Letters* **1994,** *229*, 616.
16. Miedzinska, K.; Hollebone, B.; Cook, J., *Journal of Physics and Chemistry of Solids* **1987,** *48*, 649.
17. Cook, J. G.; van der Meer, M. P., *Thin Solid Films* **1986,** *144*, 165.
18. Kim, K. J.; Park, Y. R., *Solid State Communications* **2003,** *127*, 25.

19. Behzad, H.; Ghodsi, F. E., *Journal of Materials Science-Materials in Electronics* **2016,** *27*, 6096.
20. Belova, I. D.; Roginskaya, Y. E.; Shifrina, R. R.; Gagarin, S. G.; Plekhanov, Y. V.; Venevtsev, Y. N., *Solid State Communications* **1983,** *47*, 577.
21. Ohnishi, S.; Sugano, S., *Journal of Physics C-Solid State Physics* **1981,** *14*, 39.
22. Boggio, R.; Carugati, A.; Trasatti, S., *Journal of Applied Electrochemistry* **1987,** *17*, 828.
23. Švegl, F.; Orel, B.; Hutchins, M.; Kalcher, K., *Journal of the Electrochemical Society* **1996,** *143*, 1532.
24. Švegl, F.; Orel, B.; Grabec-Švegl, I.; Kaučič, V., *Electrochimica Acta* **2000,***45*, 4359.
25. Trasatti, S., *Electrochimica Acta* **1991,** *36*, 225.
26. Kim, T. W.; Woo, M. A.; Regis, M.; Choi, K.-S., *Journal of Physical Chemistry Letters* **2014,** *5*, 2370.
27. Bott, A. W., *Current Separations* **1998,** *17*, 87.
28. Bard, A. J.; Faulkner, L. R.; Leddy, J.; Zoski, C. G., *Electrochemical methods: fundamentals and applications*. Wiley New York: 1980; Vol. 2.
29. Trasatti, S.; Petrii, O., *Journal of Electroanalytical Chemistry* **1992,** *327*, 353.
30. Dutta, P.; Seehra, M. S.; Thota, S.; Kumar, J., *Journal of Physics-Condensed Matter* **2008,** *20*, 015218.
31. Zobel, C.; Kriener, M.; Bruns, D.; Baier, J.; Gruninger, M.; Lorenz, T.; Reutler, P.; Revcolevschi, A., *Physical Review B* **2002,** *66*, 020402.
32. Korotin, M. A.; Ezhov, S. Y.; Solovyev, I. I.; Anisimov, V. V.; Khomskii, D. I.; Sawatzky, G. A., *Phys Rev B Condens Matter* **1996,** *54*, 5309.
33. Qian, D.; Hinuma, Y.; Chen, H.; Du, L. S.; Carroll, K. J.; Ceder, G.; Grey, C. P.; Meng, Y. S., *Journal of the American Chemical Society* **2012,** *134*, 6096.
34. Liu, Y.; Xiao, C.; Lyu, M.; Lin, Y.; Cai, W.; Huang, P.; Tong, W.; Zou, Y.; Xie, Y., *Angewandte Chemie* **2015,** *127*, 11383.
35. Cox, P. A., *Transition metal oxides: an introduction to their electronic structure and properties.* Oxford: Carendon Press: 1992.
36. Han, B.; Qian, D.; Risch, M.; Chen, H.; Chi, M.; Meng, Y. S.; Shao-Horn, Y., *Journal of Physical Chemistry Letters* **2015,** *6*, 1357.
37. Qian, D.; Hinuma, Y.; Chen, H.; Du, L. S.; Carroll, K. J.; Ceder, G.; Grey, C. P.; Meng, Y. S., *Journal of the American Chemical Society* **2012,** *134*, 6096.

38. Suntivich, J.; May, K. J.; Gasteiger, H. A.; Goodenough, J. B.; Shao-Horn, Y., *Science* **2011,** *334*, 1383.

39. Zhou, S.; Miao, X.; Zhao, X.; Ma, C.; Qiu, Y.; Hu, Z.; Zhao, J.; Shi, L.; Zeng, J., *Nature communications* **2016,** *7*.

40. Betley, T. A.; Wu, Q.; Van Voorhis, T.; Nocera, D. G., *Inorganic Chemistry* **2008,** *47*, 1849.

41. Ballhausen, C. J.; Gray, H. B., *Inorganic Chemistry* **1962,** *1*, 111.

42. Bjartnes, E. Oxygen evolution on La_{1-x} Sr $_x$ CoO_3 Pellet-Electrodes in alkaline Solution: Charge Carrier density dependence of electrocatalytic activity. Mater's thesis, Institutt for materialteknologi, 2012.

43. Wang, H. Y.; Hung, S. F.; Chen, H. Y.; Chan, T. S.; Chen, H. M.; Liu, B., *Journal of the American Chemical Society* **2016,** *138*, 36.

Chapter 5

Role of Co^{3+} in Co_3O_4 on the electrochemical oxygen evolution

5.1 Introduction

In the previous chapter, the effect of Zn^{2+} substitution for Co^{2+} in Co_3O_4 on the electrocatalytic activity for the oxygen evolution reaction (OER) was studied. To study the role of Co^{3+} in Co_3O_4, Co^{3+} is partially replaced by $Al^{3+}$and the electrocatalytic properties of the resulting compositions for OER is studied in this chapter. Al^{3+} is one of the ideal choices for the replacement of Co^{3+}, because, the ionic radius of Al^{3+} (0.535 Å for hexa coordinated) closely matches with that of Co^{3+} (0.545 Å for hexa coordinated) [1]. In Al-substituted spinel compositions, Al preferentially occupies the octahedral site. Similar to the parent compound, Co_3O_4, identical conditions are followed during the synthesis of Al-substituted Co_3O_4 to achieve a meaningful comparison. To achieve detailed information on the role of Co^{3+}, a systematic variation of Al has been followed, represented by the formula $Co_{3-x}Al_xO_4$ where x = 0.5, 1.0, 1.5 and 2. All materials are characterized using various techniques such as XRD, BET, TEM, magnetic and electrocatalytic measurements for understanding of the characteristic properties and to correlate the OER activity to identify the best possible catalytic formulation.

5.2 Synthesis

Autocombustion method is adapted for the preparation of Al-substituted cobalt oxide, and more detailed information on the synthetic methodology is described in Chapter 2. Briefly, to a mixed solution of stoichiometric amounts of aluminium nitrate ($Al(NO_3)_3.9H_2O$) and cobalt nitrate ($Co(NO_3)_2.6H_2O$) dissolved separately in a minimum amount of distilled water was mixed with a solution of glycine dissolved in minimum amount of distilled water and stirred vigorously to obtain a uniform solution.The mixed solution was evaporated slowly at 200 ºC, on a hot plate, to initiate the autocombustion reaction in a controlled manner. After the evaporation of water, the resulting thick mass burnt spontaneously to obtain a fluffy powder mass of cobalt aluminium oxide. More detailed information such as composition, the mole ratio of metal ion(s) to glycine used and the respective sample code are given in Table 5.1. 0.15 moles of glycine per mole of the metal ion is the lowest possible fuel needed for the synthesis of Co_3O_4.The same glycine ratio is used for the synthesis of all compositions in $Co_{3-x}Al_xO_4$ (x= 0.5, 1, 1.5 and 2).

All the obtained powders after the combustion reaction are found to be amorphous in nature. Therefore, all the as-prepared powder samples are calcined at 400 ºC, in air, for 3 hrs. The

resulting calcined powders have been used for all the characterizations and electrochemical testing.

Table 5.1.Sample codes, compositions and mole ratio of metal ions

Sample code	Composition	Mole ratio of $Al(NO_3)_2.9H_2O$	Mole ratio of $Co(NO_3)_2.6H_2O$
CO	Co_3O_4	0	3
CAO-1	$Co_{2.5}Al_{0.5}O_4$	0.5	2.5
CAO-2	$Co_{2.0}Al_{1.0}O_4$	1	2
CAO-3	$Co_{1.5}Al_{1.5}O_4$	1.5	1.5
CAO-4	$CoAl_2O_4$	1	2

5.3 Characterization

5.3.1 X-ray diffraction

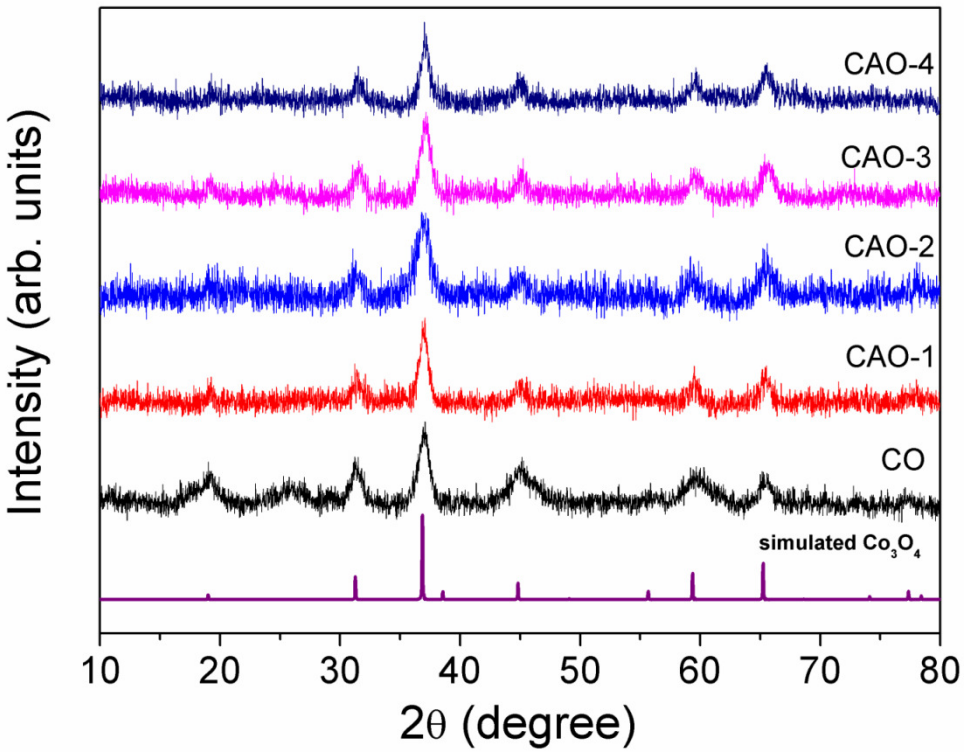

Figure 5.1 XRD patterns of the different Al-substituted Co_3O_4 compositions, compared with the simulated pattern of Co_3O_4

Figure 5.1 shows the powder XRD patterns of the calcined powders of cobalt oxide (CO) and the aluminium substituted cobalt oxides (CAO-1 to CAO-4). The experimental patterns are compared with the simulated pattern of Co_3O_4. The powder pattern is simulated using the space group Fd3m and the corresponding lattice parameter a = 8.0840 Å. All the experimental patterns match very well with the simulated one and clearly confirming the formation of spinel phase. The lattice parameter is obtained by least squares fitting of the XRD patterns, and the values are given in Table 5.2. The average crystallite size is calculated from the full width at half maximum (FWHM) of the major peak (311) using the Scherrer formula (section 2.3.1, chapter 2), and the values are given in Table 5.2.

Table 5.2 Lattice parameter and crystallite size of $Co_{3-x}Al_xO_4$

Sample code	**Lattice parameter a (Å)**	**Crystallite size (nm)**
CO	8.08	7
CAO-1	8.08	11
CAO-2	8.07	7
CAO-3	8.07	10
CAO-4	8.08	11

5.3.2 TEM studies

Figure 5.2 shows the TEM images of calcined $Co_{3-x}Al_xO_4$. All the samples show the presence of spherical particles agglomerated to small clusters. It is evident from the images that all the particles are approximately 7-11 nm in size. Substitution of Al in Co_3O_4 does not change the morphology and particle size. Hence, it may be expected that the resulting electrocatalytic activities can be purely from electronic and/or other structural and intrinsic properties of the specific composition.

5.3.3 Surface area

Figure 5.3 shows the nitrogen adsorption-desorption studies of $Co_{3-x}Al_xO_4$. The nature of the hysteresis loop confirms type IV isotherm, and it is a characteristic behavior for the mesoporous materials [2]. The BET surface area of all the samples is tabulated in Table 5.3. When Al^{3+} is introduced in Co_3O_4, the surface area decreases and CAO-3 has relatively higher surface area than the other samples. This irregularity may be due to the Al^{3+} distribution in the both the tetrahedral and octahedral sites.

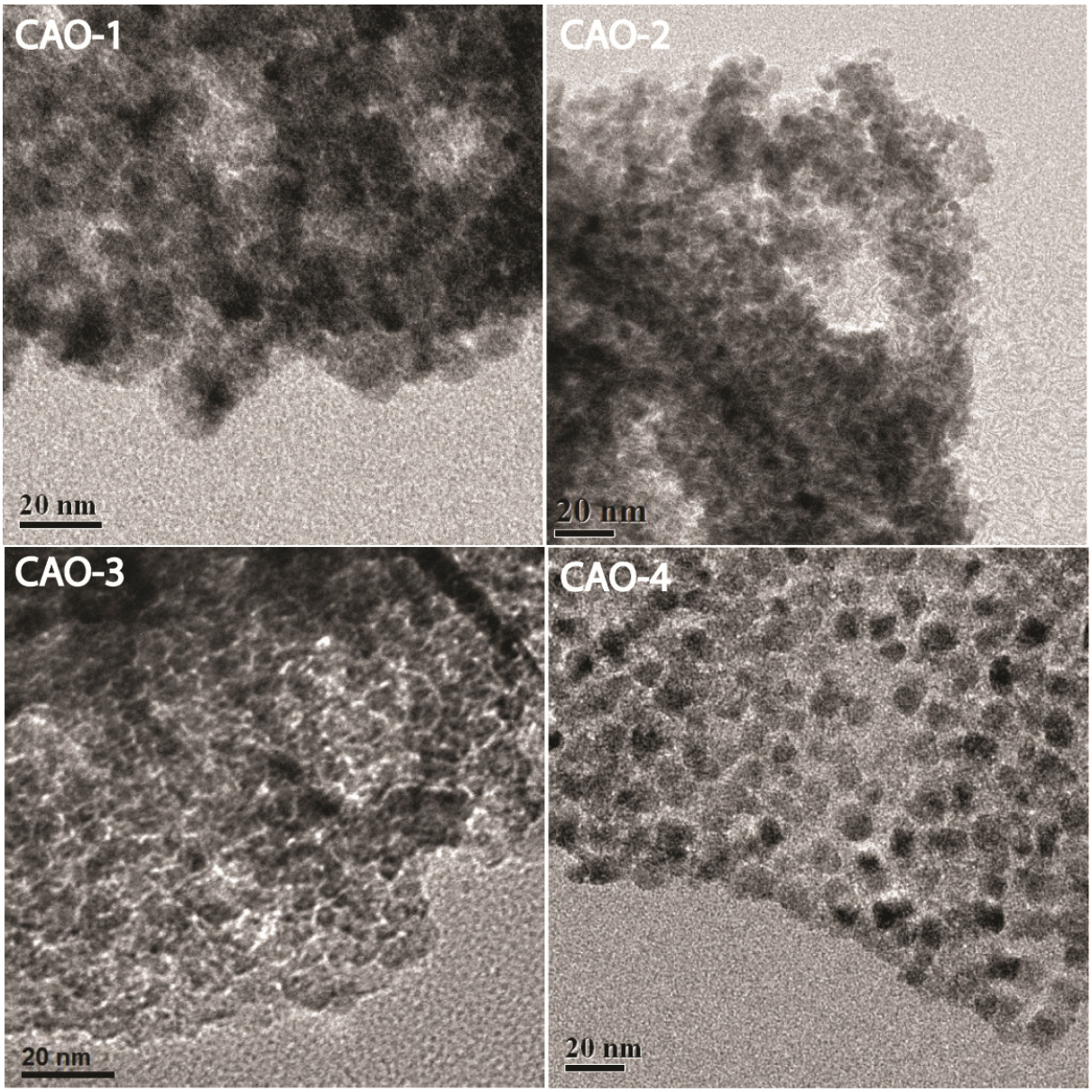

Figure 5.2 TEM images of different compositions in $Co_{3-x}Al_xO_4$

Table 5.3 BET surface area of $Co_{3-x}Al_xO_4$

Sample code	BET surface area (m^2/g)
CO	70
CAO-1	52
CAO-3	85
CAO-4	45

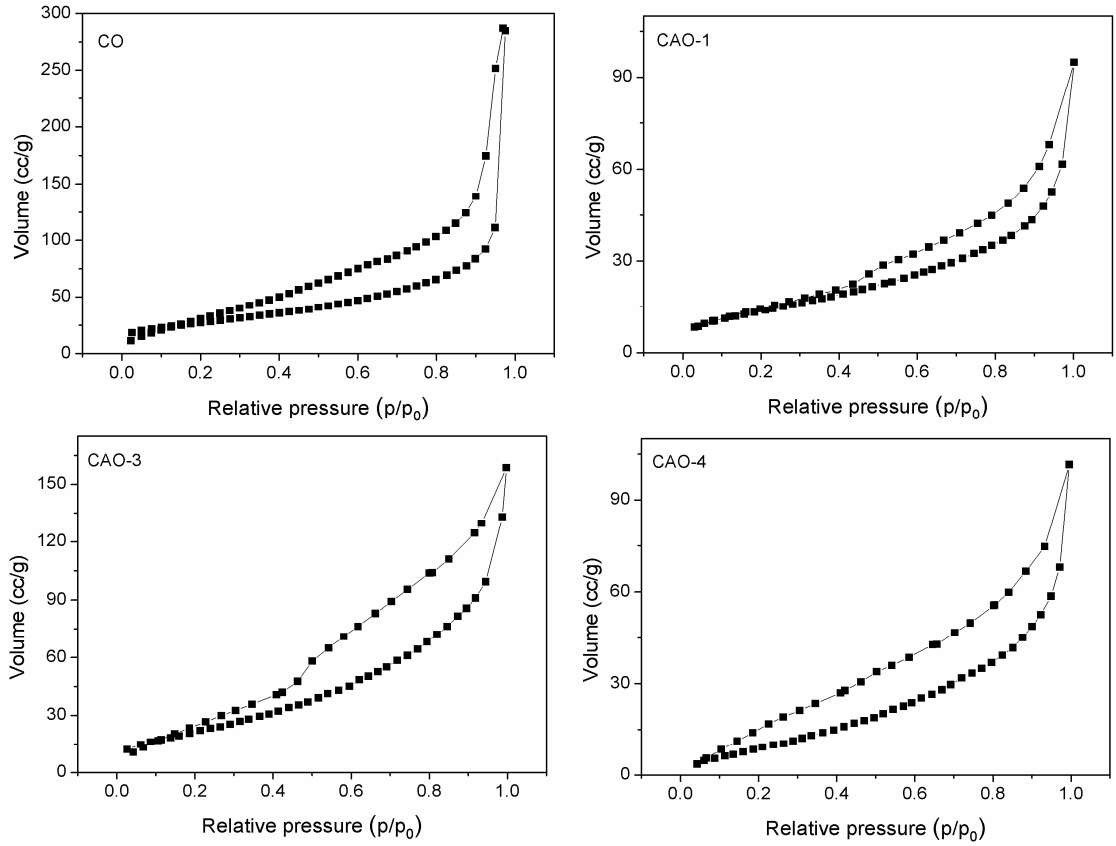

Figure 5.3 Nitrogen adsorption-desorption curves of $Co_{3-x}Al_xO_4$.

5.3.4 X-Ray photoelectron spectroscopy

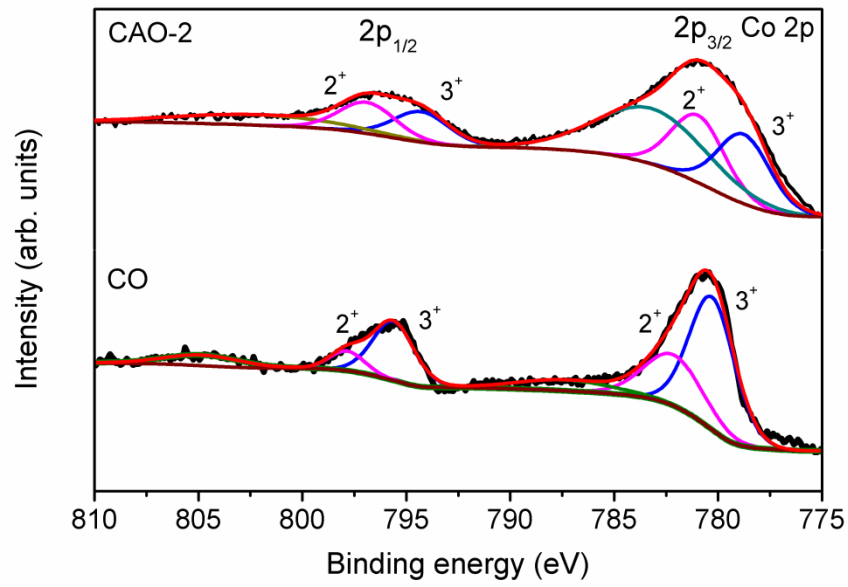

Figure 5.4 Co 2p XPS spectra of CO and CAO-2.

X-ray photoelectron spectroscopy (XPS) studies have been carried out to get information on the oxidation states of Co in Co_3O_4, and Al substituted cobalt oxide (CAO-2). In general, upon changes in the oxidation state, changes in the XPS binding energy (BE) can be expected from their chemical effects. Figure 5.4 shows the XPS spectra of cobalt oxide (CO) and Al-substituted cobalt oxide (CAO-2). Co $2p_{3/2}$ and Co $2p_{1/2}$ peaks of CAO-2 is broader compared to that of CO. Also, CAO-2 Co $2p_{3/2}$ peak position is slightly shifted to higher binding energy (781 eV) compared to the Co $2p_{3/2}$ peak position of CO (780.7 eV) [3-5]. The Co 2p spectra are fitted to get information on the Co^{2+} and Co^{3+} content in the different samples. Table 5.4 shows the Co^{2+}/Co^{3+} ratio calculated by integrating the area under the individual fitted curves of the XPS spectra. It shows that Co^{2+}/Co^{3+} ratio increases with the introduction of Al^{3+} in cobalt oxide. The ratio of Co^{2+} /Co^{3+} in CAO-2 indicates that Al^{3+} is replacing Co^{3+} in Co_3O_4.

Table 5.4 Comparison of the ratios of Co^{2+}/Co^{3+} obtained from the XPS spectra

Sample name	Co^{2+} /Co^{3+} ratio from XPS	Expected ratio
CO (Co_3O_4)	0.49	0.5
CAO-2($AlCo_2O_4$)	0.98	1.0

5.3.5 Magnetic susceptibility

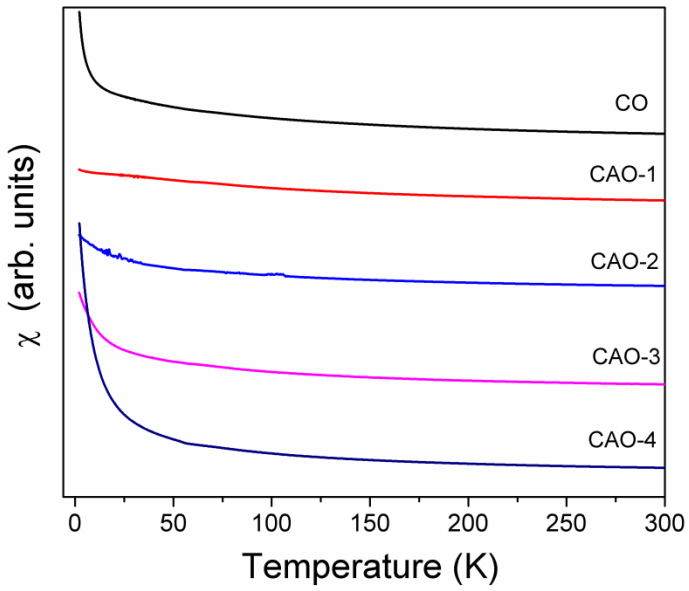

Figure 5.5 DC magnetic susceptibility curves of $Co_{3-x}Al_xO_4$.

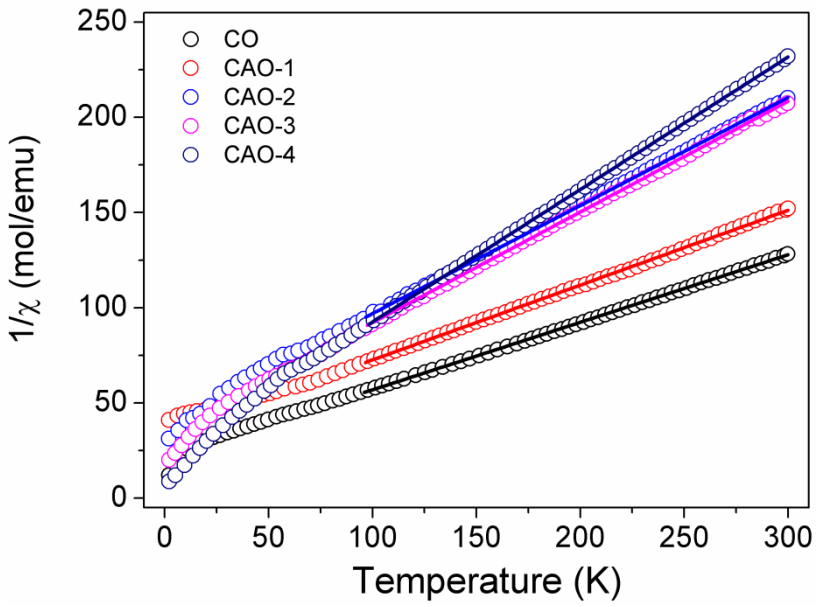

Figure 5.6 The temperature dependence of the inverse susceptibilities of $Co_{3-x}Al_xO_4$.

Figure 5.5 shows DC susceptibility of the as prepared Al-substituted Co_3O_4 measured in an applied magnetic field of 1 T, as a function of temperature. The magnetic measurement clearly indicates the paramagnetic behavior of all the samples. Figure 5.6 shows the $1/\chi$ vs. T curves and above 100 K which show a linear behaviour and follows the Curie-Weiss law [6]. The inverse slope of the straight line is the Curie constant. The total spin is calculated from the Curie constant and plotted in Figure 5.7, and it decreases with the increasing Al content in $Co_{3-x}Al_xO_4$. This is due to the replacement of paramagnetic Co^{3+} by diamagnetic Al^{3+}. Ideally, in Co_3O_4, Co^{3+} should be in the low-spin state and the total magnetic moment is mainly coming from the three unpaired electrons in the Co^{2+} [7-9]. However, CO and CAO-1 has an extra spin contribution from Co^{3+} (0.44 and 0.31 respectively), due to its intermediate spin state. CAO-2 and CAO-3 show spin values comparable or less than the contribution of Co^{2+} alone (S=1.5), suggesting the presence of only low-spin Co^{3+} (Table 5.5).

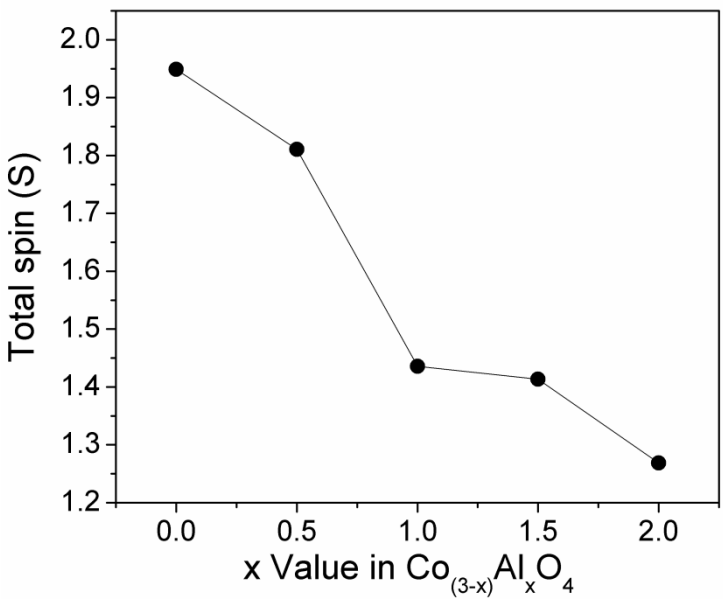

Figure 5.7 Calculated total spin values of $Co_{3-x}Al_xO_4$

Table 5.5 Curie constant and spin values of $Co_{3-x}Al_xO_4$ from the magnetic studies.

Sample code	Curie constant (emu K mol^{-1})	Total spin
CO	2.87	1.94
CAO-1	2.54	1.81
CAO-2	1.75	1.44
CAO-3	1.71	1.41
CAO-4	1.44	1.27

5.4 Electrochemical oxygen evolution

5.4.1 Cyclic voltammetry

Figure 5.8 shows the cyclic voltammograms of $Co_{3-x}Al_xO_4$ in 0.1 M KOH. All the samples show similar characteristic redox behavior of Co_3O_4. All the voltammograms exhibit one anodic peak (A) and one cathodic peak (C). Anodic peak (A) corresponds to the oxidation of Co^{3+} to Co^{4+}, and the cathodic peak (C) corresponds to the reduction of Co^{4+} to Co^{3+}. In addition to that, an anodic redox peak is observed at 0.4 V (vs. Hg/HgO) in CO and CAO-1, which corresponds to the oxidation of Co^{2+} to Co^{3+}.

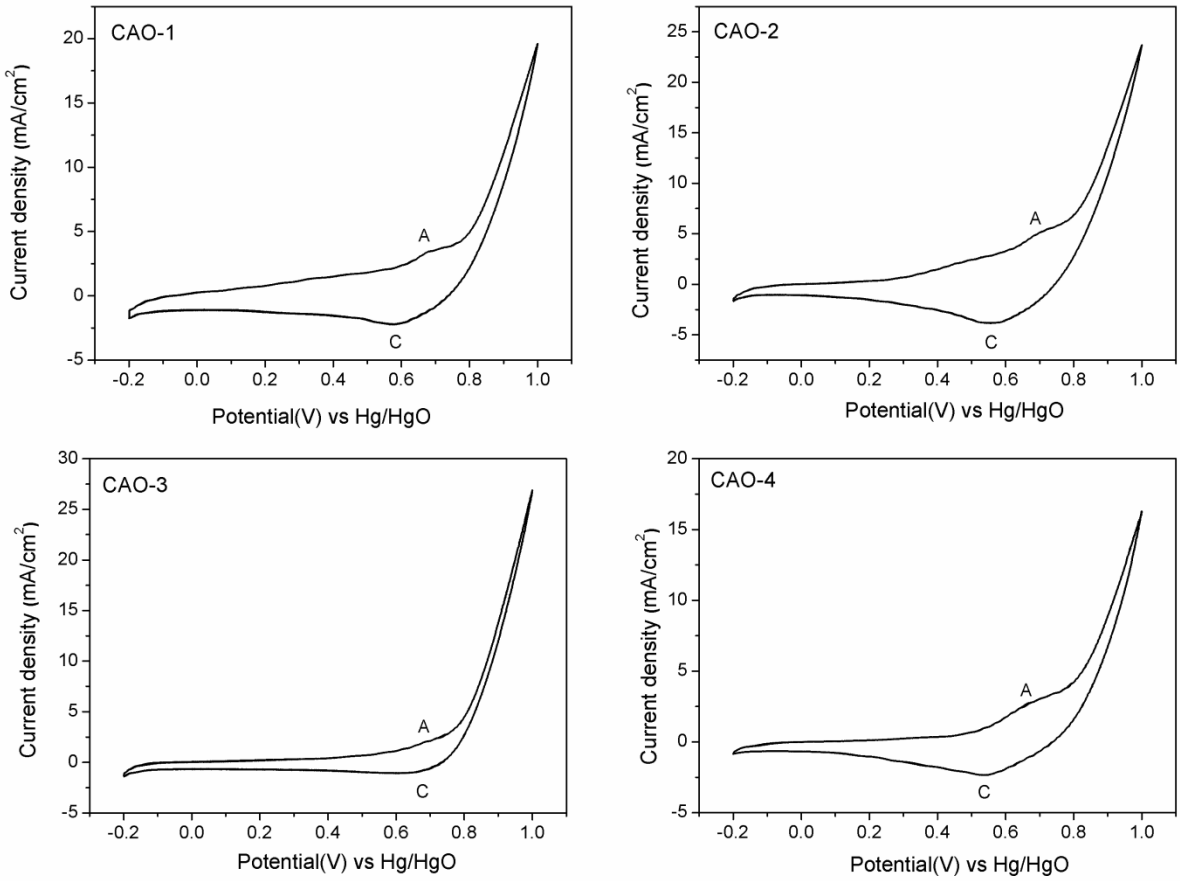

Figure 5.8 Cyclic voltammetry curves of $Co_{3-x}Al_xO_4$in 0.1 M KOH at the scan rate of 100 mV/s.

5.4.2 Tafel plots

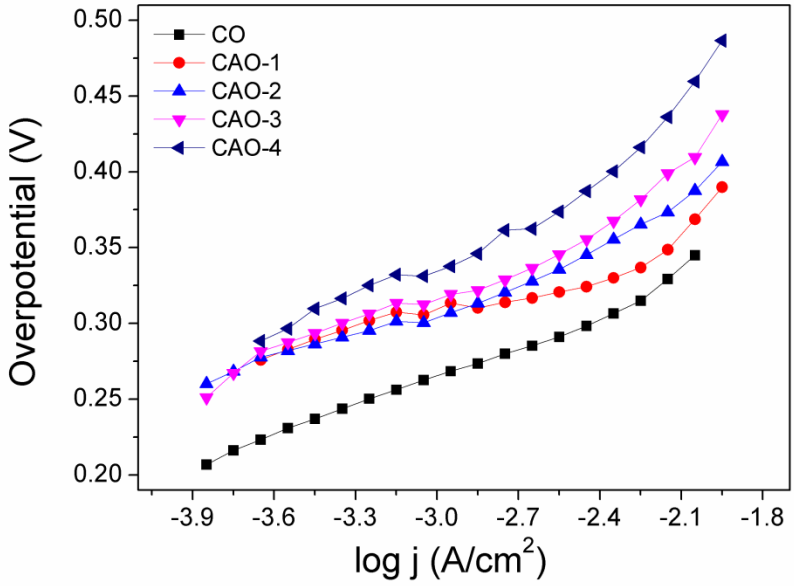

Figure 5.9 Tafel plots of $Co_{3-x}Al_xO_4$.

Tafel plot is a good tool to study the slow kinetics reactions like OER. The plot of overpotential (η) vs. log (current density (j)) generates the Tafel plot. It gives detailed information about the kinetic parameters such as overpotential, Tafel slope and exchange current density. All the samples in $Co_{3-x}Al_xO_4$ show Tafel behavior in the given current density region (Figure 5.9). The extracted kinetic parameters like overpotential, Tafel slope, and exchange current density are given in Table 5.6. As the Al content increases in the $Co_{3-x}Al_xO_4$, Tafel slope increases from 62 to 149 mV. Higher Tafel slope implies the instability of the catalyst at the experimental conditions. This shows that the introduction of Al^{3+} in Co_3O_4 is not favorable for the OER. Similarly, the increment of Al content in $Co_{3-x}Al_xO_4$ also increases the overpotential exponentially (Figure 5.10), which also implies that introduction of Al^{3+} in Co_3O_4 impedes the kinetics of OER.

Table 5.6 Overpotential, Tafel slope and exchange current density parameters from Tafel plots of $Co_{3-x}Al_xO_4$.

Sample code	Overpotential(η) at 10 mA/cm^2 (mV)	Tafel slope (mV)	Exchange current density (A/cm^2)
CO	358	62	5.20×10^{-8}
CAO-1	371	33	1.38×10^{-12}
CAO-2	392	82	2.20×10^{-6}
CAO-3	423	99	8.34×10^{-7}
CAO-4	487	149	7.80×10^{-6}

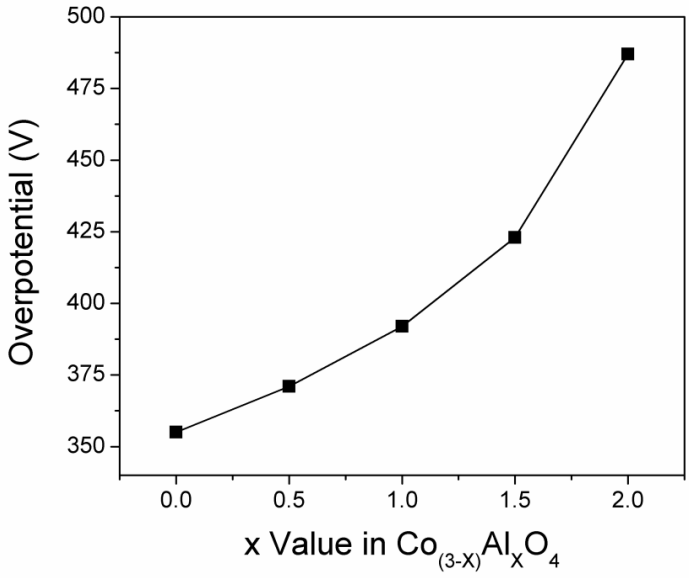

Figure 5.10 Variation of overpotential with Al content in $Co_{3-x}Al_xO_4$.

5.4.3 Roughness factor

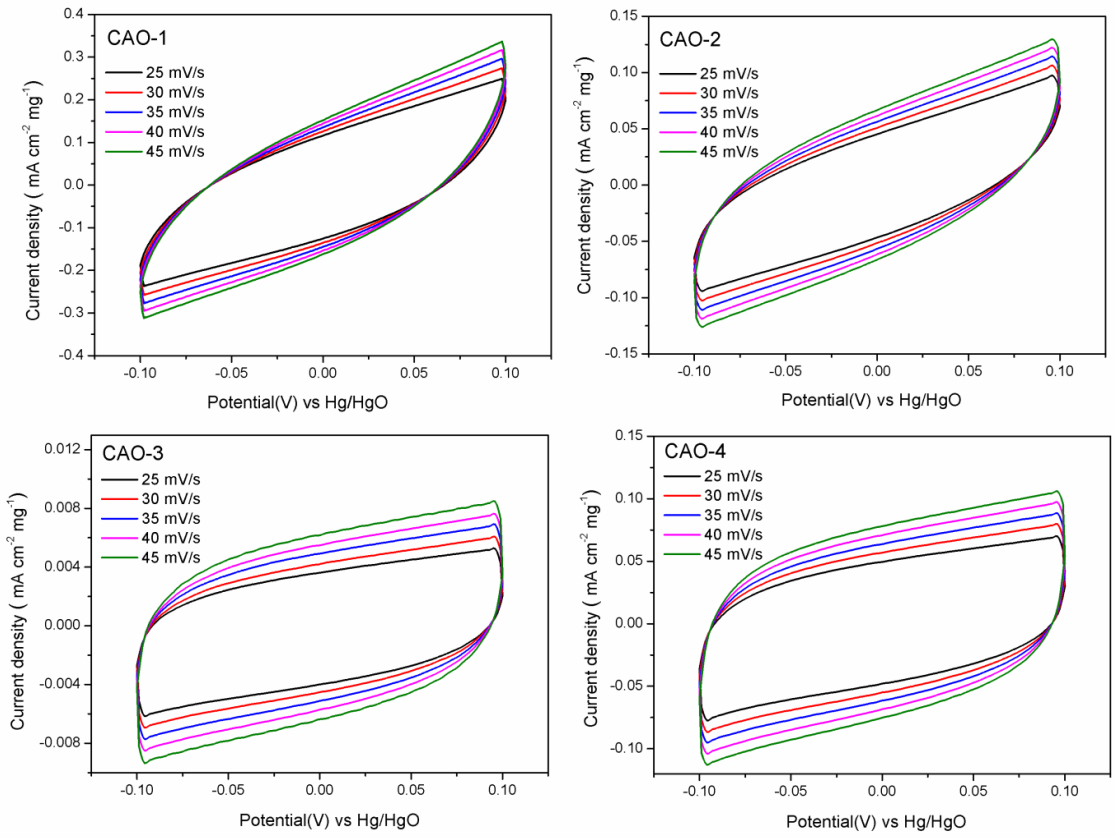

Figure 5.11 Cyclic voltammetry curves of $Co_{3-x}Al_xO_4$ in 0.1 M KOH at different scan rates in the non-faradic potential window (-0.1 to 0.1 V).

Roughness factor is determined from the double layer capacitance measurements [10]. According to this method, cyclic voltammetry curves are recorded in the non-Faradaic region at different scan rates. It is assumed that double layer charging is the only process in the potential window. Figure 5.11 shows the cyclic voltammograms of $Co_{3-x}Al_xO_4$ at the different scan rates in the non-Faradaic potential window. Figure 5.12 shows the linear part of the capacitive current vs. scan rate. The slope gives the double layer capacitance, and from that, the roughness factor is calculated and tabulated (Table 5.7). The calculated roughness factors of $Co_{3-x}Al_xO_4$ are compared in Table 5.7 and it shows that all the Al-substituted cobalt oxides have lower roughness factor than that for the unsubstituted cobalt oxide (Co_3O_4).

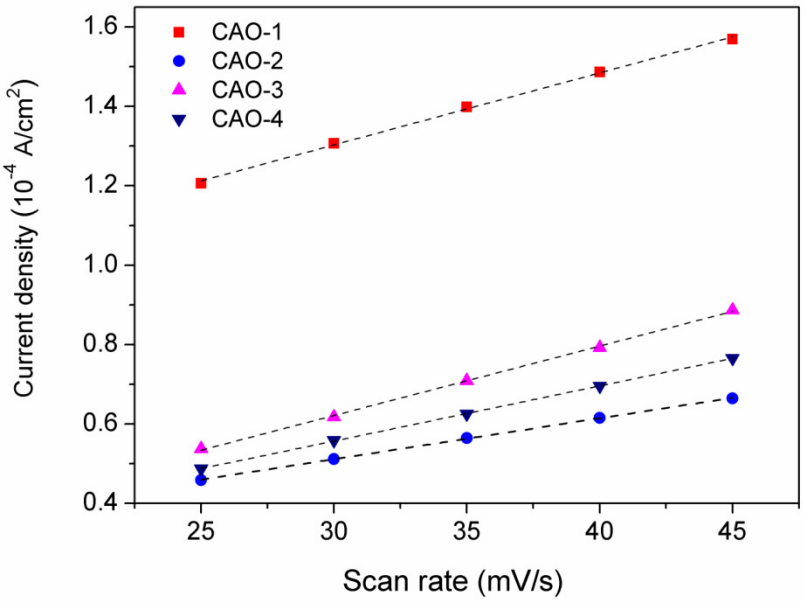

Figure 5.12 Capacitive current density as a function of scan rate for different compositions in $Co_{3-x}Al_xO_4$.

Table 5.7 Roughness factor of $Co_{3-x}Al_xO_4$.

Sample code	Roughness factor (R_f)
CO	337
CAO-1	30
CAO-2	17
CAO-3	29
CAO-4	23

5.5 Role of Co^{3+} in the electrocatalytic oxygen evolution of $Co_{3-x}Al_xO_4$

All the compositions of nanostructured $Co_{3-x}Al_xO_4$ exhibits similar spherical morphology and the sizes in the range of 7-11 nm. Therefore, the effect of size and morphology on the electrocatalytic activities can be neglected. XPS studies showed that the substitution of Al^{3+} successfully replaces the Co^{3+} in the spinel cobalt oxide. Magnetic studies revealed that Al^{3+}replaced the paramagnetic intermediate-spin Co^{3+} in Co_3O_4. Cyclic voltammetry studies showed that the non-capacitive nature might be due to the introduction of electrochemically inactive Al^{3+}. The observed anodic and cathodic redox peaks are assigned to the oxidation of Co^{3+} to Co^{4+} and the reduction of Co^{4+} to Co^{3+}, respectively.Also, the roughness factor is

greatly reduced when the Al content is increased in the spinel cobalt oxide. This is because Co^{3+} in the octahedral sites is responsible for the surface double layer capacitance. When the pseudocapacitive Co^{3+} is replaced by the redox inactive Al^{3+}, the double layer capacitance is decreased.

Recent *in situ* spectroscopic studies on cobalt oxides revealed some important information about the mechanism and active site for the OER [11-14]. The formation of μ-OO peroxide (Co-OO-Co) moieties was identified before the rising of the catalytic current in cobalt oxides [13]. Particularly, the μ-OO peroxide stretching band is obtained at higher bias for $CoAl_2O_4$ than for Co_3O_4 from *in situ* Raman spectroscopy studies. Higher potential required for the formation of μ-OO peroxide moiety in $CoAl_2O_4$couldbe correlated to the population or the proximity of cobalt atoms on the surface of the catalyst. *In situ* Fourier-transform infrared spectroscopic studies on water oxidation using cobalt oxide showed that the reaction rate is very fast when adjacent cobalt atoms are available, whereas on the isolated cobalt atom the reaction rate is very slow [11].

In the present study, galvanostatic Tafel polarization plots showed linear Tafel lines for $Co_{3-x}Al_xO_4$. It is found that that the introduction of Al in cobalt oxide increases the overpotential (at 10 mA/cm^2) for OER exponentially from 358 mV to 487 mV. It shows that the introduction of Al hinders the electrocatalytic activity of cobalt oxide by decreasing the population of octahedral Co^{3+}, which is believed as the active site for the OER. Moreover, the Tafel slope also increased from 62 mV to 149 mV with the increasing amount of Al in $Co_{3-x}Al_xO_4$. Since the population Co^{3+} is reduced with the increasing Al content, the distance between two cobalt atoms is increasing. The proximity of the cobalt atoms at the catalyst surface provides the better electrocatalytic activity with the fast kinetics [11]. If the distance between the cobalt atoms increases due to the reduced population of cobalt, then a different mechanism, having a higher kinetic barrier, is followed. It results in the higher overpotential and higher Tafel slope. Higher Tafel slope implies less stability of the catalyst at the reaction condition.

Thus, the presence of Co^{3+} in cobalt oxides for the oxygen evolution reaction is inevitable and plays a major role in the mechanism of oxygen evolution. The presence of Co^{3+} in the cobalt oxides provides a reaction path with faster kinetics for the OER with a lower overpotential and lower Tafel slope.

5.6 Conclusions

Nanostructured $Co_{3-x}Al_xO_4$ has been synthesized by a simple autocombustion method. The different compositions are characterized by XRD, TEM and magnetic measurements. When the Al content in $Co_{3-x}Al_xO_4$ is increased, the electrocatalytic activity for OER is decreased. When both Co^{3+} in Co_3O_4 is replaced by Al^{3+} (x=2), the electrocatalytic activity is decreased greatly, and the composition (CAO-4) showed the highest overpotential and higher Tafel slope. Thus, from the present studies, it is concluded that the population of Co^{3+} in $Co_{3-x}Al_xO_4$ directly affects the OER electrocatalytic activity. This implies the importance of Co^{3+} in Co_3O_4 for the oxygen evolution reaction.

References:

1. Shannon, R. D., *Acta Crystallographica Section A* **1976,** *32*, 751.
2. Sing, K. S.; Gregg, S., *Adsorption, surface area and porosity*, Academic Press, London **1982**.
3. Chin, R. L.; Hercules, D. M., *Journal of Physical Chemistry* **1982,** *86*, 360.
4. Oliveira, H. A.; Franceschini, D. F.; Passos, F. B., *Journal of the Brazilian Chemical Society* **2014,** *25*, 2339.
5. Xu, L.; Zhang, J.; Wang, F.; Yuan, K.; Wang, L.; Wu, K.; Xu, G.; Chen, W., *RSC Advances.* **2015,** *5*, 48256.
6. Cullity, B.; Graham, C., *Introduction to Magnetic Materials*. 2008.
7. Cossee, P., *Recueil Des Travaux Chimiques Des Pays-Bas-Journal of the Royal Netherlands Chemical Society* **1956,** *75*, 1089.
8. Roth, W., *Journal of Physics and Chemistry of Solids* **1964,** *25*, 1.
9. Raveau, B.; Seikh, M., *Cobalt oxides: from crystal chemistry to physics*. John Wiley & Sons: 2012.
10. Trasatti, S.; Petrii, O., *Journal of Electroanalytical Chemistry* **1992,** *327*, 353.
11. Zhang, M.; de Respinis, M.; Frei, H., *Nature chemistry* **2014,** *6*, 362.
12. Wang, H. Y.; Hung, S. F.; Chen, H. Y.; Chan, T. S.; Chen, H. M.; Liu, B., *Journal of American chemical scciety* **2016,** *138*, 36.
13. Wang, H.-Y.; Hung, S.-F.; Hsu, Y.-Y.; Zhang, L.; Miao, J.; Chan, T.-S.; Xiong, Q.; Liu, B., *The Journal of Physical Chemistry Letters* **2016,** *7*, 4847.
14. Frei, H., *Current Opinion in Chemical Engineering* **2016,** *12*, 91.

Chapter 6

Spinel type lithium cobalt oxides for electrochemical oxygen evolution

6.1 Introduction

Spinel Co_3O_4 with mixed valent nature of cobalt ions is identified as one of the potential electrocatalyst for oxygen evolution reaction. The role of Co^{2+} and Co^{3+} for the oxygen evolution reaction has been studied by partially replacing Co^{2+} and Co^{3+} by Zn^{2+} and Al^{3+}, respectively, as reported in the previous chapters. The oxidation state of cobalt and the associated electronic structure are found to play very important role in the catalytic activity for the oxygen evolution reaction. Hence, changing the oxidation state of cobalt in the cobalt oxide without affecting its structure, by proper substitution, and correlation with the electrocatalytic activity would be very much interesting. Thus, it would be interesting to study spinel-type cobalt oxides containing only Co^{3+}. Similarly, oxidation of Co^{3+} produces Co^{4+} and the $Co^{3+/4+}$ redox couple would be very important for electrocatalytic activities.

Spinel-type lithium cobalt oxides received much attention, recently, due to their structure, electrical conductivity and electrocatalytic activities. Lithium substitution in Co_3O_4 is known to increase the electrocatalytic activity with the better electrical conductivity [1-2]. Metal oxides containing lithium are well known for their use as cathode materials in Li-ion batteries [3]. One of such material is $LiCoO_2$ [4]. $LiCoO_2$ has two crystalline polymorphs. $LiCoO_2$ synthesized at higher temperatures (~800 ºC) has the α-$NaFeO_2$ structure (space group $R\bar{3}m$), in which Li^+ and Co^{3+} occupies the alternative (111) planes in the rock salt structure. $LiCoO_2$ synthesized at lower temperatures (~400 ºC) crystallizes in the spinel structure (space group *Fd3m*), in which Li^+ occupies the tetrahedral sites and Co^{3+} occupies the octahedral sites. Spinel like $LiCoO_2$ (space group *Fd3m*) contains the Co_4O_4 cubane and recently it has been found to be catalytic active in OER [24], whereas rhombohedral $LiCoO_2$ (space group $R\bar{3}m$) is inactive. Delithiation of $LiCoO_2$ induces Co^{4+}, which has interesting electrochemical properties. Studies on lithium cobalt oxides ($Li_{0.5}Co_{2.5}O_4$, spinel type $LiCoO_2$ and delithiated $LiCoO_2$) for their electrocatalytic activity for the OER are reported in this chapter. The electrocatalytic property is studied with respect to the oxidation state by controlling the oxidation state of cobalt in the cobalt oxides. Co_3O_4 has the oxidation states of +2 and +3 for cobalt. $Li_{0.5}Co_{2.5}O_4$ and $LiCoO_2$ has only +3 oxidation state for cobalt whereas dethiliated $LiCoO_2$ has +3 and +4 oxidation states for cobalt.

6.2 Studies on $Li_{0.5}Co_{2.5}O_4$

6.2.1 Synthesis

Lithium substituted cobalt oxide, $Li_{0.5}Co_{2.5}O_4$, was synthesized by the autocombustion method, following the procedure discussed for the synthesis of Co_3O_4 (refer section 3.3.1). Cobalt nitrate ($Co(NO_3)_2.6H_2O$), lithium nitrate ($LiNO_3$), and glycine were taken in the molar ratio of 0.5:2.5:0.45 and dissolved in minimum amount of distilled water and stirred vigorously to obtain a homogeneous solution. The mixed solution was evaporated slowly at 200 ºC, on a hot plate, to initiate the autocombustion reaction. After the evaporation of water, the resulting thick mass burnt spontaneously to obtain a fluffy powder mass. The as-synthesized powder (labelled as CO-L5) is used for further characterizations and electrochemical analysis.

6.2.2 Characterization

6.2.2.1 X-Ray diffraction

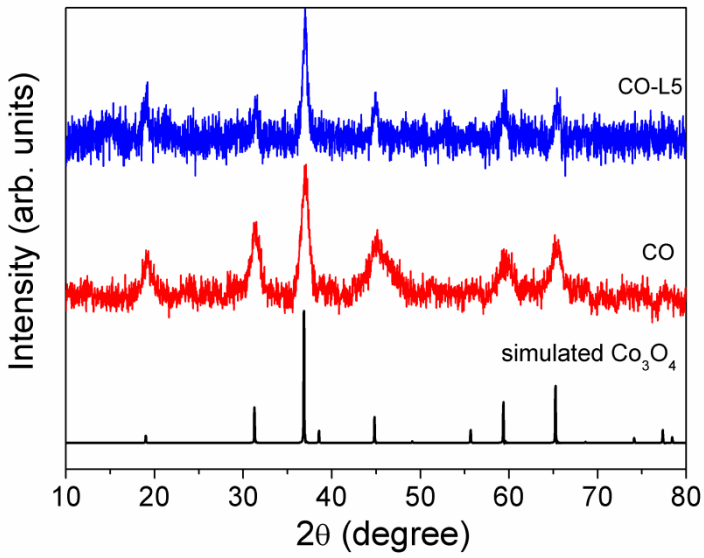

Figure 6.1 XRD patterns of Co_3O_4 and Li-substituted Cobalt oxide compared with the simulated pattern of Co_3O_4

Figure 6.1 shows the powder XRD patterns of cobalt oxide (CO) and Li-substituted cobalt oxide (CO-L5). The experimental patterns are compared with the simulated pattern of Co_3O_4. The powder pattern is simulated using the space group Fd3m and the corresponding cubic lattice parameter a = 8.0840 Å (JCPDS # 09-0418). The experimental patterns match well with the simulated one confirming the formation of spinel phase. The most intense peak

(at 2θ = 36.9º) which corresponds to (311) is used for the calculation of crystallite size using the Scherrer formula. The crystallite sizes are calculated as 7 nm and 12 nm for CO and CO-L5, respectively. The lattice parameters are calculated from least squares fitting and obtained as 8.075 Å and 8.084 Å for CO and CO-L5, respectively.

6.2.2.2 TEM studies

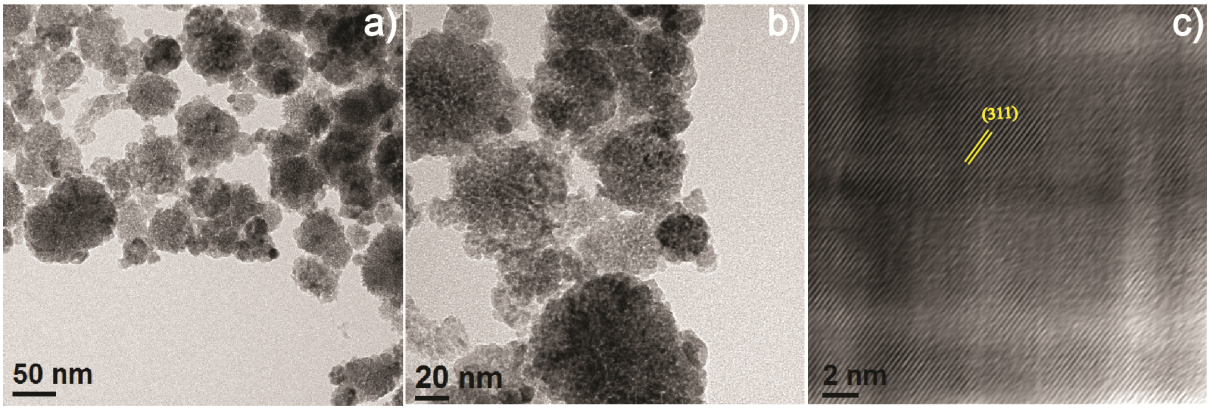

Figure 6.2 TEM images of CO-L5

TEM studies on CO are already discussed in the previous chapters. Figure 6.2 shows TEM images of lithium-substituted cobalt oxide (CO-L5) nanoparticles. As evidenced from Figure 6.2(a,b), all the particles are spherical in nature and aggregated together into small clusters. Lithium substitution in the cobalt oxide does not change the morphology of the cobalt oxide nanoparticles. Figure 6.2(c) shows the lattice fringes of the nanoparticles. The d-spacing of the lattice fringes is measured as 2.5 Å, which matches with the d-spacing of the (311) plane in the spinel lattice.

6.2.2.3 Surface area

Figure 6.3 shows the hysteresis loop of nitrogen adsorption-desorption isotherm of CO-L5. The nature of the hysteresis loop confirms type IV isotherm which is a characteristic behaviour of the mesoporous materials [5]. The BET surface area is obtained as 25 m^2/g. CO, prepared under similar conditions has higher BET surface area (70 m^2/g) compared to that of CO-L5 (see section 3.3.4, chapter 3). Thus, lithium substitution reduces the surface of area of cobalt oxide synthesized under similar conditions. It is found that the particle size is slightly larger for the substituted sample.

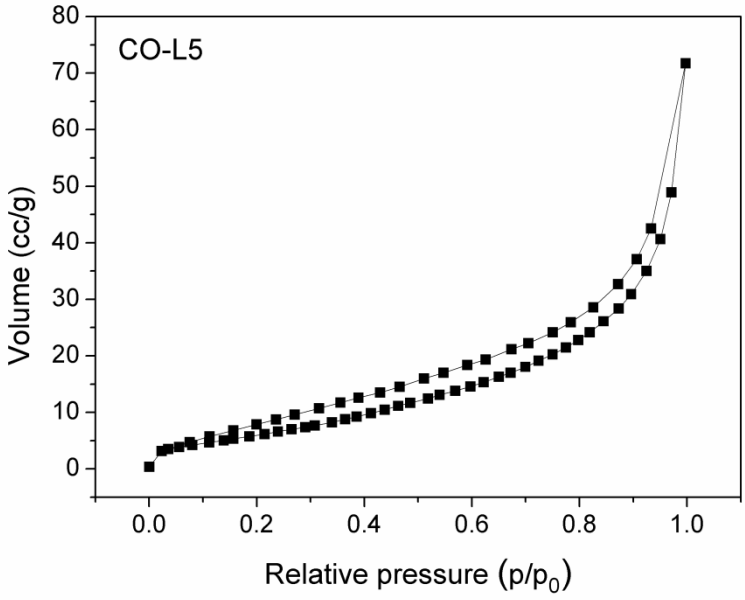

Figure 6.3 Nitrogen adsorption-desorption curves of CO-L5

6.2.2.4 Magnetic susceptibility

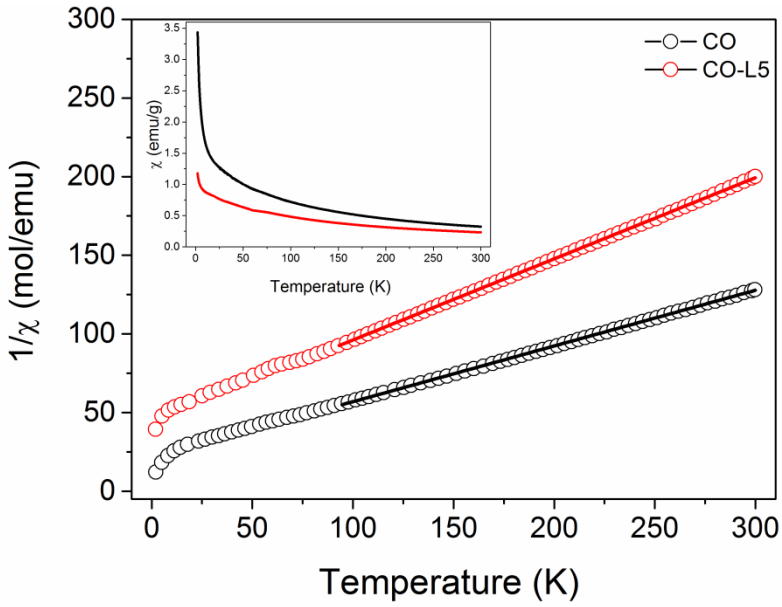

Figure 6.4 The temperature dependence inverse susceptibilities of Co_3O_4 (CO) and $Li_{0.5}Co_{2.5}O_4$ (CO-L5). Inset shows the susceptibility curves of Co_3O_4 (CO) and $Li_{0.5}Co_{2.5}O_4$ (CO-L5) nanoparticles

Figure 6.4 shows the results on the magnetic studies on CO and CO-L5. The inset of Figure 6.4 shows the magnetic susceptibility, measured as a function of temperature. The nature of

the curves indicates paramagnetic nature of CO and CO-L5. Figure 6.4 shows the $1/\chi$ vs T curves and above 100 K the curves show straight-line behaviour, following the Curie-Weiss law, $\chi = C/(T-\theta)$, where C is the Curie constant and θ is the Weiss temperature. From the fit to the straight lines above 100 K, C (1/slope) is obtained as 2.87 emu K $mol^{-1}$for CO and 1.94 emu K mol^{-1} for CO-L5 (Table 6.1).

Table 6.1 Curie constant and spin values of CO and CO-L5 from the magnetic studies

Sample code	Curie constant (emu K mol^{-1})	Total spin(S)
CO	2.87	1.94
CO-L5	1.94	1.53

Ideally, in Co_3O_4, Co^{3+} is in the low-spin state and the total magnetic moment should be coming from the unpaired electrons in the Co^{2+} [6-7].The calculated total spin is larger than the spin contribution from Co^{2+} (S=3/2), and therefore, the remaining spin value should be coming from the Co^{3+} ions.

$$\text{Spin contribution from } Co^{3+} = \text{Total spin} - (1-x)\frac{3}{2}$$

Therefore, the spin contribution from Co^{3+} is obtained as 0.45 for CO and the spin contribution from one Co^{3+} is 0.225. But in CO-L5, since all Co^{2+} is converted into Co^{3+} due to the substitution of $Li^{+,}$ the observed spin value is totally from Co^{3+} and this shows the paramagnetic nature of Co^{3+}. In CO-L5, the spin contribution from one Co^{3+} is 0.61. Thus, the magnetic studies shows that the Co^{3+} in $Li_{0.5}Co_{2.5}O_4$ are in their intermediate spin state or part of them are in the high-spin state.

6.2.2.5 X-Ray photoelectron spectroscopy

Figure 6.5 shows comparison of the XPS spectra of CO and CO-L5. The energy separation between Co $2p_{3/2}$ and Co $2p_{1/2}$ is approximately 15.1 eV and confirms the presence of spinel phase of the compounds [8-9]. Figure 6.5 shows that the Co 2p peak of CO is broad and the peak could be fitted to two components for the +2 and +3 oxidation states. On the other hand, the Co 2p spectrum of CO-L5 shows a narrow peak and could be fitted to mainly a single due to only Co^{3+}.

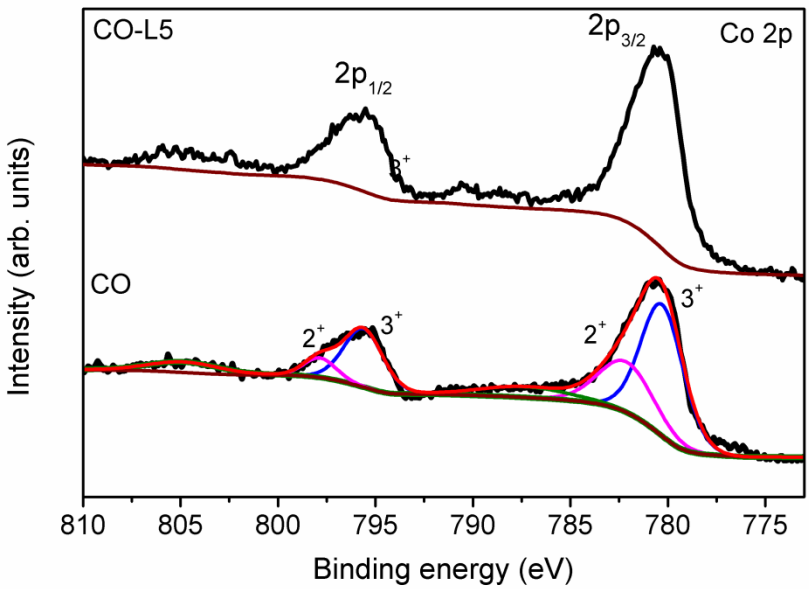

Figure 6.5 XPS spectra of CO and CO-L5

6.2.3 Electrochemical studies

6.2.3.1 Cyclic voltammetry

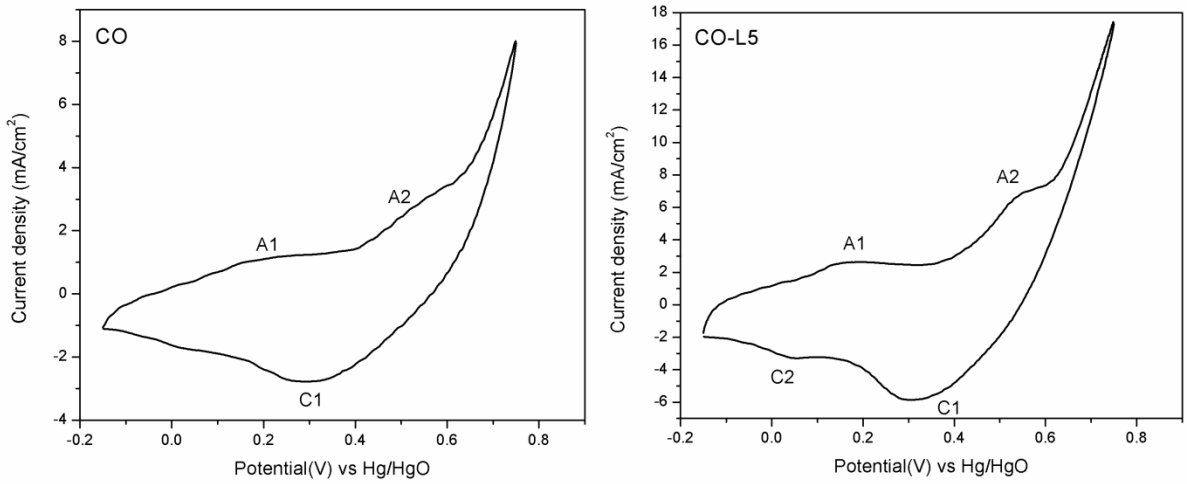

Figure 6.6 Cyclic Voltammetry of CO and CO-L5 in 0.1 M KOH at the scan rate of 50 mV/s

Figure 6.6 shows the cyclic voltammograms of CO and CO-L5 in 0.1 M KOH. Both the samples show the characteristic redox behaviour of cobalt oxide [10]. The voltammograms exhibit two anodic peaks (A1 and A2) corresponding to oxidation of Co^{2+} to Co^{3+}, and Co^{3+} to Co^{4+}, respectively. The cathodic peaks (C1 and C2) correspond to the reduction of Co^{4+} to Co^{3+} and Co^{3+} to Co^{2+}, respectively. The anodic redox peak A2 (at 0.55 V vs Hg/HgO) is more predominant in CO-L5, when compared to that of CO. This can be due to effect of

lithium substitution in the cobalt oxide. The lithium substitution converts the Co^{2+} to Co^{3+} in the cobalt oxide, to maintain charge neutrality and thereby increasing the population of Co^{3+} in CO-L5 [11].

6.2.3.2 Tafel plots

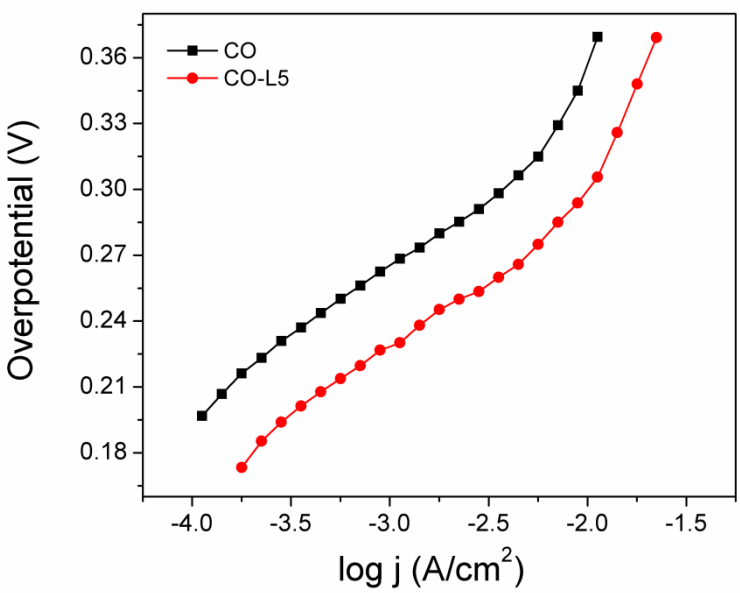

Figure 6.7 Tafel plots of CO and CO-L5

The electrocatalytic activity and kinetic parameters of the as synthesized cobalt oxide and lithium substituted cobalt oxide (CO and CO-L5) are studied by galvanostatic Tafel polarization technique for the OER. An efficient electrocatalyst for the OER should have lower overpotential and higher exchange current density for the good electrocatalytic activity. Figure 6.7 shows the Tafel plots of cobalt oxide and lithium substituted cobalt oxide (CO and CO-L5). The kinetic parameters such as overpotential, Tafel slope and exchange current density are extracted from the Tafel plots and given in Table 6.2. Both the catalysts show similar Tafel behavior with different overpotentials.

Table 6.1 Overpotential, Tafel slope and exchange current density parameters from Tafel plots of CO and CO-L5

Sample code	Overpotential(η) at 10 mA/cm^2 (mV)	Tafel slope (mV)	Exchange current density (A/cm^2)
CO	358	62	5.2×10^{-8}
CO-L5	303	64	2.9×10^{-7}

From Table 6.2, it is clear that lithium substituted cobalt oxide has lower overpotential and higher exchange current density than the unsubstituted cobalt oxide (CO). Both the catalysts have almost similar Tafel slope. Higher exchange current density implies higher catalytic activity. So, CO-L5 has better electrocatalytic performance than by CO for the OER. The electrocatalytic activity of CO-L5 is comparable to that of $ZnCo_2O_4$ (ZCO 10), reported in Chapter 4 (see section 4.4.2, chapter 4). In ZCO 10, all the Co^{2+}in Co_3O_4 are replaced by Zn^{2+} and the compound shows a very similar overpotential (300 mV at 10 mA/cm^2), Tafel slope (60 mV) and exchange current density (1×10^{-7} A/cm^2). Hence, the suppression of Co^{2+} in the cobalt by Li^+ oxides improves the electrocatalytic activity of Co_3O_4 for OER.

6.2.3.3 Roughness factor

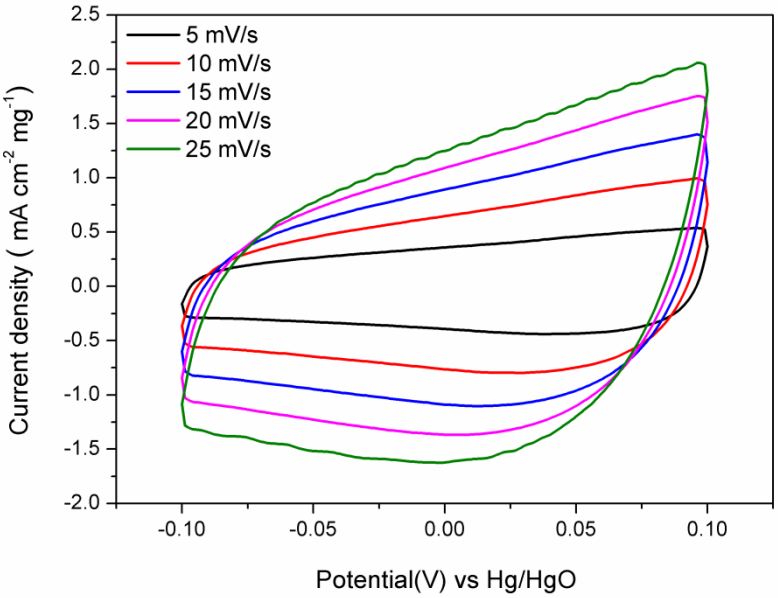

Figure 6.8 Cyclic voltammetry of Co-L5 in 0. M KOH at different scan rates in the non-Faradic potential window (-0.1 to 0.1 V)

Roughness factor is determined from the double layer capacitance measurements [12]. The details of the technique are explained in Chapter 2. Figure 6.8 shows the cyclic voltammograms of CO-L5 at different scan rates in the non-Faradaic potential window. Figure 6.9 shows the plot of scan rate vs capacitive current and a linear behavior is observed. The slope of the straight line gives the double layer capacitance and from that the roughness factor is calculated as 881. The roughness factor of CO is obtained as 337 (Chapter 4, section 4.4.5). Thus, the roughness factor of CO-L5 (881) is quite high, comparable to the roughness

factor of 722 obtained for $Zn_{0.8}Co_{2.2}O_4$ (ZCO 8) reported in Chapter 4. This can be due to the higher population of Co^{3+} in CO-L5 compared to that in ZCO 8. The higher roughness factor is due to the Co^{3+} in the surface of the catalyst responsible for the capacitive behaviour [13].

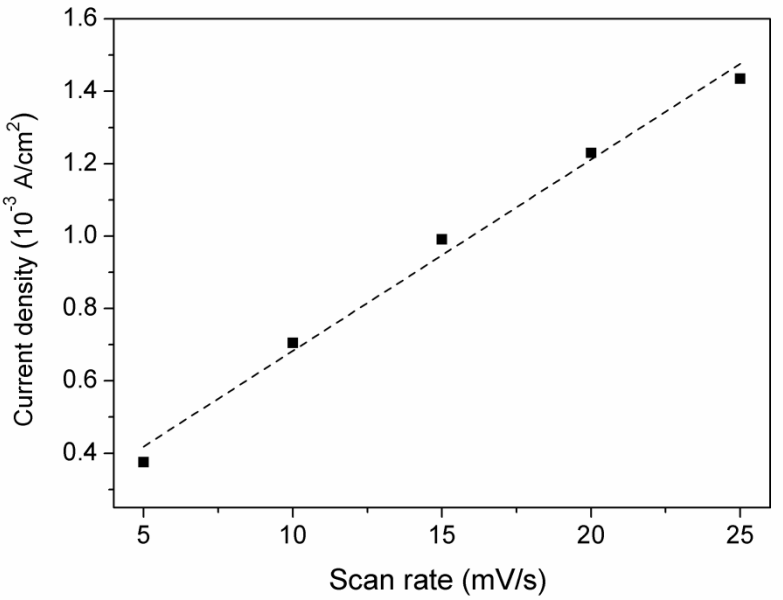

Figure 6.9 Capacitive current density as a function of scan rate for CO-L5

6.2.4 Discussion

The electrocatalytic activities of Co_3O_4 (CO) and $Li_{0.5}Co_{2.5}Co_2O_4$ (CO-L5) have been studied for OER. From the Tafel plots, it is found that CO-L5 has higher electrocatalytic activity than CO with a lower overpotential and higher exchange current density, compared to CO. CO-L5 has almost 50 mV lower overpotential (at 10 mA/cm^2) and 10 times increased exchange current density than CO. The increased electrocatalytic activity of CO-L5 can be due to the Li^+ substitution in the spinel Co_3O_4 structure. Usually, Lithium doping is known to increase the conductivity of a semiconductor [1]. In the case of Co_3O_4 also, it has been shown that Li doping increases the electrical conductivity and thereby reducing the resistance associated with the OER [11, 14].

XPS studies showed that Li substitution in Co_3O_4 converts the Co^{2+} to Co^{3+} to maintain the charge neutrality. From the previous studies, it is found that Co^{3+} is the active site or the conversion of Co^{3+} to Co^{4+} plays the important role in the mechanism of OER [15]. Therefore, the increased population of Co^{3+} in the CO-L5, due to the lithium substitution could be one of the reasons for the enhanced electrocatalytic activity of CO-L5 for the OER.

Even though CO-L5 has lower BET surface area than CO, it shows higher electrocatalytic activity for OER than CO. This shows that surface area is not the factor which determines the electrocatalytic activity. The electronic structure of the catalyst also plays an important role in the electrocatalytic activity. Magnetic studies revealed some information about the difference in the electronic structure of the two catalysts. The spin contribution per Co^{3+} in CO and CO-L5 are obtained as 0.225 and 0.612. Higher spin contribution from Co^{3+} is due to the higher e_g orbital occupancy. e_g orbital occupancy is identified as one of the important descriptor for the OER [16-17]. e_g orbital is antibonding in nature and involves in the in the overlap with the oxygen related adsorbates and intermediates [18-19]. CO-L5 has higher e_g occupancy and shows higher electrocatalytic activity than CO. Also, CO-L5 has higher roughness factor (Rf =881) than for CO (Rf =337). The higher roughness factor leads to increased active sites which are exposed at the surfaces of the catalyst. Thus, combination of the parameters such as presence of only Co^{3+} ions, intermediate- or high-spin states of Co^{3+}, roughness factor, etc is likely to be reason for the higher OER activity of lithium substituted cobalt oxide $Li_{0.5}Co_{2.5}Co_2O_4$ (CO-L5) when compared to that of Co_3O_4 (CO).

6.3 Studies on $LiCoO_2$ and delithiated $LiCoO_2$

6.3.1 Synthesis

Lithium cobalt oxide ($LiCoO_2$) is synthesized by the autocombustion method. Cobalt nitrate ($Co(NO_3)_2.6H_2O$), lithium nitrate ($LiNO_3$) and glycine were taken in the mole ratio of 1:1:1.55 and the synthesis procedure is the same as that described under section 6.2.1.The as-synthesized powder was ground well and calcined at 400 ºC in air for 3 hours. The calcined powder (labelled as LCO) is used for further characterizations and electrochemical analysis.

The obtained $LiCoO_2$ (LCO) powder was used for the delithiation process for the preparation of $Li_{0.5}CoO_2$ (De-LCO). The chemical delithiation process, using potassium persulfate ($K_2S_2O_8$), was followed for the preparation of De-LCO. As per the reported procedure [20], 1 g of $LiCoO_2$ and 1.75 g of $K_2S_2O_8$were dispersed in 50 ml of distilled water in a round bottom flask and stirred for 24 hours at 60 ºC. The dispersion was then cooled to room temperature and washed with large amount of distilled water by centrifugation. The obtained precipitate was dried in air at 60 °C for 24 h. The dried power was used for further characterizations and electrochemical analysis.

6.3.2 Characterization

6.3.2.1 X-Ray diffraction

Figure 6.10 shows the XRD patterns of $LiCoO_2$ (LCO) and $Li_{0.5}CoO_2$ (De-LCO). The experimental XRD patterns are matched well with the reference patterns (JCPDS data) and confirm the formation of the corresponding phases. As already discussed, $LiCoO_2$ has two crystalline polymorphs [4]. The main difference in the XRD pattern of the both the structure is the peak at 2θ = 66º. Spinel structure (space group *Fd3m*) has a single peak at 2θ = 66º, which corresponds to the reflection of (440), whereas in rhombhohedral structure (space group $R\bar{3}m$), the peak splits in to two which are the reflections from the (108) and (110) planes. Low temperature synthesized $LiCoO_2$ (space group *Fd3m*) adopts lithiated spinel structure $\{Li_2\}_{16c}[Co_2]_{16d}O_4$, in which the Li^+ ions occupy the 16c octahedral sites and the Co^{3+} ions occupy the 16d octahedral sites of the spinel framework. The average crystallite size is calculated from the full width at half maxima (FWHM) of the maximum intensity peak (2θ =19.39 º) using the Scherrer formula (section 2.3.1, chapter 2) as 17±1 nm for LCO.

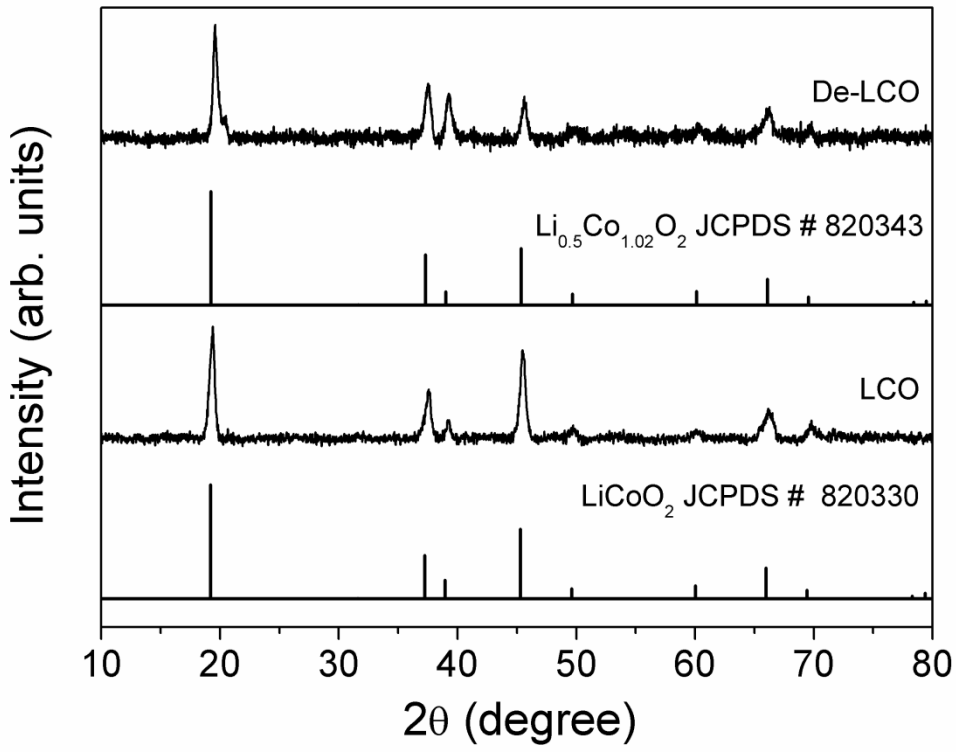

Figure 6.10 XRD patterns of lithium cobalt oxide (LCO) and delithiated lithium cobalt oxide (De-LCO) compared with the JCPDS data.

6.3.2.2 TEM studies

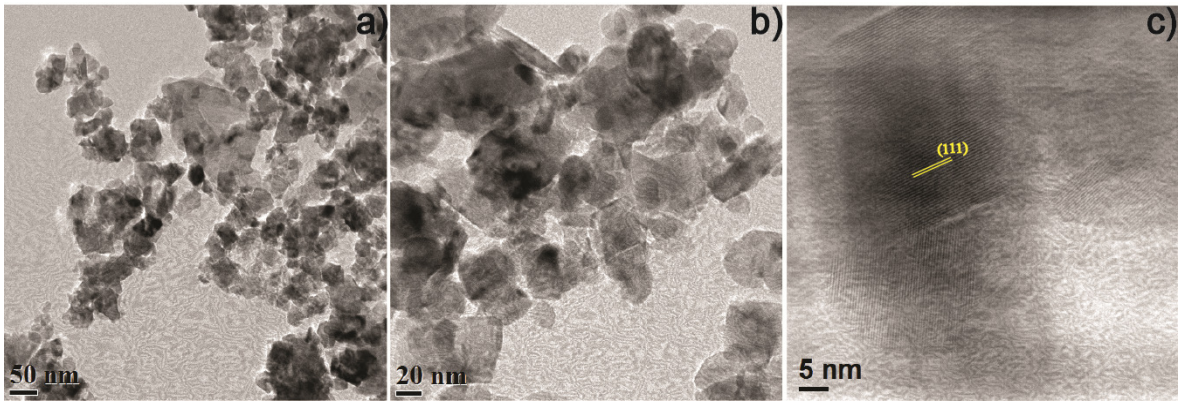

Figure 6.11 TEM images of LCO

Figure 6.11 shows the TEM images of $LiCoO_2$ (LCO). No well-defined morphology has been found. Small particles are aggregated and formed some cube-like and rectangular shapes. Figure 6.11(c) shows the lattice fringes of LCO and the observed d-spacing (4.5 Å) matches with the d-spacing of the (111) plane, which is the most intense peak in the XRD pattern. TEM images of delithiated $LiCoO_2$ (De-LCO) are shown in Figure 6.12. The chemical delithiation process did not change the morphology and a similar morphology as that of $LiCoO_2$ has been observed for De-LCO. The observed lattice fringes are shown in Figure 6.12(c). The observed lattice fringe (4.7 Å) matches with the d-spacing of the (111) plane.

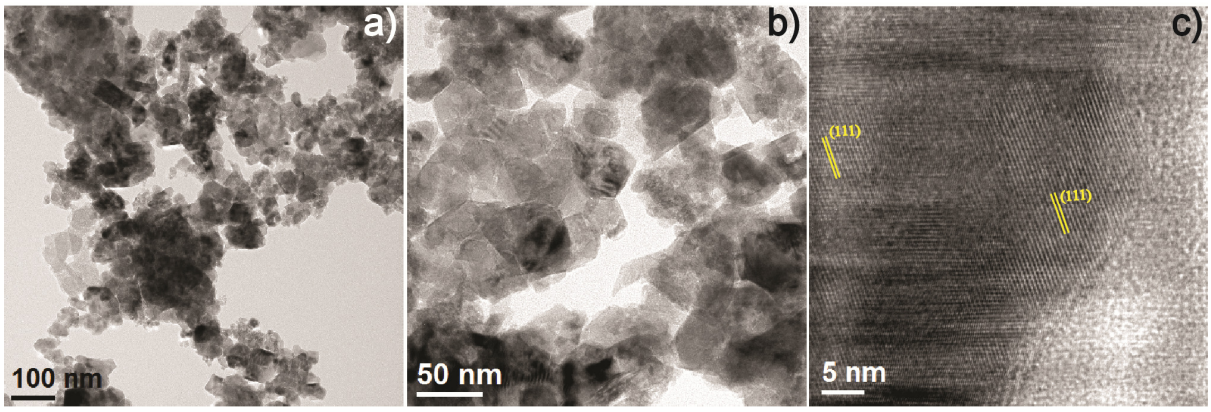

Figure 6.12 TEM images of De-LCO

6.3.2.3 Surface area studies

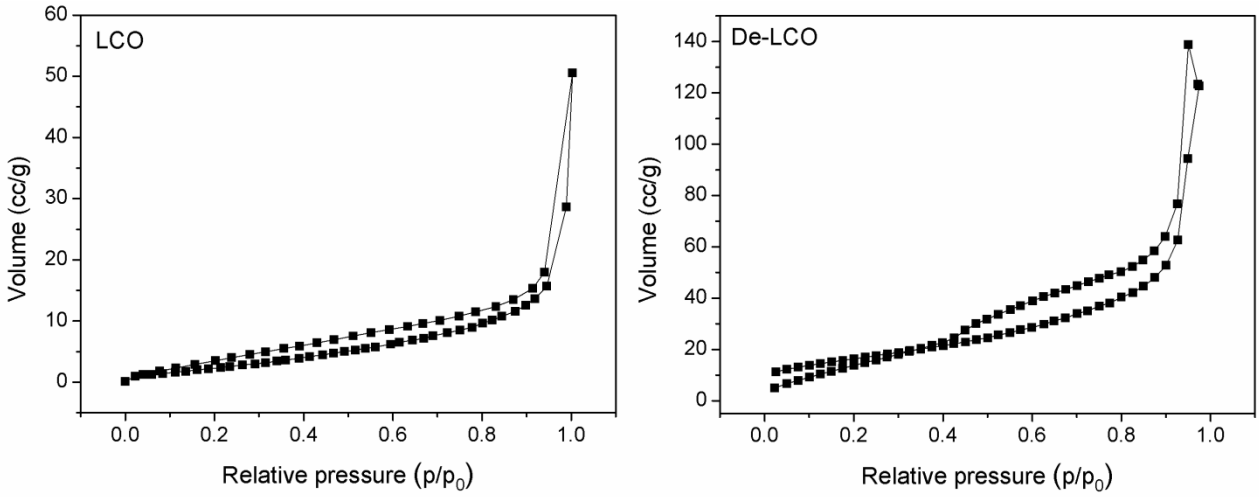

Figure 6.13 Nitrogen adsorption-desorption curves of LCO and De-LCO

Figure 6.13 shows the nitrogen adsorption-desorption studies on LCO and De-LCO. The shapes of the hysteresis loops confirm type IV isotherm and mesoporous nature of the materials. The BET surface areas are obtained as 11 m^2/g and 41 m^2/g. The results show that the chemical delithiation process increases the surface area of the catalyst.

6.3.2.4 Magneticsusceptibility

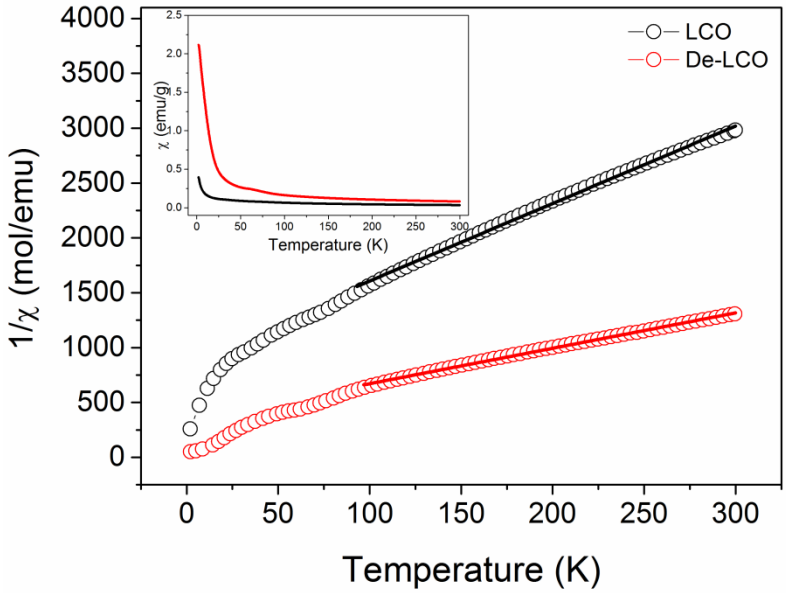

Figure 6.14 Temperature dependence of inverse magnetic susceptibility of $LiCoO_2$ (LCO) and delithiated $LiCoO_2$ (De-LCO). Inset: Magnetic susceptibility curves of $LiCoO_2$ (LCO) and delithiated $LiCoO_2$ (De-LCO) nanopartciles.

Magnetic susceptibility studies on LCO and De-LCO have been carried out and the results are shown in Figure 6.14. The inset in figure shows the temperature variation of susceptibility measured in an applied magnetic field of 1 T. The paramagnetic nature of the samples is obvious from the susceptibility curves. The main figure (Figure 6.14) shows the $1/\chi$ vs T plots. Above 100 K a straight-line behaviour is observed for both samples. The linear part of the graph above 100 K is fitted to the Curie-Weiss law, $\chi = C/(T-\theta)$, where C is the Curie constant and θ is the Weiss temperature. The results of the fit are shown in Table 6.3.

Table 6.3 Curie constant and spin values of LCO and De-LCO from the magnetic studies

Sample code	Curie constant (emu K mol^{-1})	Total spin(S)
LCO	0.14	0.23
De-LCO	0.31	0.43

Since LCO ($LiCoO_2$) contains only Co^{3+}, the observed spin value is coming only from the Co^{3+} and shows the paramagnetic behavior of Co^{3+}. The spin state of Co^{3+} in $LiCoO_2$ is controversial, high-spin or intermediate-spin is reported [21-22]. The observed value, less than that expected for one unpaired electron (S=0.5) suggests that probably part of the Co^{3+} is in the low-spin state. Delithiation of $LiCoO_2$ induces Co^{4+} in $Li_{0.5}CoO_2$. Because of this reason, De-LCO a higher spin value is obtained from the magnetic measurements (Table 6.3) which is arising from Co^{4+}. $Co^{4+}$is d^5 system and prefers low-spin configuration with a single unpaired electron [23]. The calculated spin is closer to that for one unpaired electron, confirming the low-spin configuration of Co^{4+}.

6.3.2.5 X-Ray photoelectron spectroscopy

Figure 6.15 shows Co 2p XPS spectra of LCO and De-LCO. The changes in the oxidation state of cobalt in LCO after chemical delithiation are very clear by comparing the XPS spectra of LCO and De-LCO. The broadening of the Co 2p peaks located around 779.6 eV and 794.7 eV towards the higher binding energy confirms the presence of Co^{4+} in De-LCO [24]. The XPS spectrum of De-LCO is fitted for the quantification of the Co^{3+}/Co^{4+} ratio. From the area of the of Co^{3+} and Co^{4+} components, the ratio of Co^{3+}:Co^{4+} is found to be 0.515:0.485 which is comparable to the expected ratio of 1:1.

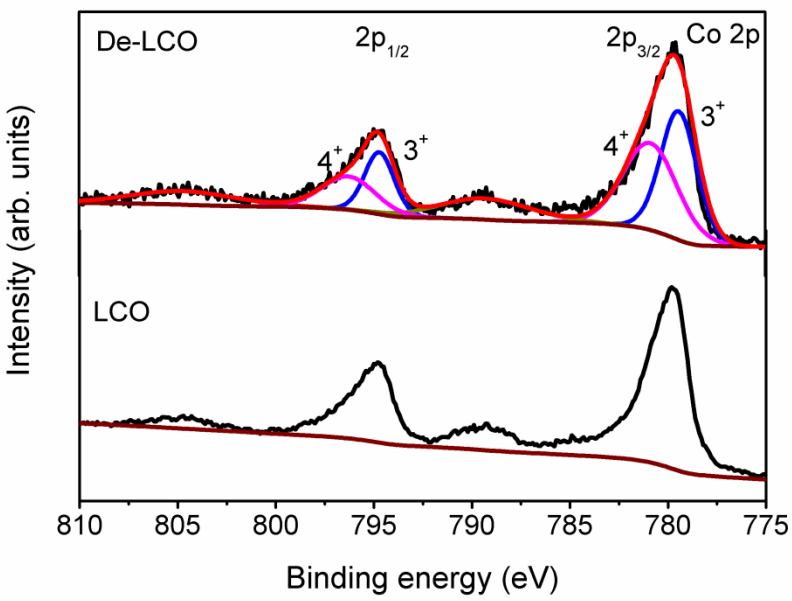

Figure 6.15 XPS spectra of LCO and De-LCO

6.3.3 Electrochemical studies

6.3.3.1 Cyclic voltammetry

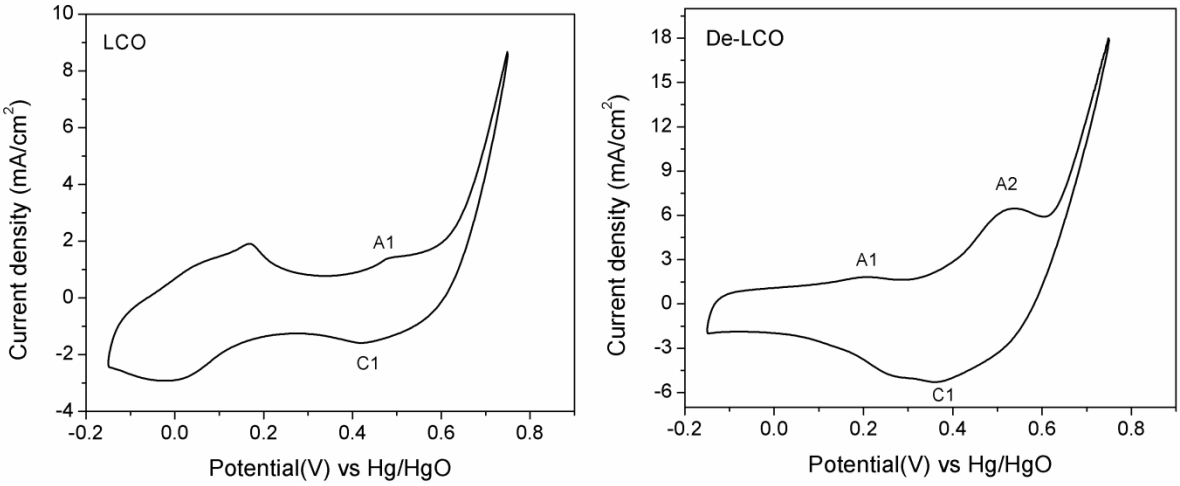

Figure 6.16 Cyclic voltammetry of $LiCoO_2$ (LCO) and delithiated $LiCoO_2$ (De-LCO) in 0.1 M KOH at the scan rate of 50 mV/s

The redox reactions and electrochemical properties of $LiCoO_2$ (LCO) and delithiated $LiCoO_2$ (De-LCO) have been studied by cyclic voltammetry. Figure 6.16 shows the cyclic voltammetry curves of LCO and De-LCO. LCO shows two redox peaks in the anodic region

and two redox peaks in the cathodic region. The redox peaks observed at the higher potentials (A1&C1) are similar to the redox peaks of Co_3O_4 and it can be assigned to the oxidation of Co^{3+} to Co^{4+} and the reduction of Co^{4+} to Co^{3+}. The redox peaks observed at the lower potential can be due to the structural transformation at deep lithium extraction and involves proton insertion, due to the instability at high Co^{4+} contents [25]. Cyclic voltammetry curve of De-LCO has almost similar behaviour as that of Co_3O_4. The intensity of the redox peak corresponding to the oxidation of Co^{3+} to Co^{4+} is enhanced for De-LCO when compared to LCO. This can be due to the introduction of Co^{4+} in De-LCO due to the delithiation process.

6.3.3.2 Tafel plots

The electrocatalytic activities of LCO and De-LCO for the OER have been studied by galvanostatic Tafel polarization technique. Figure 6.17 shows the Tafel plots of LCO and De-LCO. The overpotential (η) vs log (current density (j)) curves show straight line behaviour with a Tafel slope after the correction for the uncompensated resistance. The kinetic parameters such as overpotential, Tafel slope and exchange current density are extracted from Tafel plots and are given in Table 6.4.

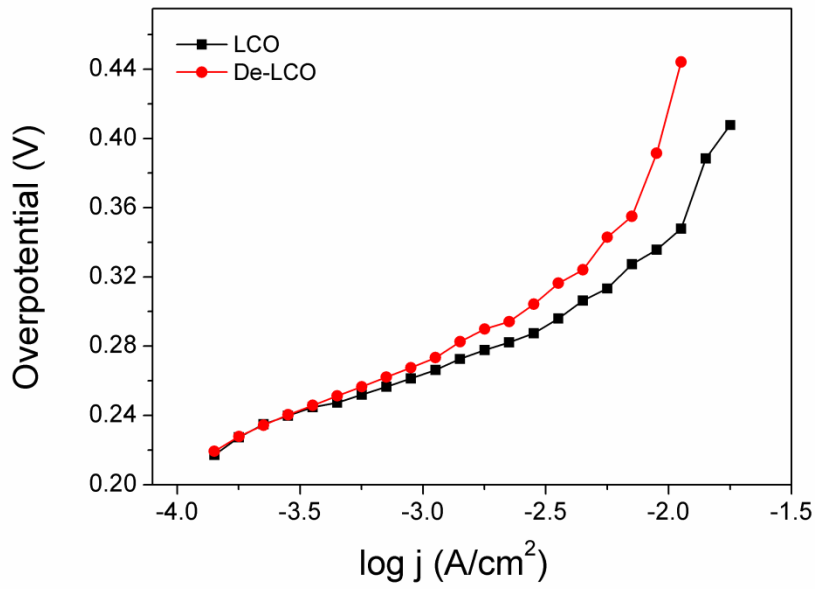

Figure 6.17 Tafel plots of $LiCoO_2$ (LCO) and delithiated $LiCoO_2$ (De-LCO)

Table 6.4 Overpotential, Tafel slope and exchange current density parameters from Tafel plots of LCO and De-LCO

Sample code	Overpotential(η) at 10 mA/cm^2 (mV)	Tafel slope (mV)	Exchange current density (A/cm^2)
LCO	344	60	2.0×10^{-8}
De-LCO	418	66	7.0×10^{-8}

From Table 6.4, it may be seen that LCO shows a lower overpotential (344 mV) compared to that for CO (358 mV, see section 6.2.3.2). Even though LCO has very low surface area (11 m^2/g) compared to CO (70 m^2/g), LCO shows higher electrocatalytic activity. This can be due to the structure of LCO. Compared to CO, all the Co atoms in the LCO are Co^{3+} and all are in the octahedral positions. The octahedral Co^{3+} is more stable and active for the oxygen evolution reaction, whereas Co^{3+} and Co^{2+} in tetrahedral coordination is inactive [25]. Moreover, the loss of crystal field stabilization energy (CFSE) during the oxidation of low-spin Co^{3+} ($3d^6$, $t_{2g}^6 e_g^0$) to Co^{4+} ($3d^5$, $t_{2g}^5 e_g^0$) on the surface of LCO and also due to the high conductivity (possibly metallic) of the surface arising from the partially filled t_{2g} orbitals of Co^{4+} across the shared octahedral edges may favor the high electrocatalytic activity of LCO for OER, as reported [25].

6.3.3.3 Roughness factor

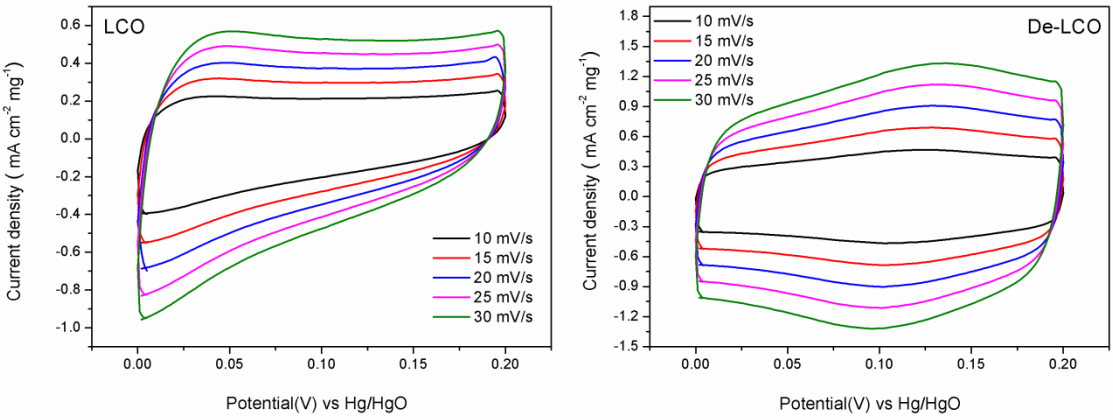

Figure 6.18 Cyclic voltammetry of LCO and De-LCO in 0. M KOH at different scan rates in the non-Faradic potential window (0 to 0.2 V)

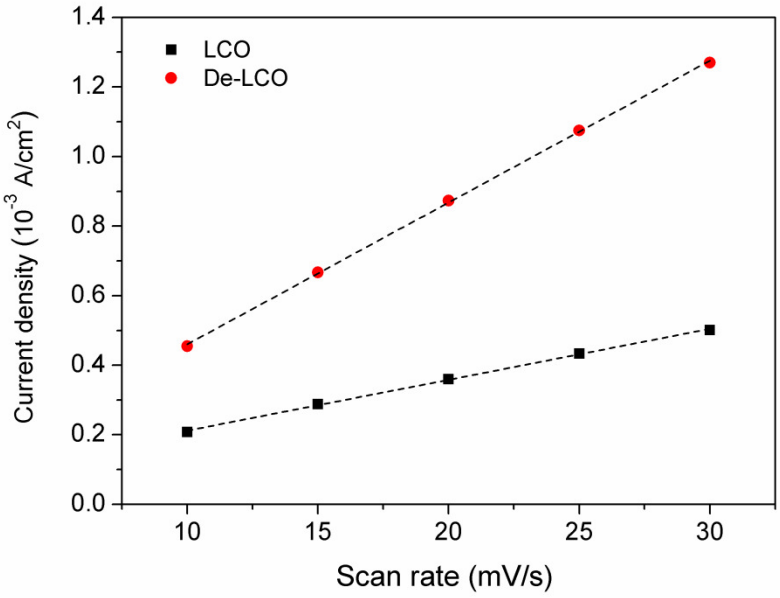

Figure 6.19 Capacitive current density as a function of scan rate of LCO and De-LCO

Roughness factor is determined from the double layer capacitance measurements [12]. Cyclic voltammetry curves were recorded in the non-Faradaic region (0 to 0.2 V vs Hg/HgO) at different scan rates, as shown in Figure 6.18. It is assumed that double layer charging is the only process in the potential window. Figure 6.19 shows the linear part of scan rate vs capacitive current. The slope gives the double layer capacitance and from that the roughness factor is calculated and tabulated (Table 6.5). LCO shows a roughness factor of 2440. After the chemical delithiation, the roughness factor of is reduced to 680 for De-LCO.

Table 6.5 Roughness factor of LCO and De-LCO

Sample name	Roughness factor
LCO	2440
De-LCO	680

The roughness factor of LCO is quite high compared to the all other materials studied in this chapter. This can be due to the exposure of octahedrally coordinated Co^{3+} which is responsible for the capacitive behaviour. The population of octahedral Co^{3+} is higher in LCO compared to CO, CO-L5 and De-LCO.

6.4 Discussion

When we compare the electrocalalytic activities of LCO and De-LCO, LCO has lower overpotential (344 mV) than for De-LCO (418 mV). Actually, comparison of the electrocatalytic activities of LCO and De-LCO is controversial. In some studies, it has been reported that the delithiation process increases the catalytic activity [28] whereas in other report decreased catalytic activity is reported [25]. In the present case, De-LCO has higher overpotential than LCO, but De-LCO has very low roughness factor (680) than for LCO (2440) and still has a reasonable overpotential for OER.

The delithaition process in LCO is expected to increase the electrocatalytic activity due to the increased oxidation state of cobalt in De-LCO from the average oxidation of 3 to 3.5. This could enhance the electrophilicity of the adsorbed O and thereby facilitates the reaction between OH^- anion and adsorbed O on the catalytic sites for the formation of –OOH species [15, 26]. This is considered as the rate limiting step in the mechanism of OER [27]. Also, this is experimentally verified by a model which promotes the catalytic activity of the molecular cobaltate clusters if the oxidation state of cobalt is more than +3 [26]. The delithiation process makes the Co-O bond more covalent, which may lead to the formation of holes in the hybridized Co 3d – O 2p band and increases the electrophilic nature of the material, which in turn facilitates the adsorption of hydroxyl anions and thereby increasing the electrocalytic activity of OER. Delithiation also increases the electronic conductivity of LCO. Actually, $LiCoO_2$ is a semiconductor, whereas $Li_{0.5}CoO_2$ is metallic. Therefore, the efficient charge transport at the surface of the catalyst will be beneficial for the better electrocatalytic activity [28].

6.5 Conclusions

Spinel-type cobalt oxides with different oxidation states of cobalt; Co_3O_4 (Co^{2+} and Co^{3+}), $Li_{0.5}Co_{2.5}O_4$ (Co^{3+}), $LiCoO_2$ (Co^{3+}), and $Li_{0.5}CoO_2$ (Co^{3+}, Co^{4+}) are synthesized by a simple autocombustion method. The structural and electronic structure of all the cobalt oxides are studied using XRD, XPS and magnetic measurements, which revealed the details about the oxidation state and electronic structure of cobalt ions. The OER electrocatalytic activities are correlated to the oxidation state and electronic structure of cobalt in the cobalt oxides. Increasing the Co^{3+} spin contribution is found to increase the electrocatalytic activity in the following order $Li_{0.5}CoO_2$<Co_3O_4<$LiCoO_2$<$Li_{0.5}Co_{2.5}O_4$, based on the overpotential for OER.

The crystal structure containing more octahedral Co^{3+} ions is found to have higher electrocatalytic activity for OER and presence of the higher oxidation state (Co^{4+}) also improves the electronic properties in the cobalt oxides, thereby increasing the electrocatalytic activities for OER.

References:

1. Koumoto, K.; Yanagida, H., *Journal of the American Ceramic Society* **1981,** *64*, C-156.
2. Wu, X.; Scott, K., *International Journal of Hydrogen Energy* **2013,** *38*, 3123.
3. Goodenough, J. B.; Kim, Y., *Chemistry of Materials* **2010,** *22*, 587.
4. Gummow, R. J.; Liles, D. C.; Thackeray, M. M., *Materials Research Bulletin* **1993,** *28*, 235.
5. Sing, K. S.; Gregg, S., *Adsorption, surface area and porosity*.Academic Press, London: 1982
6. Roth, W., *Journal of Physics and Chemistry of Solids* **1964,** *25*, 1.
7. Raveau, B.; Seikh, M., *Cobalt oxides: from crystal chemistry to physics*. John Wiley & Sons: 2012.
8. Na, C. W.; Woo, H. S.; Kim, H. J.; Jeong, U.; Chung, J. H.; Lee, J. H., *Crystengcomm* **2012,** *14*, 3737.
9. Oku, M.; Sato, Y., *Applied Surface Science* **1992,** *55*, 37.
10. Boggio, R.; Carugati, A.; Trasatti, S., *Journal of Applied Electrochemistry* **1987,** *17*, 828.
11. Švegl, F.; Orel, B.; Grabec-Švegl, I.; Kaučič, V., *Electrochimica Acta* **2000,** *45*, 4359.
12. Trasatti, S.; Petrii, O., *Journal of Electroanalytical Chemistry* **1992,** *327*, 353.
13. Wang, H. Y.; Hung, S. F.; Chen, H. Y.; Chan, T. S.; Chen, H. M.; Liu, B., *Journal of the American Chemical Society* **2016,** *138*, 36.
14. Bocca, C.; Cerisola, G.; Magnone, E.; Barbucci, A., *International Journal of Hydrogen Energy* **1999,** *24*, 699.
15. McAlpin, J.; Surendranath, Y.; Dinca, M.; Stich, T.; Stoian, S.; Casey, W.; Nocera, D.; Britt, R., *Journal of the American Chemical Society* **2010,** *132*, 6882.
16. Zhou, S.; Miao, X.; Zhao, X.; Ma, C.; Qiu, Y.; Hu, Z.; Zhao, J.; Shi, L.; Zeng, J., *Nature communications* **2016,** *7*.
17. Suntivich, J.; May, K. J.; Gasteiger, H. A.; Goodenough, J. B.; Shao-Horn, Y., *Science* **2011,** *334*, 1383.

18. Betley, T. A.; Wu, Q.; Van Voorhis, T.; Nocera, D. G., *Inorganic Chemistry* **2008,** *47*, 1849.
19. Ballhausen, C. J.; Gray, H. B., *Inorganic Chemistry* **1962,** *1*, 111.
20. Graetz, J.; Hightower, A.; Ahn, C. C.; Yazami, R.; Rez, P.; Fultz, B., *The Journal of Physical Chemistry B* **2002,** *106*, 1286.
21. Han, B.; Qian, D.; Risch, M.; Chen, H.; Chi, M.; Meng, Y. S.; Yang, S.-H., *Journal of Physical Chemistry Letters* **2015,** *6*, 1357.
22. Qian, D.; Hinuma, Y.; Chen, H.; Du, L. S.; Carroll, K. J.; Ceder, G.; Grey, C. P.; Meng, Y. S., *Journal of the American Chemical Society* **2012,** *134*, 6096.
23. Xiong, F.; Yan, H. J.; Chen, Y.; Xu, B.; Le, J. X.; Ouyang, C. Y., *International Journal of Electrochemical Science* **2012,** *7*, 9390.
24. Liu, H.; Zhou, Y.; Moré, R.; Müller, R.; Fox, T.; Patzke, G. R., *Acs Catalysis* **2015,** *5*, 3791.
25. Maiyalagan, T.; Jarvis, K. A.; Therese, S.; Ferreira, P. J.; Manthiram, A., *Nature communications* **2014,** *5*.
26. Kanan, M. W.; Yano, J.; Surendranath, Y.; Dincă, M.; Yachandra, V. K.; Nocera, D. G., *Journal of the American Chemical Society* **2010,** *132*, 13692.
27. Yeo, B. S.; Bell, A. T., *Journal of the American Chemical Society* **2011,***133*, 5587.
28. Lu, Z.; Wang, H.; Kong, D.; Yan, K.; Hsu, P.-C.; Zheng, G.; Yao, H.; Liang, Z.; Sun, X.; Cui, Y., *Nature communications* **2014,** *5*.

Chapter 7

Conclusions and future perspectives

7.1 Conclusions

Spinel-type cobalt oxide, Co_3O_4, has been identified as a potential candidate as catalyst for the oxygen evolution reaction (OER) in electrochemical water splitting. Cobalt based materials are expected to replace the currently used precious metal oxide based anode materials such as RuO_2 and IrO_2 for OER. The mixed valent nature of cobalt, thermodynamic stability of the compound and the intrinsic catalytic property of cobalt are the important properties of Co_3O_4 which makes it a potential candidate as the anode material for the oxygen evolution reaction. It is known that metal cations change their oxidation state to higher values before the oxygen evolution reaction and the higher-valent cations act as active sites. In Co_3O_4, the cobalt ions are in the 2+ and 3+ oxidation states. The oxidation of Co^{3+} to Co^{4+} precedes the oxygen evolution reaction and Co^{4+} is identified as the active site for OER.

Currently used precious anode materials RuO_2 and $IrO_2$are stable and show good electrocatalytic activity in the acid medium. However, in the neutral and alkaline medium, corrosion/dissolution of the anode material limits its stability and electrocatalytic activity. Moreover, the oxygen evolution catalyst which is incorporated in photoelectrochemical cells demands stability in a wide range of pH, particularly at neutral medium. However, most of the transition metal oxides are stable only in the basic pH condition under applied potentials. Below pH 9, most of the transition metal oxides undergo severe corrosion.

The objective of the present study was to reduce the overpotential for the oxygen evolution reaction by tuning the microstructure and composition of Co_3O_4 nanostructures. In the present study, Co_3O_4 nanorods were synthesized by a template-free, simple co-precipitation/digestion method and studied the stability and electrocatalytic activity of the nanorods over a wide range of pH (4-14). Particularly, the stability issue of the Co_3O_4 nanorods in neutral and acidic medium is solved by introducing proton conducting phosphate buffer as the electrolyte. The oxygen evolution overpotential, much less than that reported in the literature, could be achieved using the nanorods. Also, the electrocatalytic activity of Co_3O_4 nanoparticles synthesized by an autocombustion method is compared with the activity of the nanorods. Even though surface area of the catalyst is one of the important descriptors for OER, in the present work, both Co_3O_4 nanostructures showed comparable electrocatalytic activities despite the difference in their surface areas. Magnetic studies revealed that the spin contribution from Co^{3+} is one of the important descriptors for OER. Since both the Co_3O_4

nanostructures have similar values of spin contribution from Co^{3+}, the electrocatalytic activities are also similar.

Since Co_3O_4 contains both Co^{2+} and Co^{3+}, to further understand the role of the different oxidation states and electronic structure of cobalt in Co_3O_4 for OER, electrochemical activity studies are performed by substituting part of Co^{2+} or Co^{3+} by the divalent ion Zn^{2+} or the trivalent Al^{3+}. Substitution of Co^{2+} by Zn^{2+} in Co_3O_4 is found to change the electronic structure of Co^{3+} from low-spin to intermediate/high-spin. The population of intermediate/high-spin $Co^{3+}$is found to increase with increasing Zn content in $Zn_xCo_{3-x}O_4$. The presence of intermediate/high-spin $Co^{3+}$is confirmed from magnetic susceptibility measurements and UV-Vis spectroscopic studies. The electrocatalytic activity is found to increase with respect to the population of high-spin Co^{3+}. The overpotential is found to decrease with increasing Zn content, and when all Co^{2+} are replaced by Zn^{2+} (x=1), the overpotential is found to be larger than that for x = 0.8. This confirmed the role of Co^{2+} which is involved in the formation of CoOOH, which is believed as the active species in the OER mechanism.

The role of Co^{3+} in Co_3O_4 for OER is studied by substituting Co^{3+} by Al^{3+}. The magnetic susceptibility studies showed that the remaining Co^{3+} present in $Co_{3-x}Al_xO_4$ are in their low-spin state only and this implies that the introduction of Al^{3+} does not facilitate the change in the electronic structure of Co^{3+} from low-spin to high-spin. When the Co^{3+} content decreases due to the substitution of Al^{3+}, the electrocatalytic activity for OER is also found to be decreased. It shows that presence of Co^{3+} is essential for OER activity in Co_3O_4.

The effect of different oxidation states of cobalt (Co^{2+}, Co^{3+}, Co^{4+}) on the electrocatalytic activity for OER is studied in cobalt oxides without changing the crystal structure. Lithium containing spinel-type cobalt oxide, $Li_{0.5}Co_{2.5}O_4$, with only Co^{3+}, is found to show higher catalytic activity than Co_3O_4, due to the higher population of Co^{3+}. Similarly $LiCoO_2$(with only Co^{3+}) showed better catalytic activity than Co_3O_4, probably due to the higher population of octahedral Co^{3+}. Dethiation of $LiCoO_2$ induces Co^{4+} and equal amount of Co^{3+} and Co^{4+} are found in $Li_{0.5}CoO_2$. $Li_{0.5}CoO_2$ showed higher overpotential for OER than for $LiCoO_2$. Based on the overpotential values, the electrocatalytic activities of different spinel-type cobalt oxides are found to be in the order $Li_{0.5}CoO_2<Co_3O_4<LiCoO_2<Li_{0.5}Co_{2.5}O_4$.

Thus, the present studies have provided information on the role of Co^{2+} and Co^{3+}, including the electronic structure of Co^{3+}, on the electrocatalytic activity of Co_3O_4 nanostructures for electrochemical water splitting. Oxygen evolution overpotential as low as 260 mV (at 10 mA/cm^2) is obtained for the Zn-substituted composition $Zn_{0.8}Co_{2.2}O_4$, comparable to that reported for the precious metal oxides.

7.2 Future perspectives

In the present study, it is found that the e_g orbitals occupancy of Co^{3+} in the spinel cobalt oxides influences the electrocatalytic activity for OER. The method and models for the quantification of e_g orbital occupancy is established in perovskites. However, the quantification of e_g orbital occupancy is not yet established in spinels, due to the complexity of the structure and the presence of more than one B-sites in the spinel structure (AB_2O_4). DFT studies are required to develop models for the quantification of e_g orbital occupancy. Better understanding about the electronic structure and the electrocatalytic activity for OER demands the quantification of e_g orbital occupancy.

All the spinel cobalt oxides discussed in this work are *p*-type semiconductors with good electrocatalytic activities for OER. Coupling this *p*-type electrocatalyst with *n*-type semiconductors like TiO_2, WO_3 and Fe_2O_3 which have absorption in the visible region is expected to increase the overall efficiency of the photoelectrochemical cells due to following reasons:

i. *p*-type electrocatalyst can capture the photogenerated holes and reduce the recombination of the photogenerated electron-hole pairs.
ii. Since OER is the bottleneck for the kinetics for the overall water splitting, incorporation of oxygen evolution electrocatalyst in the photoelectrochemical cells is expected to increase the overall kinetics by many orders.

Hence, use of the developed catalysts in photoelectrochemical cells needs to be studied to tap the potential of the materials for direct solar-to-hydrogen conversion. It is expected that the best compositions studied in the present work may find applications in photoelectrochemical cells.

Publications

1. **R.M.Ramsundar** , Joyashish Debgupta , Vijayamohanan K Pillai , P.A.Joy, "Co_3O_4 Nanorods-Efficient Non-noble Metal Electrocatalyst for Oxygen Evolution at Neutral pH" Electrocatalysis-Us. 2015; 6(4):331-40.
2. P.A.Joy, Vijayamohanan K Pillai, **R.M.Ramsundar** , Joyashish Debgupta, "Electrochemical process for water splitting using porous Co_3O_4 nanorods " US2015136614A1, WO2013160915A1
3. **R.M.Ramsundar,** P.A.Joy, "Zinc cobalt oxide composition with low overpotential for oxygen evolution reaction for electrochemical water splitting", IN201611034059 (patent filed)